

**Channel Modeling for Hybrid Free-Space Optics/Radio  
Wireless Systems for Fifth-Generation (5G) Mobile  
Backhaul Networks**

**Trinh Viet Phuc**

A DISSERTATION

SUBMITTED IN FULFILLMENT OF THE REQUIREMENTS

FOR THE DEGREE OF DOCTOR OF PHILOSOPHY

IN COMPUTER SCIENCE AND ENGINEERING

Graduate Department of Computer and Information Systems

The University of Aizu

2017



Copyright by Trinh Viet Phuc

All Rights Reserved

The thesis titled

*Channel Modeling for Hybrid Free-Space Optics/Radio Wireless  
Systems for Fifth-Generation (5G) Mobile Backhaul Networks*

by

Trinh Viet Phuc

is reviewed and approved by:

Chief referee

*Professor*

Anh T. Pham

Anh T. PHAM 

---

*Professor*

Toshiaki Miyazaki

---

*Professor*



Igor Lubashevsky

---

*Senior Associate Professor*

Truong Cong Thang

---

The University of Aizu

2017



# Contents

Contents . . . . .	v
List of Figures . . . . .	x
List of Notations . . . . .	xiv
List of Abbreviations . . . . .	xv
Abstract . . . . .	xvi
1. Introduction . . . . .	1
1.1 Motivations . . . . .	1
1.2 Original Contributions . . . . .	2
1.3 Thesis Organization . . . . .	4
2. Background of The Study . . . . .	8
2.1 Introduction . . . . .	8
2.2 A History of Wireless Cellular Networks . . . . .	8
2.2.1 The First Generation (1G) . . . . .	9
2.2.2 The Second Generation (2G) . . . . .	9
2.2.3 The Third Generation (3G) . . . . .	10
2.2.4 The Fourth Generation (4G) . . . . .	10
2.2.5 Issues and Challenges of Existing Cellular Networks . . . . .	10

2.3	The Fifth Generation (5G) . . . . .	11
2.3.1	A New Horizon in Radio Spectrum . . . . .	11
2.3.2	5G Visions . . . . .	12
2.4	Conclusions . . . . .	13
3.	State of the Art and Scope of the Study . . . . .	15
3.1	Introduction . . . . .	15
3.2	Backhaul Networks: State of the Art . . . . .	17
3.2.1	Conventional Architecture . . . . .	18
3.2.2	5G Ultra-Dense Architecture . . . . .	19
3.2.3	Technologies . . . . .	21
3.2.3.1	mmWave Backhauling Technologies . . . . .	22
3.2.3.2	FSO Backhauling Technologies . . . . .	23
3.2.4	Architecture with Hybrid Technologies . . . . .	25
3.3	Scope of the Study . . . . .	27
3.3.1	Problem Statements . . . . .	27
3.3.2	Hybrid Systems . . . . .	28
3.3.3	Contributions . . . . .	29
3.4	Conclusions . . . . .	30
4.	Relaying mmWave RF/FSO Systems . . . . .	31
4.1	Introduction . . . . .	31
4.2	System Model . . . . .	34
4.3	mmWave RF Channel Model . . . . .	35
4.4	FSO Channel Model . . . . .	38
4.4.1	Channel Loss . . . . .	38
4.4.2	$\mathcal{M}$ Atmospheric Turbulence Model . . . . .	39
4.4.3	Pointing Errors Models . . . . .	40

4.4.4	Composite Atmospheric Channel Model . . . . .	40
4.5	Statistical Characteristics of The End-to-end SNR, $\gamma_{e2e}$ . . . . .	41
4.5.1	Cumulative Distribution Function . . . . .	41
4.5.2	Probability Density Function . . . . .	43
4.5.3	Moment Generating Function . . . . .	44
4.5.4	Remarks . . . . .	44
4.6	Performance Analysis . . . . .	45
4.6.1	Outage Probability . . . . .	45
4.6.2	Average BER . . . . .	45
4.6.3	Average Capacity Analysis . . . . .	47
4.7	Numerical Results . . . . .	48
4.8	Conclusions . . . . .	53
5.	Two-Way Relaying FSO Systems . . . . .	54
5.1	Introduction . . . . .	54
5.2	System and Channel Models . . . . .	56
5.2.1	System Model . . . . .	56
5.2.2	Channel Model . . . . .	58
5.2.2.1	$\mathcal{M}$ Atmospheric Turbulence Model . . . . .	59
5.2.2.2	Pointing Errors Model . . . . .	60
5.2.2.3	Composite Atmospheric Channel Model . . . . .	61
5.3	Statistical Characterization of The End-to-end SNR, $\Gamma_{T_i}$ . . . . .	62
5.4	Performance Analysis . . . . .	65
5.4.1	Outage probability . . . . .	65
5.4.2	Average Bit Error Rate . . . . .	66
5.4.3	Ergodic Achievable-Rate . . . . .	67
5.5	Numerical Results . . . . .	70

5.6	Conclusions . . . . .	72
6.	Multihop Relaying WDM/FSO Systems . . . . .	74
6.1	Introduction . . . . .	74
6.1.1	Related Studies and Motivations . . . . .	75
6.1.2	Main Contributions . . . . .	76
6.2	Proposed System Descriptions . . . . .	77
6.2.1	Network Model . . . . .	77
6.2.2	System Model . . . . .	78
6.3	FSO Dispersive Turbulence Channel Model . . . . .	81
6.3.1	Atmospheric Dispersive Model . . . . .	81
6.3.2	Atmospheric Turbulence Model . . . . .	83
6.4	Bit-Error Rate Analysis . . . . .	84
6.4.1	Downstream Analysis . . . . .	87
6.4.2	Upstream Analysis . . . . .	87
6.5	Numerical Results . . . . .	88
6.5.1	Downstream Transmission . . . . .	88
6.5.2	Upstream Transmission . . . . .	92
6.6	Conclusions . . . . .	94
7.	Generalized Selection Combining in FSO Systems . . . . .	95
7.1	Introduction . . . . .	95
7.2	System and Channel Models . . . . .	97
7.2.1	System Model . . . . .	97
7.2.2	Channel Model . . . . .	98
7.3	GSC Output Statistics and Outage Probability . . . . .	100
7.3.1	MGF of GSC Output SNR . . . . .	100



7.3.2	CDF of GSC( $M, L$ ) Output SNR . . . . .	101
7.3.3	Outage Probability . . . . .	102
7.4	Numerical Results . . . . .	102
7.5	Conclusions . . . . .	104
8.	Summary and Future Research . . . . .	105
8.1	Summary . . . . .	105
8.2	Future Research . . . . .	108
8.2.1	Motivations . . . . .	108
8.2.2	Research Directions . . . . .	109
	Acknowledgements . . . . .	111
	Bibliography . . . . .	113
	Appendices . . . . .	130
Appendix A	A Proof of Theorem 1 in Chapter 7 . . . . .	130
Appendix B	A Proof of Lemma 1 in Chapter 7 . . . . .	132

# List of Figures

1.1	Organization of the thesis. . . . .	4
2.1	The evolution of wireless technologies [14]. . . . .	9
2.2	mmWave spectrum availability [26]. . . . .	12
3.1	Example of current backhaul connectivity in LTE 4G networks [4]. . . . .	15
3.2	Example of 5G mobile backhaul network consisting of fronthaul, midhaul, and traditional backhaul [4]. . . . .	16
3.3	Distributed ultra-dense cellular networks with a single gateway: a) the deployment scenario with a single gateway; b) the logical architecture with a single gateway [48]. . . . .	20
3.4	Distribution ultra-dense cellular network with multiple gateways: a) the deployment scenario with multiple gateways; b) the logical architecture with multiple gateways [48]. . . . .	20
3.5	A summary of wireless backhaul technologies in 5G [4]. † refers to [49], ‡ refers to [50] . . . . .	21
3.6	Our proposed architecture for 5G cellular networks [90]. . . . .	25
3.7	Possible backhaul connectivity subsystems. (a) Conventional fiber-based backhauling subsystem; (b) Fiber-mmWave RF backhauling subsystem; (c) Fiber-FSO backhauling subsystem; (d) FSO-FSO backhauling subsystem; (e) FSO-mmWave RF backhauling subsystem [90]. . . . .	29

4.1	Hybrid architecture for backhaul networks: (a) Standard backhauling connection utilizing OF and mmWave RF [48]; (b) Proposed connection utilizing FSO and mmWave RF. . . . .	33
4.2	Mixed mmWave RF/FSO with AF relay system model. . . . .	34
4.3	PDF plots for the exact expression in (4.5) and the approximation in (4.7). . . . .	37
4.4	CDF plots for the exact expression in (4.6) and the approximation in (4.8). . . . .	37
4.5	Outage probability versus the average SNR per hop ( $\bar{\gamma}_1 = \bar{\gamma}_2$ ) under different turbulence conditions, $\gamma_{th} = 0$ dB, $\xi = 1$ (i.e., strong pointing errors). . . . .	49
4.6	Outage probability versus the average SNR per hop ( $\bar{\gamma}_1 = \bar{\gamma}_2$ ) under different turbulence conditions, $\gamma_{th} = 0$ dB, $\xi = 6$ (i.e., weak pointing errors). . . . .	49
4.7	Outage probability versus the average SNRs of the RF ( $\bar{\gamma}_1$ ) and FSO links ( $\bar{\gamma}_2$ ) under the moderate turbulence condition, $\gamma_{th} = 0$ dB, $\xi = 1$ (i.e., strong pointing errors). . . . .	50
4.8	Outage probability versus the average SNRs of the RF ( $\bar{\gamma}_1$ ) and FSO links ( $\bar{\gamma}_2$ ) under the moderate turbulence condition, $\gamma_{th} = 0$ dB, $\xi = 6$ (i.e., weak pointing errors). . . . .	51
4.9	ABER versus the average SNRs per hop ( $\bar{\gamma}_1 = \bar{\gamma}_2$ ) under different turbulence conditions and pointing errors: systems employing BPSK. . . . .	51
4.10	ABER versus the average SNRs per hop ( $\bar{\gamma}_1 = \bar{\gamma}_2$ ) under different turbulence conditions and pointing errors: systems employing 4-QAM. . . . .	52
4.11	Average capacity versus the average SNRs per hop ( $\bar{\gamma}_1 = \bar{\gamma}_2$ ) under different turbulence conditions and pointing errors: strong turbulence. . . . .	52
4.12	Average capacity versus the average SNRs per hop ( $\bar{\gamma}_1 = \bar{\gamma}_2$ ) under different turbulence conditions and pointing errors: weak turbulence. . . . .	53
5.1	System model of a two-way all-optical AF relaying FSO system. . . . .	56
5.2	Outage probability for the two-way AF relaying FSO system at terminal $T_2$ under different turbulence and pointing errors conditions. . . . .	71

5.3	ABER for the two-way AF relaying FSO system at terminal $T_2$ with $\alpha_1 = \alpha_2 = 4.2$ , $\beta_1 = \beta_2 = 3$ , $\rho_1 = \rho_2 = 1$ . . . . .	72
5.4	Ergodic achievable-rate for the two-way AF relaying FSO system with varying atmospheric turbulence strength and pointing errors severity, $\rho_1 = \rho_2 = 0.596$ . . . . .	72
6.1	(a) PON optical fiber access network; (b) Proposed all-optical multi-hop WDM/FSO access network. . . . .	77
6.2	Multi-hop OAF relaying WDM/FSO systems for optical access networks.	79
6.3	Rytov variance versus the refractive structure index for different transmission distances. . . . .	84
6.4	Downstream transmission: BER versus the average transmitted power per information bit $P_s$ , with $R_b = 1$ Gbps, $L_{dx,XT} = -30$ dB, $L = 4$ km, and $C_n^2 = 5 \times 10^{-15}$ for different numbers of relays $N$ in systems using OOK (a) and 4-PPM (b). . . . .	89
6.5	Downstream transmission: BER versus the average transmitted power per information bit $P_s$ , with 4-PPM, $R_b = 1$ Gbps, $L_{dx,XT} = -30$ dB, and $L = 4$ km, for different turbulence strengths $C_n^2$ . . . . .	90
6.6	Downstream transmission: BER versus the transmission distance $L$ , $P_s = 0$ dBm, $R_b = 1$ Gbps, $L_{dx,XT} = -30$ dB, and $C_n^2 = 5 \times 10^{-15}$ for different numbers of relays (a) and orders of PPM modulation (b). . . . .	91
6.7	Downstream transmission: BER versus the transmission rate $R_b$ , $P_s = 0$ dBm, $L_{dx,XT} = -30$ dB, and $C_n^2 = 5 \times 10^{-15}$ , and $L = 4$ km for different orders of PPM modulation with $N = 1$ (a) and $N = 2$ (b). . . . .	92
6.8	Upstream transmission: BER versus the average transmitted power per information bit $P_s$ , with $L_{dx,XT} = -30$ dB (a) and $L_{dx,XT} = -15$ dB (b); $C_n^2 = 5 \times 10^{-15}$ , $M = 4$ , $N = 1$ , $L = 4$ km. . . . .	92
6.9	Upstream transmission: BER versus the average transmitted power per information bit $P_s$ , with different numbers of relays $N$ (a) and different PPM modulation orders $M$ (b); $L_{dx,XT} = -15$ dB, $d_{N+1,int} = 20$ m, $C_n^2 = 5 \times 10^{-15}$ , $L = 4$ km. . . . .	94

7.1	SIMO FSO System Model with GSC( $M,L$ ) Scheme. . . . .	97
7.2	Plots for PDFs (a) and CDFs (b), respectively in (7.2) and (7.3), under weak ( $C_n^2 = 6 \times 10^{-15}$ ), moderate ( $C_n^2 = 10^{-14}$ ), and strong ( $C_n^2 = 4 \times 10^{-14}$ ) turbulence conditions. . . . .	100
7.3	Outage probability versus the normalized average SNR per branch for GSC( $M,5$ ) under weak turbulence (a), and strong turbulence (b). . . .	103
7.4	Outage probability versus the transmission distance $d$ (km) for GSC( $M,5$ ) with $C_n^2 = 10^{-14}$ . . . . .	103
8.1	Future research: Relaying satellite-UAV-ground station for vertical backhaul/fronthaul in resilient 5G and beyond wireless networks. . . . .	110

# List of Notations

$\Gamma(\cdot)$	the ordinary Gamma function
$\gamma(\cdot, \cdot)$	the lower incomplete Gamma function
$K_\nu(\cdot)$	the modified Bessel function of second kind and order $\nu$ -th
$I_0(\cdot)$	the zero order modified Bessel function of the first kind
$Q_1(\cdot, \cdot)$	the Marcum $Q$ -function
$\operatorname{erfc}(\cdot)$	the complementary error function
$G_{p,q}^{m,n}[\cdot]$	the Meijer's $G$ -function

# List of Abbreviations

AF	Amplify-and-Forward
ABER	Average Bit Error Rate
APD	Avalanche Photo-Diode
AWGN	Additive White Gaussian Noise
BBU	Baseband Unit
BC	Broadcast
BER	Bit Error Rate
BPSK	Binary Phase Shift Keying
BS	Base Station
CDF	Cumulative Distribution Function
CSI	Channel State Information
DC	Direct Current
EGBMGF	Extended Generalized Bivariate Meijer's G-function
FSO	Free-Space Optics
GSC	Generalized Selection Combining
LTE	Long-Term Evolution
MA	Multiple Access
M-C	Monte-Carlo
MGF	Moment Generating Function
mmWave	Millimeter Wave
PDF	Probability Density Function
PPM	Pulse Position Modulation
PSK	Phase Shift Keying
QAM	Quadrature Amplitude Modulation
RAN	Radio Access Network
RF	Radio Frequency
RRH	Remote Radio Head
SI	Scintillation Index
SIMO	Single-Input Multiple-Outputs
SNR	Signal-to-Noise Ratio
WDM	Wavelength-division multiplexing

# Abstract

Current cellular backhaul networks are mostly built with microwave links and fiber/copper-based links, which cannot cope with the capacity, latency, reliability, energy efficiency, and cost effectiveness required for the fifth generation (5G) of mobile networks. Therefore, the 5G backhaul research has been triggered, aiming at bridging the gap between the requirements stipulated by the 5G radio access network (RAN) and the realistic backhaul capabilities, from two different perspectives. The first consists of evolving the current backhaul (microwave, optical fiber, copper, etc.) to meet 5G expectations and encompassing new wireless technologies such as millimeter-wave (mmWave) and free-space optics (FSO). The other backhaul research perspective looks at adapting the 5G RAN to the available backhaul with realistic performance, such as investigating intermediate RAN architectures between the centralized RAN and the distributed RAN to fit the backhaul/fronthaul capabilities. In this thesis, the main focus is on the channel modeling of the disruptive wireless technologies, including mmWave and FSO, for 5G backhaul networks.

To enable the mixture of mmWave and FSO, how to accurately capture the channel characteristics of both mmWave and FSO under various transmission conditions for performance evaluation is very important. To do so, the following problems need to be addressed. Firstly, the analysis with different channel models and effects induced by physical layer impairments would result in highly complex analytical problems. Secondly, the effectiveness of different signal processing and coding techniques needs to be investigated to optimize the performance of the mixed systems. Finally, comprehensive experimental implementation should be conducted to validate the analytical models and performance results.

To derive the analytical model for performance analysis, we strive to formulate



mathematical models describing the effects of transmission channels and study the statistical characterization of the end-to-end signal-to-noise ratio (SNR) of the mixed systems. On the other hand, improvement techniques suitable for the mixture of mmWave and FSO systems are proposed, including including two-way communications, relaying techniques, and diversity reception with generalized selection combining (GSC). Furthermore, comprehensive computer-based experiments using practical channel data and Monte-Carlo simulations are implemented to evaluate the accuracy of the derived analytical model and performance results.



# Chapter 1

## Introduction

### 1.1. Motivations

Mobile traffic has significantly increased over the last decade mainly due to the stunning expansion of smart wireless devices and bandwidth-demanding applications. It is expected that the fifth generation (5G) of cellular networks is able to achieve 1000 times the system capacity, 10 times the spectral/energy efficiency, 10-100 times the data rate, and 25 times the average cell throughput, compared to the fourth generation (4G) networks [1]. Current cellular networks that are based on macrocells and mostly built with microwave links and fiber/copper-based links, cannot cope with the capacity, latency, reliability, energy efficiency, and cost effectiveness required for the 5G mobile networks. To increase the network capacity for supporting high-density mobile users with high-speed data services, the inevitable trend is the deployment of smaller cells (i.e., picocells and femtocells). This results in a larger number of smaller cells in the radio access network (RAN) producing massive data traffic. The massive data traffic from the small cells shall be connected to the core network through the backhaul network with extreme requirements in terms of capacity, latency, reliability, energy efficiency, and cost effectiveness. The most viable solution to realize such a backhaul network would involve the use of an optical fiber (OF) cable. However, the associated cost and challenge of deploying fiber to each picocell and femtocell site

is prohibitive, especially in urban areas. Wireless links, on the contrary, can provide a cost-effective fiber alternative to interconnect the outlining areas beyond the reach of the fiber rollout. In particular, the unbalanced temporal and geographical variations of spectrum usage along with the rapid proliferation of bandwidth-hungry mobile applications, such as video streaming with high definition television (HDTV) and ultra-high definition video (UHDV), have inspired millimeter-wave (mmWave) [2], and free space optics (FSO) [3] communications as promising technologies to alleviate the pressure of scarce spectrum resources for 5G mobile broadband.

Motivated by the above discussion, the 5G backhaul research has been triggered, aiming at bridging the gap between the requirements stipulated by the 5G RAN and the realistic backhaul capabilities, from two different perspectives. The first consists of evolving the current backhaul to meet 5G expectations and encompassing new wireless technologies such as mmWave and FSO. The other backhaul research perspective looks at adapting the 5G RAN to the available backhaul with realistic performance, such as investigating intermediate RAN architectures between the centralized RAN and the distributed RAN to fit the backhaul/fronthaul capabilities [4]. In this thesis, we follow the former research perspective, focusing on evolving the current backhaul by deploying disruptive wireless technologies (mmWave and FSO) in combination with OF to meet the extreme requirements of the future 5G backhaul networks.

## 1.2. Original Contributions

Our argument is that none of the above-mentioned backhaul technologies can be a stand-alone solution. OF is still the suitable choice for mobile backhaul upper-tier connections, whereas mmWave and FSO are more preferable for the high-density small cells. However, both mmWave RF and FSO suffer from their own issues which are the high path loss and sensitivity to weather conditions (mmWave), and atmospheric turbulence together with pointing errors due to the misalignments between transmitters and receivers (FSO). We therefore propose a hybrid architecture for the 5G-backhaul networks utilizing both wired (OF) and wireless (mmWave/FSO) con-

nections to provide a cost-effective, scalable, reliable, and high-capacity connectivity in the future heterogeneous network (HetNet) with the ability to dynamically adjust and adapt to the changes in the network in a flexible, efficient, and timely manner. The objectives of our proposed research are threefold.

1. Firstly, the hybrid architecture is able to satisfy the extreme requirements in 5G backhaul networks, due to the advantageous nature of all three technologies (OF, mmWave, and FSO).
2. Secondly, the combined usage of relaying FSO/mmWave and/or FSO/FSO systems could ensure the resilience of the wireless-based backhaul networks under various atmospheric and weather conditions.
3. Thirdly, we strongly advocate the use of FSO for solving the spectrum scarcity and interference issues in the radio wireless-based backhaul networks. FSO could also be seamlessly connected with OF to form an all-optical high-capacity and low latency backhaul link.

To achieve the aforementioned goals, we first develop the concept of hybrid systems for 5G backhaul networks, which are different combinations of all three technologies (OF/mmWave/FSO). From these basic hybrid-systems, various extensions (e.g., multihop relaying systems [5], [6]) and combinations (mixed/parallel systems [7], [8]) can be developed. Based on different combinations of OF/mmWave and FSO, we focus on channel modeling and analytical frameworks to study the performance limits of the considered hybrid-systems. To enhance the system performance, we investigate the use of improvement techniques (including two-way communications, relaying techniques, diversity reception with generalized selection combining) for the hybrid systems. The experimental implementation by computer-based Monte-Carlo simulations is also conducted to validate the accuracy of analytical results. In this thesis, our *key contributions* is the derivation of analytical solutions and the performance analysis of different systems for backhaul networks (e.g., relaying mmWave/FSO,

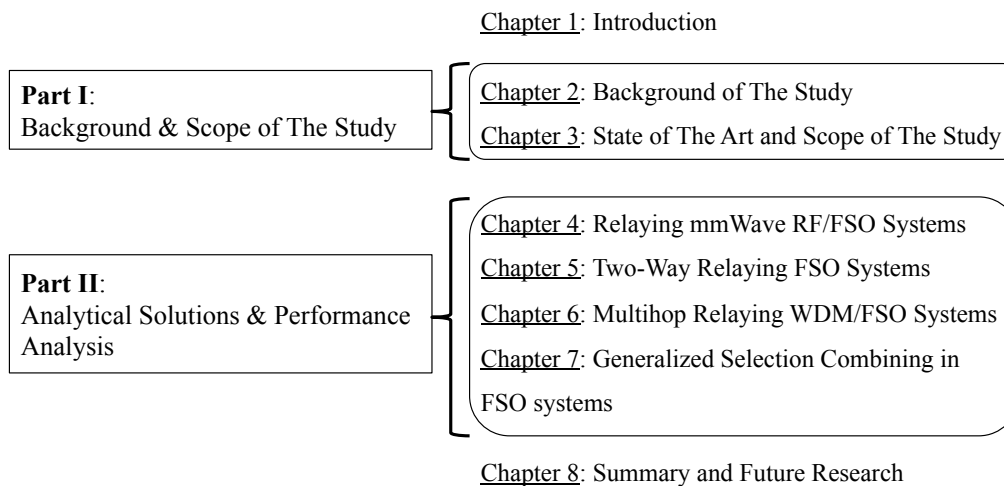


**Figure 1.1:** Organization of the thesis.

FSO/FSO). Several performance metrics including the outage probability, the average bit error rate, and the average capacity will be investigated.

Apart from the contributions appeared in this thesis, we also investigated the application of quantum key distribution (QKD) in FSO systems, which has the potential to provide a secure connection in the future optical backhaul networks. For further reading, please refers to [9]- [11].

### 1.3. Thesis Organization

The remainder of this thesis is organized in two parts, as illustrated in Fig. 1.1. Details of each part are highlighted as follows.

#### **Part I: Background and Scope of the Study**

This part includes Chapters 2 and 3, which are dedicated to introduce the background knowledge of wireless cellular networks and review the state of the art as well as the scope of our study on the cellular backhaul networks. More specifically, Chapter 2 summarizes the evolution of wireless cellular networks from the first-generation (1G) to current 4G cellular networks. With the ever-increasing in the number of Internet mobile devices, current 4G networks expose several issues and challenges in coping with the extreme requirements of the future cellular networks. In the near future, i.e., beyond 4G, some of the prime objectives or demands that need to be addressed

are increased capacity, improved data rate, decreased latency, and better quality of service. To meet these demands, drastic improvements need to be made in cellular network architecture. Cellular densification with ultra-dense deployment of base stations in a large number of small cells is considered as the key solution, which triggered many studies on emerging technologies that can be used in 5G wireless systems to fulfill the probable performance desires. Nevertheless, a new bottleneck has emerged in the current backhaul networks. The ultra-dense and heavy traffic from small cells should be connected to the core network through the backhaul, with extreme requirements in terms of capacity, latency, availability, energy, and cost efficiency. Chapter 3 reviews the state-of-the-art of 5G wireless backhaul technologies and focuses on the applications of enabling wireless technologies including mmWave and FSO for 5G backhaul networks. Furthermore, a hybrid architecture is introduced for 5G-backhaul networks utilizing both wired (OF) and wireless (mmWave/FSO) connections to provide a cost-effective, scalable, reliable, and high-capacity connectivity in the future heterogeneous network (HetNet) with the ability to dynamically adjust and adapt to the changes in the network in a flexible, efficient, and timely manner. From the hybrid architecture, various hybrid combinations of transmission technologies form different systems for 5G backhaul networks, which could be implemented according to the practical need in the deployment areas.

#### **Part II: Analytical Solutions and Performance Analysis**

This part includes Chapters 4, 5, 6 and 7, which focus on our *key contributions* of deriving analytical solutions and analyzing the performance of different systems for backhaul networks (e.g., relaying mmWave/FSO, FSO/FSO). Several performance metrics including the outage probability, the average bit error rate, and the average capacity will be investigated.

Chapter 4 studies the performance of mixed mmWave RF/FSO systems as a highly scalable and cost-effective solution for the 5G mobile backhaul networks. The mmWave RF and FSO fading channels are respectively modeled by the Rician and the generalized Malaga ( $\mathcal{M}$ ) distributions. The effect of pointing errors due

to the misalignments between the transmitter and the receiver in the FSO link is also included. Novel accurate closed-form expressions for the cumulative distribution function (CDF), the probability density function (PDF), and the moment generating function (MGF) in terms of Meijer's G functions are derived. Capitalizing on these new results, we analytically derive precise closed-form expressions for various performance metrics of the proposed system including the outage probability, the average bit error rate (ABER), and the average capacity. Additionally, new asymptotic results are provided for the outage probability, the MGF, and the ABER in terms of simple elementary functions by applying the asymptotic expansion of the Meijer's G function at high signal-to-noise ratios (SNR). Numerical results further validate the mathematical analysis by Monte-Carlo (M-C) simulations. The contributions in this chapter were originally published in [7].

Chapter 5 studies the implementation of two-way transmission in an amplify-and-forward (AF) relaying FSO system utilizing a relay with optical amplifier. Two-way transmission protocol is an efficient method to overcome the spectral loss incurred due to half-duplex communication. The performance of the proposed FSO system using subcarrier intensity modulation (SIM) with intensity modulation/direct detection (IM/DD) over independent but not necessarily identically distributed (i.n.i.d) Malaga ( $\mathcal{M}$ ) atmospheric turbulence channels in presence of pointing errors is studied. Exact closed-form expressions for the moment generating function (MGF) and cumulative distribution function (CDF) of the end-to-end signal-to-noise ratio (SNR) are obtained in terms of extended generalized bivariate Meijer's G-functions (EGBMGF). Capitalizing on these new results, we derive exact closed-form expressions for various performance metrics of the considered FSO system including the outage probability, the average bit error rate (ABER), and the ergodic achievable-rate. All analytical results are thoroughly confirmed by M-C simulations. The contributions in this chapter were originally published in [12].

Chapter 6 newly proposes and theoretically analyzes the performance of multi-hop FSO systems employing optical amplify-and-forward (OAF) relaying technique



and wavelength division multiplexing (WDM). The proposed system can provide a low cost, low latency, high flexibility, and large bandwidth access network for multiple users in areas where installation of optical fiber is unfavorable. In WDM/FSO systems, WDM channels suffer from the interchannel crosstalk while FSO channels can be severely affected by the atmospheric turbulence. These impairments together with the accumulation of background and amplifying noises over multiple relays significantly degrade the overall system performance. To deal with this problem, the use of the  $M$ -ary pulse position modulation ( $M$ -PPM) together with the OAF relaying technique is advocated as a powerful remedy to mitigate the effects of atmospheric turbulence. For the performance analysis, we use a realistic model of Gaussian pulse propagation to investigate major atmospheric effects, including signal turbulence and pulse broadening. We qualitatively discuss the impact of various system parameters, including the required average transmitted powers per information bit corresponding to specific values of bit error rate (BER), transmission distance, number of relays, and turbulence strength. Our numerical results are also thoroughly validated by M-C simulations. The contributions in this chapter were originally published in [13].

Chapter 7 investigates the outage performance of generalized selection combining (GSC) receiver that combines a subset of  $M$  strongest branches in terms of instantaneous signal-to-noise ratio (SNR) out of  $L$  available branches, i.e.  $GSC(M,L)$ , for coherent free-space optical (FSO) communication systems. A closed-form solution for the moment generating function (MGF) of the  $GSC(M,L)$  output SNR is concisely derived when the total received signal experiences independent and identically distributed (i.i.d.) atmospheric turbulence-induced fading, modeled by a mixture-Gamma distribution. As a result, the outage probability of the GSC receiver for coherent FSO systems is obtained and comprehensively studied. Numerical results show the crucial role of selected diversity branches under the effect of atmospheric turbulence channels, which are further verified by M-C simulations.

Finally, Chapter 8 concludes the thesis with a summary and outlooks on the future research directions.

# Chapter 2

## Background of The Study

### 2.1. Introduction

Over the years, mobile wireless communications has evolved from analog voice calls to current digital technologies, which are able to provide various services with data rates up to megabits per second. This rapid development in mobile communications as well as the ever-increasing number of Internet mobile devices, e.g. smart phones, tablets, and laptops, leads to the exponential growth in broadband traffic. This chapter summarizes the evolution as well as the state-of-the-art of wireless communications technologies towards the future 5G networks.

### 2.2. A History of Wireless Cellular Networks

The history of wireless cellular networks started when the well-known Italian inventor Marconi successfully communicated the letter ‘S’ encoded by the three-dot Morse code along a distance of 3 km, using electromagnetic waves. Since then, wireless communications has been evolving and becoming a crucial part of the society nowadays. As summarized by Gupta *et al.*, the evolution of wireless is shown in Fig. 2.1 [14]. It is seen that wireless technologies explicitly develop in terms of data rate, mobility, coverage, and spectral efficiency. At a glance, we can also see in Fig. 2.1 the key

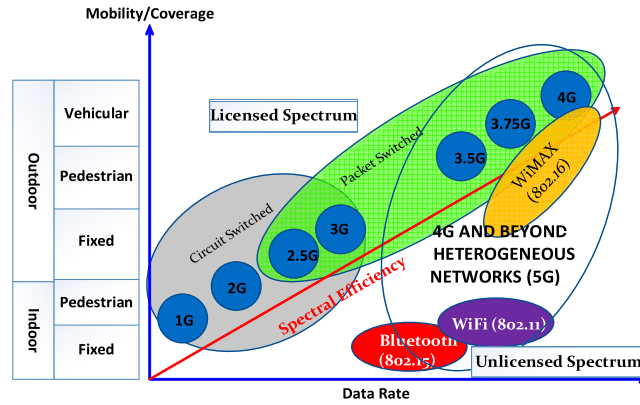


**Figure 2.1:** The evolution of wireless technologies [14].

technology used in each generation of wireless cellular networks, which reveals the evolution from circuit switching to packet switching networks. A brief review of this evolution is presented as follows.

### 2.2.1. The First Generation (1G)

The 1G dated back in 1980's. The data rate was up to 2.4 kbps and major subscribers were Advanced Mobile Phone System (AMPS), Nordic Mobile Telephone (NMT), and Total Access Communication System (TACS). At that time, 1G has a lot of disadvantages, for example, low capacity, reckless handoff, high interference, and no security as voice calls were stored and played in radio towers [15].

### 2.2.2. The Second Generation (2G)

The 2G was later appeared in late 1990's, with the evolution to the use of digital technologies. The first 2G system is called Global Systems for Mobile communications (GSM), with data rate up to 64 kbps. Some important technologies were Code Division Multiple Access (CDMA) and IS-95. An advancement of 2G is 2.5G with the introduction of packet switching along with circuit switching, supporting data rate up to 133 kbps. The eminent technologies in 2.5G were General Packet Radio Services (GPRS), Enhanced Data Rate for GSM Evolution (EDGE), and Code Division Multiple Access (CDMA) 2000 [15].

### **2.2.3. The Third Generation (3G)**

In late 2000, the 3G was first introduced with the capability of providing data rate up to 2 Mbps, which merged high-speed mobile access to Internet Protocol (IP)-based services. In addition, global roaming and improved voice quality were made possible in 3G. However, the major disadvantage in 3G handsets was the increase in power requirement, compared to that in 2G. With some added improvement, 3.5G is able to support data rate of up to 5-30 Mbps by utilizing advanced technologies like High Speed Uplink/Downlink Packet Access (HSUPA/HSDPA) and Evolution-Data Optimized (EVDO). 3.5G also plays the role of an intermediate generation bridging 3G and the fourth generation [15].

### **2.2.4. The Fourth Generation (4G)**

The 3rd Generation Partnership Project (3GPP) standardizes Long Term Evolution (LTE) Advanced as standards for 4G along with Mobile Worldwide Interoperability for Microwave Access (WIMAX). The additional advancement in 4G is to impart a complete solution based on IP, in which voice, data, and multimedia are imparted to subscribers on every time and everywhere basis, while supporting sufficiently high data rates, compared to previous generations. Some eminent applications available in 4G networks are Multimedia Messaging Service (MMS), Digital Video Broadcasting (DVB), and video chat, High Definition TV content and mobile TV [16].

### **2.2.5. Issues and Challenges of Existing Cellular Networks**

According to some recent reports by Cisco, the global mobile traffic witnessed a growth of 70% in 2014, and will continue to grow exponentially as mobile networks will have more than half of connected devices as smart devices in 2019 [17]. For example, it is predicted that an average mobile user will download around 1 terabyte of data annually by 2020 [18]. Moreover, some advanced technologies are being in-

investigated for the future communication networks, such as Internet of Things (IoT), Internet of vehicles (IoV), Device to Device (D2D) communications, e-healthcare, Machine to Machine (M2M) communications and Financial Technology (FinTech). This rapid development of novel technologies will require an enormous amount of data usage in the network, which certainly becomes a challenging issue in current 4G LTE cellular networks. Illustratively, with a theoretical 150 Mbps maximum down-link data rate, traditional LTE systems, with  $2 \times 2$  MIMO can support only up to  $(150/4)$  simultaneous full HD (at 4 Mbps rate) video streaming. This cannot cope with the increasing demand in the future. Furthermore, as a standard LTE network was originally designed to support up to 600 connected users per cell [19], [20], it cannot support requirements of connected devices in M2M communications and IoT (tens of thousands of connections in a single cell). This enormous number of connected devices will produce a huge amount of data traffic, which will be the primary concern in the evolution of the next-generation networks. Therefore, the crucial goal is *to satisfy the exponential rise in the number of users and traffic capacity in mobile broadband communications.*

## 2.3. The Fifth Generation (5G)

### 2.3.1. A New Horizon in Radio Spectrum

As clarified in the previous section, the important goal in the next-generation networks is to increase the network capacity to support a large number of users with broadband services. In wireless communications, capacity depends on spectral efficiency, bandwidth, and cell size [21]. Over the evolution of mobile networks, cell sizes are getting smaller and technologies at physical layer is currently at the boundary of Shannon capacity [22]. However, the system bandwidth still remains untouched. Currently, wireless communications utilize spectrum in 300 MHz to 3 GHz band, namely sweet spot or beachfront spectrum [18], [23]. The main advantage of this frequency

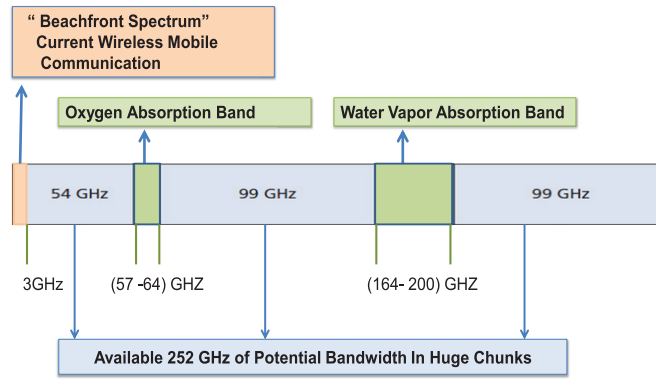


**Figure 2.2:** mmWave spectrum availability [26].

band is the reliability of the signals propagating over several kilometers in different environments [18], while the sub millimeter-wave (mmWave) band to cope with the increasing mobile traffic remains unexplored [24]. Therefore, the most important advancement of next generation 5G wireless networks lies in exploring this unused, high frequency mmWave band, ranging from 3-300 GHz. Historically, mmWave spectrum was utilized in collision avoidance in radars, in the spectrum between 59-64 GHz and 81-86 GHz for unlicensed wireless and peer to peer communications respectively [25]. As shown in Fig. 2.2 [26], only 57-64 GHz and 164-200 GHz is un-suitable for communications, in the huge 3-300 GHz mmWave spectrum. More importantly, even a small fraction of available mmWave spectrum can support hundreds of times of more data rate and capacity, compared to the current cellular spectrum [24]. Thus, the utilization of mmWave spectrum is opening up a new horizon in radio spectrum for coping with the exponential need in capacity of the future wireless communications [24], [25].

### 2.3.2. 5G Visions

In addition to the emergence of mmWave spectrum, hyper-connected vision and new application-specific requirements are going to trigger the next major evolution in wireless communications with new targeted performance for 5G [23], [27], [28]. 5G wireless communications envision magnitudes of increase in wireless data rates, bandwidth, coverage and connectivity, with a massive reduction in round trip latency

and energy consumption. It is expected that the first standard will be mature by 2020. Group Special Mobile Association (GSMA) is working with its partners towards the standardization of 5G. In the following, eight major requirements of the future 5G networks are introduced, which unify the suggestions from different research initiatives by industries and academia [23], [27], [29].

1. 1 - 10 Gbps data rates in real networks: This is almost 10 times increase from traditional LTE networks theoretical peak data rate of 150 Mbps.
2. 1 ms round trip latency: Almost 10 times reduction from 4Gs 10 ms round trip time.
3. High bandwidth in unit area: It is needed to enable large number of connected devices with higher bandwidths for longer durations in a specific area [27].
4. Enormous number of connected devices: In order to realize the vision of IoT, emerging 5G networks need to provide connectivity to thousands of devices [27].
5. Perceived availability of 99.999%: 5G envisions that network should practically be always available.
6. Almost 100% coverage for anytime anywhere connectivity: 5G wireless networks need to ensure complete coverage irrespective of users locations [27].
7. Reduction in energy usage by almost 90%: Development of green technology is already being considered by standard bodies. This is going to be even more crucial with high data rates and massive connectivity of 5G wireless [27].
8. High battery life: Reduction in power consumption by devices is fundamentally important in emerging 5G networks [27].

## 2.4. Conclusions

In this chapter, a history of the evolution of wireless cellular networks was briefly reviewed. With the ever-increasing in the number of Internet mobile devices,

current 4G networks expose several issues and challenges in coping with the extreme requirements of the future cellular networks. As a result, the evolution to 5G is inevitable and the performance requirements of 5G wireless cellular communication systems have been defined in terms of capacity, data rate, spectral efficiency, latency, energy efficiency, and Quality of service. Cellular densification with ultra-dense deployment of base stations in a large numbers of small cells is considered as the key solution, which triggered many studies on emerging technologies that can be used in 5G wireless systems to fulfill the probable performance desires. This chapter showed the big picture on the development of future 5G networks.



# Chapter 3

## State of the Art and Scope of the Study

### 3.1. Introduction

In current mobile cellular networks, the term *backhaul* refers to the network part that connects the e-Node B (eNB) to the core network. The current backhaul networks are mostly built with optical fiber, copper, microwave, and/or satellite links. In pre-LTE, the radio controller node often acts as a backhaul aggregation point to

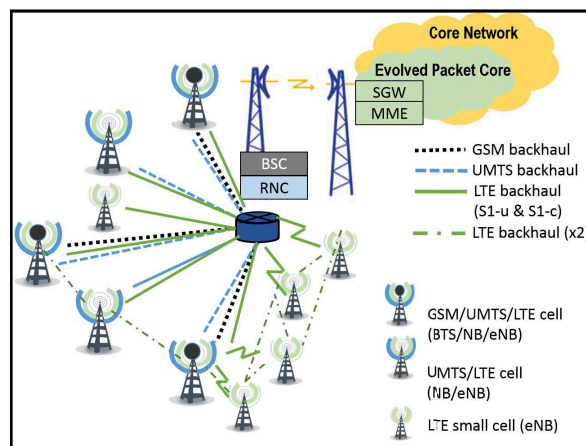


**Figure 3.1:** Example of current backhaul connectivity in LTE 4G networks [4].

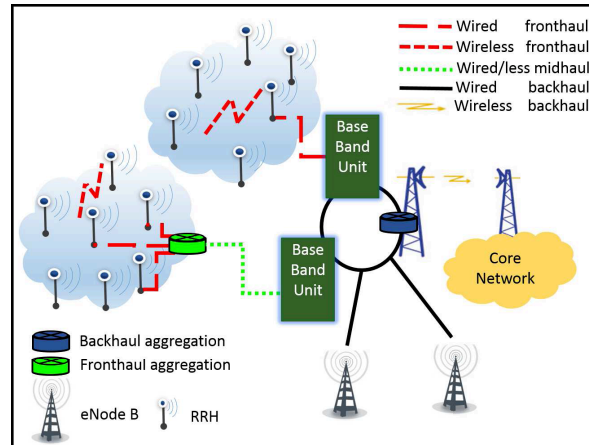


**Figure 3.2:** Example of 5G mobile backhaul network consisting of fronthaul, midhaul, and traditional backhaul [4].

concentrate backhaul connections from the neighboring radio stations towards the core network, as shown in Fig. 3.1 [4]. In LTE architectures, the radio controller node is removed, yet the backhaul aggregation is still desirable for wired/wireless connections.

As a part of the evolution to 5G networks, cloud radio access network (C-RAN), sometimes referred to as Centralized-RAN, has been introduced as the key architecture for future cellular networks, which consists of *fronthaul*, *midhaul*, and *backhaul*, as illustrated in Fig. 3.2 [4]. In C-RAN, the backhaul networks connect the remote radio head (RRH) directly to the baseband unit (BBU), or to an intermediate aggregation point which is named as fronthaul. The basic fronthaul is assumed to run over a common public radio interface (CPRI) separating the RRH from the BBU. Some novel fronthaul interfaces are being explored including the fronthaul-lite [30], next-generation fronthaul interface (NGFI) [31], and xHaul [32]. Based on the 3GPP terminology, the inter-eNB X2-based interface is called the midhaul [33]. The network connections between aggregation points and the core, based on the S1-interface [33], have retained the term backhaul. In this chapter, we use the term ***backhaul*** to refer to the entire transport network including midhaul and fronthaul.

To provide bandwidth up to 10 Gbps with low latency (hundreds of microseconds), optical fiber stands out as the only viable solution [34]. However, deploying

fiber cable is not always possible and economical. As a result, the research on 5G backhaul has been triggered, aiming at bridging the gap between the requirements stipulated by the 5G RAN and the realistic backhaul capabilities from two different perspectives. The first consists of evolving the current backhaul (microwave, optical fiber, copper, etc.) to meet 5G expectations and encompassing new wireless technologies such as in-band links (reuse the radio access spectrum), mmWave, free space optical communications (FSO), and sub-6GHz (e.g. WiMAX, WiFi). The other backhaul research perspective looks at adapting the 5G RAN to the available backhaul with realistic performance, such as investigating intermediate RAN architectures between the C-RAN and the distributed RAN (D-RAN) to satisfy the backhaul capabilities [30], [32], [35].

### 3.2. Backhaul Networks: State of the Art

Recently, the 5G cellular network is becoming a hot research topic, as telecommunication companies and academia are trying to look for solutions to meet  $1000\times$  wireless traffic volume increment in the next decade. There are several solutions were proposed. First, massive multiple-input multiple-output (MIMO) technology was proposed to improve the spectrum efficiency of 5G mobile communication systems [36]. Second, mmWave communications was presented to extend the transmission bandwidth for 5G mobile communication systems [37]. Furthermore, the cell is getting smaller to increase throughput and save energy consumption [38]. To satisfy seamless coverage, the density of 5G BSs is predicted to be 40-50 BSs/km<sup>2</sup>, which is densely deployed in a single cell. Therefore, the 5G cellular network is an *ultra-dense cellular network*.

Some initial studies on ultra-dense deployment of wireless networks were explored in [39]- [47]. More specifically, Yunas *et al.* investigated the spectrum and energy efficiency of ultra-dense wireless networks under different deployment strategies [39]. Soret *et al.* studied the interference issues of LTE-A cellular networks, and two algorithms applying time domain and frequency domain small cell interfer-

ence coordination were proposed [40]. To exploit network densification as a resource, a joint coordinated intra-cell and inter-cell resource allocation mechanism was proposed in [41]. Some advantages of network densification are discussed for 5G networks in [42]. On the other hand, a new architecture was proposed by using small cells to cope with massive and dense machine-type communication (MTC) rollout in [43]. As concluded in [42], [43], these dense wireless networks are complementary to existing macrocell networks.

To deal with backhaul traffic issues in ultra dense small-cell 5G networks, centralized and distributed wireless backhaul network architectures were compared in [44]. In this work, simulation results suggested that the distributed wireless backhaul network architecture is more suitable for future 5G networks employing massive MIMO antennas and mmWave technologies. It is noted that the distributed wireless backhaul network architecture was originally discussed for IEEE 802.16 mesh networks in [45]. As the radius of IEEE 802.16 BSs is typically 1500 m, which is much larger than the 50-100 m radius of small cells, IEEE 802.16 mesh networks are not considered as ultra-dense wireless networks. As a result, the small cell density deployment bottleneck is not a problem for IEEE 802.16 mesh networks.

As mmWave is emerging as a possible technology for 5G cellular networks, many studies on mmWave in 5G backhaul focused on the design of the antenna array and RF components [46], [47]. To deal with the pointing error issues due to the misalignment between transceivers, an efficient beam alignment technique was proposed for implementation in small cell networks [46]. The feasibility of mmWave connectivity for 5G backhaul over short- and medium-distance was investigated in [47].

### 3.2.1. Conventional Architecture

Conventionally, in cellular network architecture, the BS managers in the core network control every macrocell base station (BS). All traffic from the backhaul is then forwarded to the core network through a gateway. For conventional cellular

network with microcell deployment (e.g., femtocell, picocell), a hybrid architecture was presented, in which the backhaul traffic from microcell BSs is forwarded to the core network by a broadband Internet or optical fiber links. The coverage of microcells and macrocells is overlapped and both micro- and macro-cells independently transmit user data and management data to associated users, respectively. In this network architecture, the microcell network plays the role as a complementary to the conventional macrocell network to satisfy high-speed wireless backhauling in partial regions [47].

### 3.2.2. 5G Ultra-Dense Architecture

With the introduction of massive MIMO antenna and mmWave technologies, the preferable deployment in 5G networks is the densification of small cells. As a result, deploying backhaul links to forward massive traffic from a large number of small cell BSs becomes very challenging. Optical fiber links are the potential solution, however, they are costly and difficult to deploy densely urban environments. In addition, the small cell BS usually cannot forward backhaul traffic directly to the gateway, due to the constraint of short- and medium- distances in mmWave technology. A solution for this issue is relaying techniques, where the backhaul traffic is relayed through multiple shorter hops to the gateway. This naturally leads to a new form of architecture for 5G ultra-dense cellular networks, namely, a distributed network architecture. In this distributed architecture, the macrocell BS is configured to only transmit the management data to control handover in small cells, while small cell BS forwards user data traffic. This is the key difference of 5G distributed architecture in comparison to conventional one. The small cell network is does not play the role as a complement for the macrocell network. From the configuration of the backhaul gateway, two distributed architectures of ultra-dense cellular networks have been introduced as follows [48].

1. **Ultra-Dense Cellular Networks with a Single Gateway:** When only a single gateway is deployed in the macrocell, the corresponding scenario and

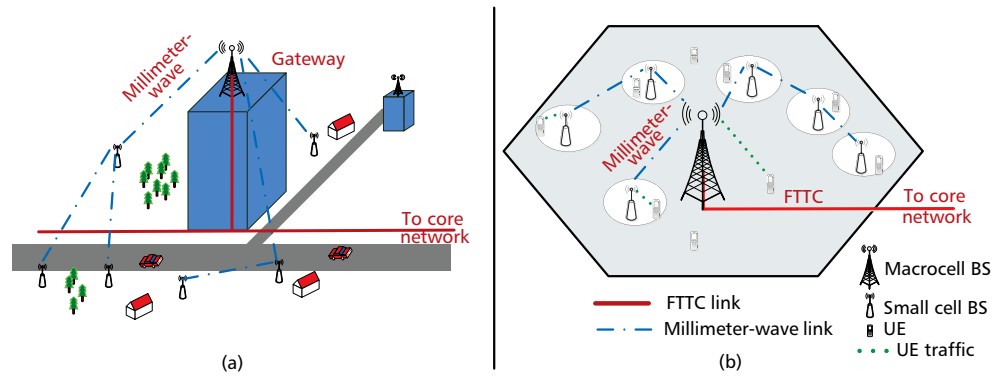


**Figure 3.3:** Distributed ultra-dense cellular networks with a single gateway: a) the deployment scenario with a single gateway; b) the logical architecture with a single gateway [48].

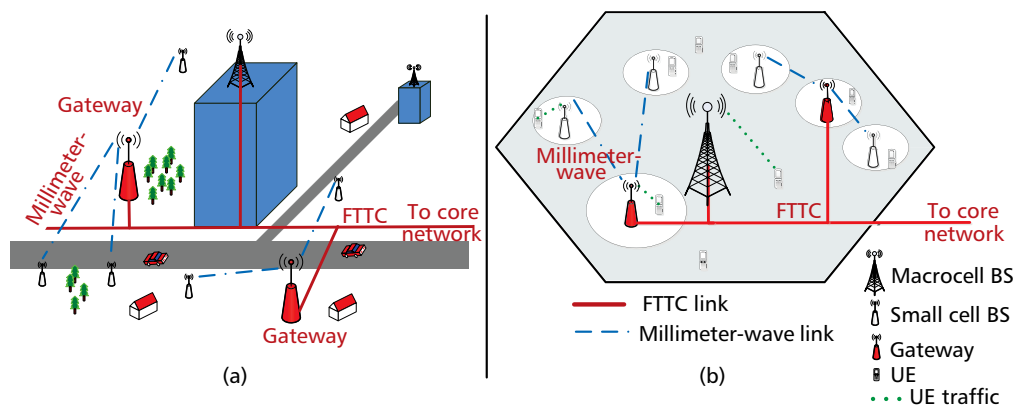


**Figure 3.4:** Distribution ultra-dense cellular network with multiple gateways: a) the deployment scenario with multiple gateways; b) the logical architecture with multiple gateways [48].

logical figures are illustrated in Fig. 3.3 [48]. It is assumed that the gateway is located at the macrocell BS and eligible to install massive MIMO mmWave antennas for receiving backhaul traffic from a number of small cells within the macrocell. From every small cell BS, the backhaul traffic is relayed and eventually forwarded to the gateway at the macrocell BS through multiple relaying hops using mmWave links. After all backhaul traffic is aggregated at the gateway, it is finally forwarded to the core network by fiber to the cell (FTTC) links.

2. **Ultra-Dense Cellular Networks with Multiple Gateways:** When multiple gateways are deployed in different small cell BSs, the corresponding sce-

### 3.2 Backhaul Networks: State of the Art

Technology	Options	Upstream throughput	Downstream throughput	Latency/ Jitter	Distance	Note
Microwave PtP †	PtP	1 Gbps	1 Gbps	< 1 msec/ hop	2-4 km	6-60 GHz remote not-spot
Microwave PtmP †	PtmP	1 Gbps	1 Gbps	< 1 msec/hop	2-4 km	6-60 GHz peppered capacity
Satellite †	LOS	15 Mbps	50 Mbps	300 msec one-way latency 5-30 msec jitter	~ubiquitous	due to cost per Mbps realistic Tput 2-10 Mbps DL/1-2 Mbps UL
TVWS †	NLOS	18 Mbps/ch	18 Mbps/ch	10 msec	1-5 km	up to 4 channels up to 10 km at 10 Mbps using 2 ch with LOS
mmWave 60 GHz †	LOS	1G bps	1 Gbps	200 $\mu$ sec	1 km	scalable
mmWave 70-80 GHz †	LOS	10 Gbps	10 Gbps	65-350 $\mu$ sec	3 km	scalable
Sub-6GHz 800 MHz-6 GHz †	NLOS	170 Mbps	170 Mbps	5 msec single hop one way	1.5-2.5 km urban 10 km rural	licensed (20 MHz TDD) expected to increase to 400 Mbps
Sub-6 GHz 2.4, 3.5, 5 GHz †	NLOS	150-450 Mbps	150-450 Mbps	2-20 msec	250 m	unlicensed data rate depends on MIMO
FSO ‡	LOS	10 Gbps	10 Gbps	low	1-3 km	

**Figure 3.5:** A summary of wireless backhaul technologies in 5G [4]. † refers to [49], ‡ refers to [50]

nario and logical figures are shown in Fig. 3.4. This architecture provides more flexibility to forward backhaul traffic into the core network. Unlike the single gateway configuration, the backhaul traffic is aggregated at different gateways located at small cell BSs. The aggregated traffic at a specified gateway at a small cell BS is then forwarded into the core network by FTTC links. All relaying paths are deployed by mmWave links to deliver user data traffic to/between multiple gateways.

#### 3.2.3. Technologies

Current backhaul networks are mostly built with microwave links and fiber/copper-based links. According to [51], fiber to the home (FTTH) is scarce worldwide with only 16 countries exceeding 15% FTTH penetration. This poses an urgent need for new backhaul technologies to support the extreme requirements in 5G networks. To this end, a number of backhauling technologies have been summarized in Fig. 3.5 [4]. Two types of links are introduced, including Point-to-point (PtP) and Point-to-multi-point (PtmP) links, which are suitable for deployment in various scenarios. PtP links are suitable to be mounted in chain, tree, ring or mesh networks, for in-

stance, but the incurred delay will increase with link length, the number of hops, and delay in aggregation/demultiplexing points. In contrast, PtmP enables easy addition/deletion/modification of nodes while relaxing the dependency of the network performance on the number of aggregation nodes.

Among wireless solutions for future backhaul in 5G networks, mmWave and FSO stand out as potential candidates. In the following sections of this chapter, detailed reviews of studies on the applications of mmWave and FSO for 5G backhaul will be presented, which give a big picture of the development of these important disruptive wireless technologies for the future 5G backhaul.

### 3.2.3.1. mmWave Backhauling Technologies

To enhance the capacity for future usage of 5G, a large chunk in the 60-100 GHz spectrum remains untouched and emerges as a promising option. This spectrum is often categorized into two sub-bands, namely 60 GHz band (or V-band) and the E-band ( $> 60$  GHz). To investigate the feasibility of mmWave backhaul connectivity, many research groups have been working on different mmWave bands. In EU FP7 project, mmWave self-backhauling was promoted for enabling broadband radio access networks [52]. In [53]- [57], intensive studies on verifying and testing the usage of 60 GHz by field measurements for both wireless mobile access and wireless backhaul/fronthaul, were conducted. In [58], mmWave was presented as the solution for boosting data rates to 10 Gbps with low delays in ultra-dense networks. Additionally, mmWave self-backhauling with interference-aware routing were proposed to avoid costly fronthaul connections. A study in [59] advocated a two-tier small cell backhaul architecture employing aggregation nodes with sub-6 GHz PtmP and PtP E-band links. This architecture is able to provide a flexible and scalable heterogeneous solution.

Another direction in 5G backhaul research is the in-band backhauling, in which the radio access is reused for backhaul links, thus optimizing resource utilization. In [60], a solution framework for supporting an in-band PtmP mmWave backhaul



was provided, together with trade-off analysis of gains and incurred reduction in radio access capacity. In addition, [61] studied the joint in-band backhaul scheduling and interference mitigation in 5G HetNet by solving the optimization problem with user throughput gains. In the context of heterogeneous networks, mmWave deployment for radio access and backhaul networks was investigated in [62]. Their results show that an aggregate cell throughput of nearly 13 Gbps is possible with 10 small cells per macro sector. mmWave was also adopted for radio access and backhaul/fronthaul, empowered with control/user plane splits, cognitive radio, and C-RAN in the MiWEBA project [63]. Besides, challenges of incorporating massive MIMO and mmWave technologies in 5G networks were analyzed in [64].

In brief, mmWave connectivity is a cost-effective solution for 5G backhaul, which is able to meet the capacity demand. However, it suffers from vulnerability to shadowing and mmWave transmission is sensitive to weather conditions.

### 3.2.3.2. FSO Backhauling Technologies

Recently, FSO has attracted much attention as a promising technology for 5G backhaul networks [65]. FSO refers to the transmission of modulated optical beam over the atmosphere to a photo-detector receiver. Given wavelength in the micrometer range, FSO is license-free and immune to electromagnetic interference generated by the radio frequency (RF) links. This important characteristic makes a FSO link become 25 fold more efficient than an RF link in terms of capacity. Moreover, FSO is also cheaper and easier to deploy, while providing comparable data rate, compared to optical fiber (OF) links. FSO links are sensitive to weather conditions, e.g., fog, snow, and rain [66]. As a result, the reliability under different environmental conditions becomes an important factor to address in the design of FSO-based backhaul networks. To cope with such varying reliability, the hybrid RF/FSO backhaul becomes an attractive, cost-effective and reliable solution as they are affected differently by weather conditions. For example, in harsh weather conditions that significantly affect the FSO link, the data is sent solely on the RF link [67]. Moreover, hybrid

RF/FSO system, as a wireless solution, can also be quickly deployed over several kilometers [68] and easily combined with OF links [69]. Therefore, hybrid RF/FSO or FSO only could be possible options for 5G backhaul networks [70].

Most of the current work in FSO [71], [72] focused on analyzing the adverse effects of channel factors affecting FSO performance, e.g., weather conditions, scintillation, etc., along with solutions for performance improvement, e.g., using multiple transmitters and multiple apertures. Thus, the research on the combination of RF and FSO technologies is still at the beginning. In [73], to satisfy a specified Quality of Service (QoS), an integer program to adaptively adjust both the transmission power and the optical beam-width of the hybrid RF/FSO was proposed. Another efficient and scalable algorithm to optimize a given physical layer objective for 2 and 3 optical transceivers per node with a minimum number of links was designed in [74]. On the other hand, results from studies in [75] and [76] showed that an RF network can be upgraded by optimally deploying a number of FSO transceivers to achieve a given throughput. For hybrid RF/FSO networks, a novel routing algorithm was designed so that traffic is backed up to the FSO route when the RF link is not able to carry it [77]. A linear integer programming model to determine routing in hybrid RF/FSO network was introduced in [67], in which the FSO link availability is varying with the weather conditions. To further improve the throughput in hybrid RF/FSO networks, a routing solution was proposed in [78]. In [79], a hybrid RF/FSO system was considered, in which the RF and FSO links operate at different data rates.

Regarding the problem of backhaul network design using hybrid RF/FSO technology, several mixed integer programming models were proposed. More specifically, an algebraic connectivity-based formulation for the design of the backbone of wireless mesh networks with FSO links was presented in [80]. To maximize the network throughput, FSO links can be installed as many as possible, under the constraint that the number of FSO links in a node is bounded [81]. In [82], a mixed integer programming model was introduced to find the optimal placement of FSO links to upgrade an existing RF backhaul network. Similarly in [76], an existing RF backhaul

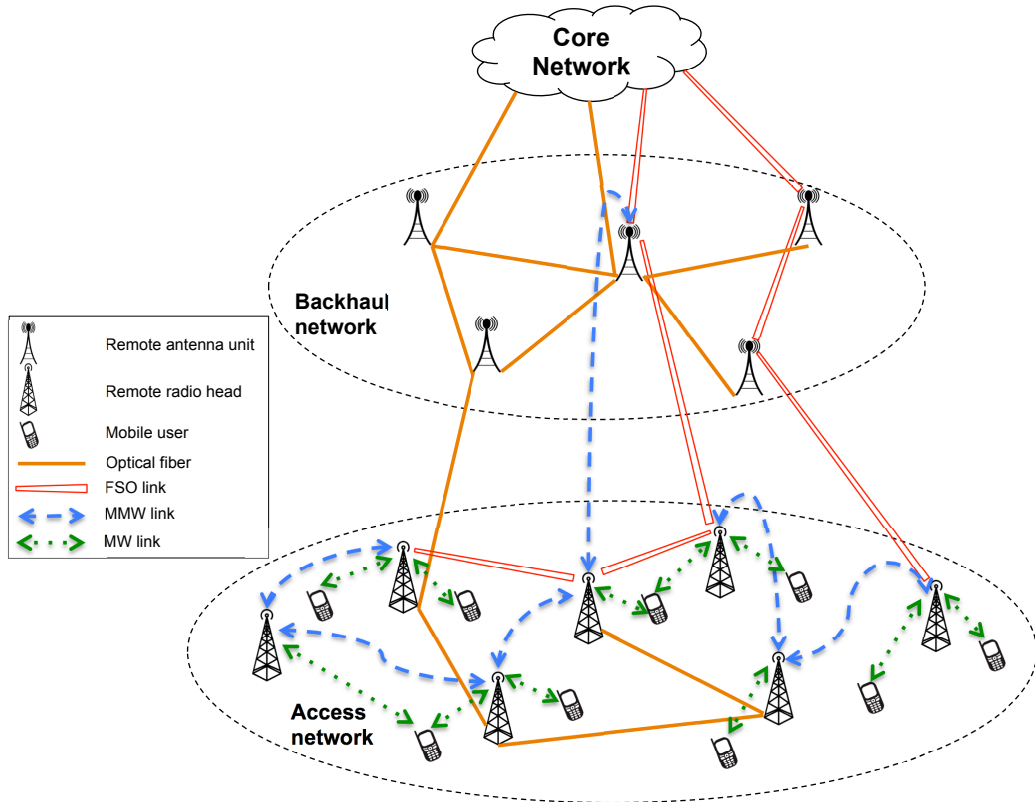


**Figure 3.6:** Our proposed architecture for 5G cellular networks [90].

network can be improved with the deployment of a minimum number of FSO links so that a target network throughput can be guaranteed when RF links are not available due to interference.

The authors in [83] suggests upgrading a pre-deployed OF backhaul network using hybrid RF/FSO links, and, hence, is related to the concept developed in [84], [85], and [86]. Particularly, the upgrade of a pre-deployed OF backhaul network using FSO links and mirrors for nodes was considered in [84]. In [86], the same group of authors analyzed the impact of the parameter  $K$  on the design. For two link-disjoint paths networks, they formulate the problem as a mixed integer programming and extend the study in [85] to  $K$  link-disjoint paths.

### 3.2.4. Architecture with Hybrid Technologies

The first challenge in 5G backhaul design is the requirement of cost-effective and scalable networks that connect a large number of cells to/from the mobile core net-

work, while ensuring sufficient capacity and quality of service. The second challenge is the resilience of backhaul networks to cope with different weather conditions is also critical to guarantee a better user experience. Finally, it is the energy efficiency is also an important issue in the large scale backhaul networks. To meet these challenges, hybrid backhaul networks that utilize both wireless and optical fiber links is therefore a cost-effective and energy-efficient solution to support the massive backhaul traffic [44].

There are many proposals dealing with the architectural designs for hybrid backhaul networks [84]- [86]. In [84]- [86], Li *et al.* presented cost-effective solutions, using FSO links and mirrors, to upgrade the cellular backhaul with pre-deployed optical fibers in 5G networks. However, the total distance of such a mirror path is subject to a limit, since mirrors provide no amplification. Additionally, in [87], possible implementations of radio-over-PON were discussed to integrate the wireless backhaul over optical access networks. Further steps in designing hybrid fiber-wireless (FiWi) backhaul networks have been made in [88]- [89]. Specifically, Liu *et al.* introduced an architecture concept using microwave-photonics, which involves the use of mmWave and radio-over-fiber (RoF) for 5G converged optical wireless access networks [88]. In [89], a seamlessly converged RoF and mmWave system at 90 GHz for high-speed wireless signal transmission in mobile backhaul network was experimentally demonstrated. As optical fiber is still the main transmission medium in all previous studies [84]- [89], the flexibility of backhaul network is confined to the fixed fiber-based architecture. The deployment of such fiber-based architecture is also cost-prohibitive and difficult to implement in densely populated metropolitan areas.

Our *proposed architecture* incorporating mmWave and FSO (together with pre-deployed optical fiber) is shown in Fig. 3.6 [90]. This architecture is expected to provide a cost-effective, scalable, and high capacity mobile backhaul connectivity for a future cloud RAN (C-RAN) in various deployment conditions. C-RAN is a centralized, cloud computing based cellular network architecture proposed to support current and future wireless communication standards. The utilization of mmWave

and FSO links are advocated in such areas where optical fiber deployment is infeasible and uneconomical. Typically, mmWave and FSO systems are not affected in the same way by atmospheric and weather effects, they therefore can be interchangeable based on the deployment conditions.

## **3.3. Scope of the Study**

### **3.3.1. Problem Statements**

Cellular backhaul networks provide connectivities between base stations and the core network. It is widely accepted that, compared to the 4G network, the 5G network is expected to achieve 1000 times the system capacity, 10 times the spectral efficiency, energy efficiency and data rate and 25 times the average cell throughput [38]. An important requirement in 5G backhaul networks is to be able to forward massive traffic to/from a large number of devices into the core network. Microwave and optical fiber have been considered as feasible solution for next-generation backhaul networks [91]. The limitations nevertheless are the facts that it is not always economical and/or possible to deploy optical fiber (especially for backhaul in high-density urban areas), and that microwave technology also has its own issues including limited data rates, licensed spectrum, interference, and weather conditions [92].

Two emerging technologies are being considered possible supplementary for above-mentioned limitations and challenges. The first one is free space optics (FSO) that has significantly evolved over the past decade [65]. An FSO link could be deployed by setting a pair of laser-photodetector transceivers in line of sight between two points to convey data through the free space transmission medium. The FSO beam uses a licensed-free wavelength in the range of micrometer, supports full-duplex, high-speed transmission, and is immune from electro-magnetic interference [68]. FSO and optical fiber are completely compatible since they operate at the same wavelength and data rates. The second one is radio frequency (RF) communication operating in millimeter-wave (mmWave) bands which is actually itself the key technology within

the evolution of 5G cellular networks [93]. Unlike microwave links, millimeter wave links cast very narrow beams that allow for deployment of multiple independent links in close proximity [25]. Moreover, mmWave also has the potential to offer bandwidth delivery comparable to that of optical fiber. Currently, the license-free 60 GHz band is under focus since it offers 10 times to 100 times more spectrum than is available for existing 4G cellular systems that operate at carrier frequencies below 6 GHz [94]. The mmWave backhaul integrating small cells in 5G cellular networks aims to extend the network capacity massively at reasonable cost and without loss of convenience to users [47].

Unlike previous studies that focused on realizing the parallel mmWave/FSO system, where data are simultaneously transmitted over both mmWave RF and FSO links [95], [96], our proposal considers the hybrid relaying system in the context that both mmWave and FSO technologies are integrated with optical fiber in a scalable and cost-effective architecture for the next-generation backhaul networks.

### 3.3.2. Hybrid Systems

A number of backhaul system variants in the proposed architecture are illustrated in Fig. 3.7. Fig. 3.7-a describes the conventional fiber-based system that utilizes optical fiber links from the baseband units (BBUs) in the core network to connect to radio access units (RAUs) in backhaul network and then remote radio heads (RRHs). The concept of converged system including fiber links from BBUs to RAUs and mmWave links from RAUs to RRHs is depicted in Fig. 3.7-b [89]. A dual-hop fiber-FSO system could also be deployed to connect the mobile core network to the small cells (Fig. 3.7-c) [97]. The use of FSO links for all connections in backhauling network is illustrated in Fig. 3.7-d [98]. Finally, a dual-hop mmWave/FSO system using fixed gain amplify-and-forward (AF) relaying to be considered in this chapter is described in Fig. 3.7-e. Similar system considering the conventional RF with FSO was also proposed in [99].

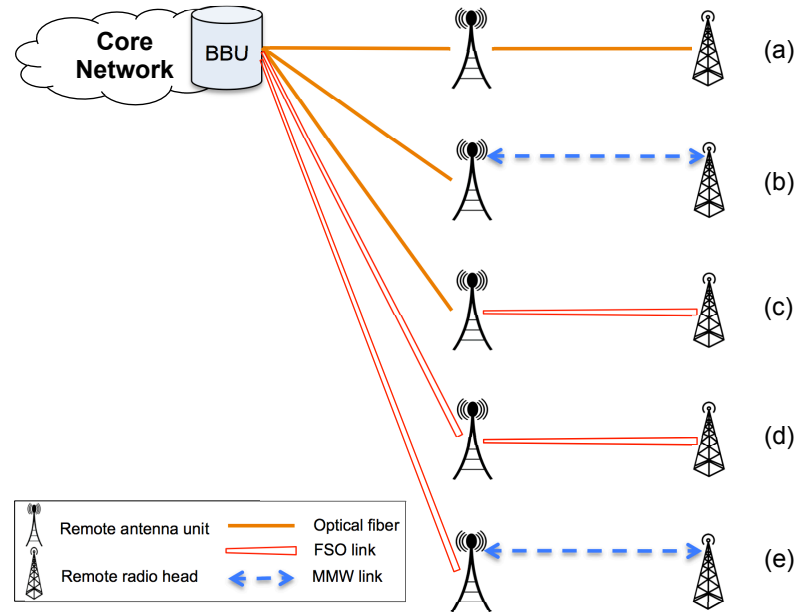


**Figure 3.7:** Possible backhaul connectivity subsystems. (a) Conventional fiber-based backhauling subsystem; (b) Fiber-mmWave RF backhauling subsystem; (c) Fiber-FSO backhauling subsystem; (d) FSO-FSO backhauling subsystem; (e) FSO-mmWave RF backhauling subsystem [90].

### 3.3.3. Contributions

Previous works on the mixture of mmWave RF and FSO only focused on the parallel system model, i.e., the signals are simultaneously transmitted over both links and then combined at the receiver on a symbol-by-symbol basis [96], [100]- [101]. Its major limitation is the cost for deploying and maintaining both mmWave RF and FSO systems at the same time for each transmission link. The parallel mmWave/FSO system can achieve 99.999% availability due to its robustness against foggy and rainy weather conditions. However, foggy and rainy conditions are very rare to happen at the same time. This fact reduce the application of the parallel system to areas where this combined weather condition is applicable. In contrast, in our hybrid architecture utilizing relaying mmWave/RF systems, signal is relayed through two/multiple hops that can offer better resilience and availability, as mmWave RF and FSO can be used interchangeably through different relaying paths. As there are numerous connection of FSO and mmWave links in the networks, different combinations of FSO and mmWave RF systems could be formed to timely adapt to the change of weather conditions.

Compared with the existing related studies on the mixture of mmWave RF and FSO, the contributions of our proposal are summarized as follows.

1. To the best of our knowledge, this is the first proposal to study the performance of mixed mmWave/FSO relaying systems in the context of 5G networks. The effects of different channel weather conditions and pointing errors are considered to give insightful results for the implementation of practical systems.
2. Different relaying configurations for various combinations of mixed FSO/FSO, mmWave/FSO, mmWave/mmWave networks will be investigated. In addition, improvement techniques suitable for these relaying system combinations of are proposed, including two-way communication, relaying techniques, and diversity reception with generalized selection combining (GSC). To evaluate the accuracy of the derived analytical model and performance results, comprehensive experiments based on real environment statistic and computer-based Monte-Carlo simulations are implemented.

### **3.4. Conclusions**

In this chapter, we presented a review of the state-of-the-art of 5G wireless backhaul technologies and focused on the applications of enabling wireless technologies including mmWave and FSO for 5G backhaul networks. We proposed a hybrid architecture for the 5G-backhaul networks utilizing both wired (OF) and wireless (mmWave/FSO) connections to provide a cost-effective, scalable, reliable, and high-capacity connectivity in the future heterogeneous network (HetNet) with the ability to dynamically adjust and adapt to the changes in the network in a flexible, efficient, and timely manner.



# Chapter 4

## Relaying mmWave RF/FSO

### Systems

#### 4.1. Introduction

With the rapid proliferation of Internet mobile devices, the fifth generation (5G) of cellular networks is predicted to achieve 1000 times the system capacity, 10 times the spectral/energy efficiency, 10-100 times the data rate, and 25 times the average cell throughput, compared to the fourth generation (4G) networks [23]. To increase the network capacity, the inevitable trend is the deployment of ultra-dense networks with a large number of smaller cells. The massive data traffic from small cells shall be connected to the core network through the *backhaul network* with extreme requirements in terms of capacity, latency, reliability, energy efficiency, and cost effectiveness.

Currently, the most viable solution for such a backhaul network is to use optical fiber (OF) together with millimeter-wave radio frequency (mmWave RF) links [47,48]. In ultra-dense cellular networks however, the mmWave RF interference issue may arise, and the mmWave RF capacity, in some cases, may not be enough for the 5G requirements. In addition, installation of OF is sometimes limited due to the high cost, especially in ultra-dense environment, or even impossible because of the

restriction on cable installation. Free-space optics (FSO) technology, which is able to offer a vast bandwidth (comparable to that of OF) over flexible and cost-effective free-space links, therefore can be an effective alternative to both OF and mmWave RF [102, 103].

Our argument is that none of the above-mentioned technologies can be a stand-alone solution for the next-generation backhaul network. OF is still the suitable choice for upper-tier connections, whereas mmWave RF and FSO are more preferable for the high-density small cells. A hybrid architecture, as depicted in Fig. 4.1, utilizing both wired (OF) and wireless (mmWave/FSO) connections is therefore proposed for cost-effective, highly scalable, and high-capacity backhauling in 5G cellular networks. More specifically, Fig. 4.1(a) shows the standard deployment of mmWave RF and OF to connect a macro cell with multiple micro cells to the backhaul network [48]. Alternatively, in Fig. 4.1(b), OF is replaced by FSO link when, for example, it is not possible to deploy OF. In addition, FSO can also be used for the links to micro cells with high capacity demands and/or for relaxing RF interference issue in ultra-dense cases. In this hybrid architecture, different types of sub-system, including OF/FSO, OF/RF, FSO/FSO, RF/RF and FSO/RF, have been studied in the literature and their performance analysis has been reported ([90]- [105] and references therein).

Our study focuses on the mixed RF/FSO sub-system in the hybrid architecture. As a matter of fact, there have been many studies on the performance of mixed RF/FSO systems, including very recent papers of [106]– [109] and references therein. In particular, Zedini *et al.* considered heterodyne/direct detection mixed RF/FSO systems over Nakagami- $m$  and Gamma-Gamma channels, respectively [106, 109]. The mixed RF/FSO systems, in which generalized  $M$ -distributed channel was assumed for FSO, was investigated in [107, 108]; and in both studies, the classical Rayleigh channel was assumed for RF links. It is nevertheless evident that the Rician fading channel is more suitable model when evaluating mmWave propagation due to the presence of the line-of-sight (LOS) component [110], and that it could be reduced to the Rayleigh fading model and mapped by the Nakagami- $m$  distribution [111]. In this paper, we

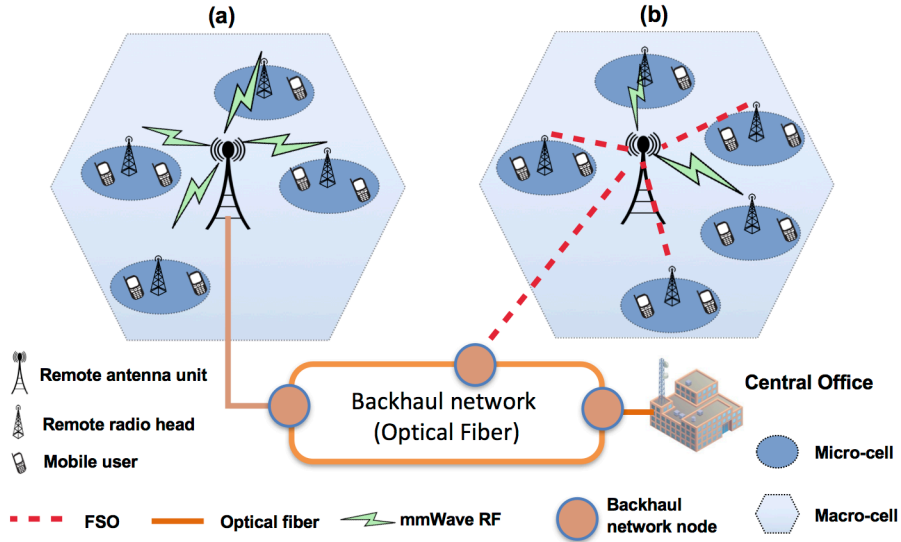


**Figure 4.1:** Hybrid architecture for backhaul networks: (a) Standard backhauling connection utilizing OF and mmWave RF [48]; (b) Proposed connection utilizing FSO and mmWave RF.

therefore employ the Rician and Málaga fading channel models for RF and FSO links, respectively, in the performance analysis of mixed mmWave RF/FSO systems using subcarrier intensity modulation (SIM) scheme with direct detection. Similar to Rician model, the Málaga ( $\mathcal{M}$ ) can also be considered as the generalized fading model for FSO which provides an excellent fit to the experimental data and represents most of the existing atmospheric turbulence channel models, including log-normal, Gamma-Gamma, K and Exponential models, as its special cases. In addition, to determine the reliability of FSO links in high density urban areas, the impact of pointing errors is also included in the analysis.

Our contributions in the paper are twofold. First, we newly derive closed-form expressions for the probability density function (PDF), the cumulative distribution function (CDF), and the moment generating function (MGF) in terms of Meijer's G functions. Capitalizing on these novel accurate results, closed-form expressions for various performance metrics of the proposed system including the outage probability, the average bit error rate (ABER), and the average capacity are derived. In addition, the asymptotic results under high signal-to-noise ratios (SNR) are provided for the outage probability, the MGF, and the ABER in terms of simple elementary functions

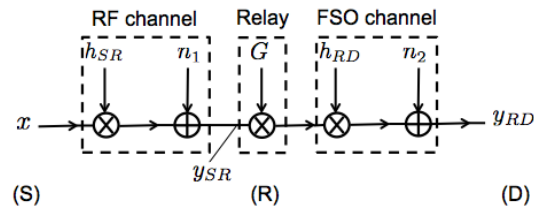


**Figure 4.2:** Mixed mmWave RF/FSO with AF relay system model.

by utilizing the asymptotic expansion of the Meijer's G function. Second, various performance metrics of the proposed system are thoroughly discussed under different channel conditions. We find that the combined effect of atmospheric turbulence and pointing errors significantly degrades the system performance and the quality of the mmWave RF link is of great importance in the overall system.

## 4.2. System Model

In the considered system model, as shown in Fig. 4.2, the source node (S) communicates with the destination node (D) via an intermediate relay node (R). The S-R and R-D hops use mmWave RF and FSO links, respectively; and in the context of mobile backhaul network, (S), (R) and (D), respectively, could be a remote antenna unit (RAU), a baseband unit (BBU) and a remote radio head (RRH). We consider the fixed-gain AF relaying scheme, i.e., the relay simply amplifies the signal by multiplying it with a fixed gain, regardless of the magnitude of the input signal. The mmWave RF link is assumed to follow a Rician distribution. On the other hand, the FSO link is modeled as the  $\mathcal{M}$  fading channel. As a crucial criteria to determine the reliability of FSO links, the effect of pointing errors due to the misalignment between the transmitter and the receiver in the FSO link is also taken into account by using the model developed in [112].

The signal received at (R), which was transmitted from (S) through the mmWave RF link, is given as

$$y_{SR} = h_{SR}x + n_{SR}, \quad (4.1)$$

where  $x$  is the transmitted signal from (S),  $n_{SR}$  is the additive white Gaussian noise (AWGN) with zero-mean and variance  $\sigma_{SR}^2$ , and  $h_{SR}$  represents the channel coefficient of the mmWave RF link. The SIM scheme is employed at (R) where a standard RF modulator and demodulator are used for transmitting and recovering the source transmitted data [113]. After filtering via a bandpass filter, a direct current (DC) bias is added to the RF signal to ensure the non-negativity of the optical signal. This bias signal is then amplified with a fixed-gain  $G$  and led to a continuous wave laser driver. Thus, the output of the optical at (R), denoted as  $y_R$ , can be written as  $y_R = G(1 + \eta y_{SR})$ , where  $\eta$  is the electrical-to-optical conversion coefficient. The optical signal is eventually forwarded to the destination (D) through the atmosphere of the FSO channel. After removing the DC component, the complex signal received at (D) can be written as

$$\begin{aligned} y_{RD} &= h_{RD}G\eta(h_{SR}x + n_{SR}) + n_{RD} \\ &= h_{RD}G\eta h_{SR}x + h_{RD}G\eta n_{SR} + n_{RD}, \end{aligned} \quad (4.2)$$

where  $h_{RD}$  is the channel coefficient of the FSO link and  $n_{RD}$  denotes the zero-mean AWGN noise with variance  $\sigma_{RD}^2$ . From (4.2), the instantaneous received SNR at (D), denoted as  $\gamma_{e2e}$ , can be written as

$$\gamma_{e2e} = \frac{h_{RD}^2 G^2 \eta^2 h_{SR}^2}{h_{RD}^2 G^2 \eta^2 \sigma_{SR}^2 + \sigma_{RD}^2} = \frac{\gamma_1 \gamma_2}{\gamma_2 + C}, \quad (4.3)$$

where  $\gamma_1 = \frac{h_{SR}^2}{\sigma_{SR}^2}$ ,  $\gamma_2 = \frac{\eta^2 h_{RD}^2}{\sigma_{RD}^2}$  are the instantaneous SNRs of the mmWave RF and FSO links, and  $C = \frac{1}{G^2 \sigma_{SR}^2}$ . Assuming that the fixed-gain  $G$  can completely compensate the noise resulted from the RF link, we can set  $C = 1$  [114].

### 4.3. mmWave RF Channel Model

The channel coefficient of the RF link can be described as  $h_{SR} = a_1 h_1$ , where  $a_1$  and  $h_1$  denote the average power gain and fading gain of the RF link, respectively;

and the average power gain of the RF link can be given by

$$a_1(dB) = G_T + G_R - 20\log_{10}\left(\frac{4\pi L_1}{\lambda_1}\right) - \alpha_{oxy}L_1 - \alpha_{rain}L_1, \quad (4.4)$$

where  $G_T$  and  $G_R$  are the transmit and receive antenna gains, respectively;  $\lambda_1$  is the wavelength of the RF system,  $L_1$  is the transmission distance of the RF link,  $\alpha_{oxy}$  and  $\alpha_{rain}$  are the attenuations caused by oxygen absorption and rain, respectively [115]. The fading gain,  $h_1$ , is modeled by Rician distribution with the PDF given by [111, pp. 21]. According to [111, pp. 420], the PDF of the instantaneous SNR received at (R) of the RF link, denoted as  $\gamma_1$ , is given by

$$f_{\gamma_1}(\gamma_1) = \frac{K+1}{\bar{\gamma}_1} \exp\left(- (K+1)\frac{\gamma_1}{\bar{\gamma}_1} - K\right) I_0\left(2\sqrt{K(K+1)}\frac{\gamma_1}{\bar{\gamma}_1}\right), \quad (4.5)$$

where  $K$  is the Rician factor ( $K \geq 0$ )<sup>1</sup> that depends on various link parameters, such as link distance or antenna height;  $\bar{\gamma}_1$  is the average SNR of the mmWave RF link,  $I_0$  is the 0-th order modified Bessel function of the first kind [116]. Furthermore, its CDF can be expressed as

$$F_{\gamma_1}(\gamma_1) = 1 - Q_1\left(\sqrt{2K}, \sqrt{\frac{2(K+1)}{\bar{\gamma}_1}\gamma_1}\right), \quad (4.6)$$

where  $Q_1(\cdot, \cdot)$  is the Marcum  $Q_1$ -function [111].

To facilitate our calculation, alternative expressions in terms of the infinite series representations of the PDF and the CDF for the Rician fading model adopted from [105], [117] are used<sup>2</sup>. By applying [105, (8) and (10)], (4.5) and (4.6) can be

<sup>1</sup>The Rician  $K$  factor reflects the relative strength of the direct LOS path component of the fading coefficient. When  $K = 0$  this model reduces to Rayleigh fading (i.e., there is no LOS path), and as  $K \rightarrow \infty$  the fading becomes deterministic giving rise to an additive white Gaussian noise (AWGN) channel [111].

<sup>2</sup>It is noted that the approaches to derive the infinite series representation of the CDF for the Rician fading model in [105] and [117] are similar.

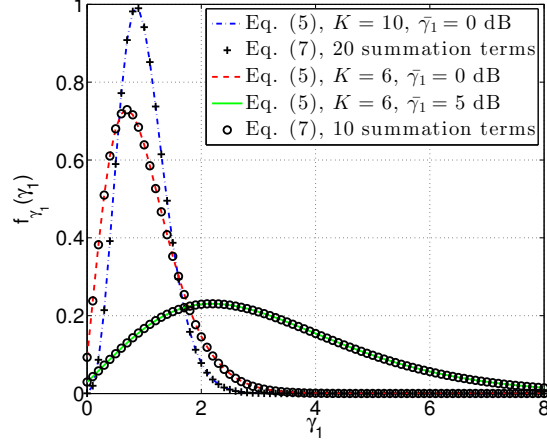


**Figure 4.3:** PDF plots for the exact expression in (4.5) and the approximation in (4.7).

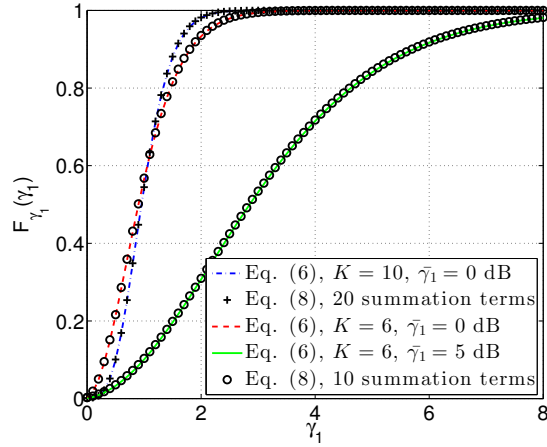


**Figure 4.4:** CDF plots for the exact expression in (4.6) and the approximation in (4.8).

respectively rewritten as

$$f_{\gamma_1}(\gamma_1) = \Phi \exp(-K) \exp(-\Phi\gamma_1) \sum_{n=0}^{\infty} \frac{(K\Phi)^n}{(n!)^2} (\gamma_1)^n, \quad (4.7)$$

$$F_{\gamma_1}(\gamma_1) = 1 - \exp(-K) \exp(-\Phi\gamma_1) \sum_{l=0}^{\infty} \sum_{n=0}^l \frac{K^l \Phi^n}{l!n!} (\gamma_1)^n, \quad (4.8)$$

where  $\Phi = \frac{K+1}{\bar{\gamma}_1}$ . In Fig. (4.3) and Fig. (4.4), we compare the PDFs and the CDFs of the Rician distribution for the exact expressions in (4.5), (4.6) and the approximations in (4.7), (4.8). As a result, we have the following observations.

*Observation 1:* The expressions of the PDF and CDF in (4.7), (4.8) contain the infinite summation which results from the use of the infinite series representations for

the Bessel  $I_0(\cdot)$  and the Marcum  $Q_1$  functions. However, for a given value of  $K$  and  $\bar{\gamma}_1$ , the infinite summation is convergent with a finite truncation. For example, as can be seen in Fig. (4.3) and Fig. (4.4), the expressions in (4.7) and (4.8) are convergent with 10 to 20 summation terms when  $K = 6$  dB and  $K = 10$  dB, respectively.

*Observation 2:* The effect of the channel parameter  $K$  on the SNR  $\gamma_1$  can be also seen from Fig. (4.3). The decrease of  $K$  spreads the distribution as it is the shape parameter and controls the steepness of the tail of the PDF. On the other hand, the height of the distribution decreases with an increase in the value of the parameter  $\bar{\gamma}_1$  since it is the scale parameter and determines the scale or the height of the distribution. As a result, any change in the channel parameters affects the tail probabilities, which are of great importance as the tail of the distribution defines the error performance.

## 4.4. FSO Channel Model

The channel coefficient of the FSO link can be described as  $h_{RD} = a_2 h_2 h_p$ , where  $a_2$ ,  $h_2$ , and  $h_p$  denote the channel loss, atmospheric turbulence-induced fading coefficient, and pointing error coefficient of the FSO link<sup>3</sup>, respectively. The channel loss  $a_2$  is caused by both the *geometric spreading* of the optical beam and the *atmospheric attenuation*.

### 4.4.1. Channel Loss

The value of loss due to the geometric spreading can be obtained as a function of the area of the receiver aperture  $A$  and the angle of divergence  $\theta$ . In addition, the path loss of laser power through the atmosphere is described by the exponential Beers-Lambert's Law. Hence,  $a_2$  can be provided by  $a_2 = \frac{A}{\pi(\frac{\theta}{2}L_2)^2} \exp(-\alpha_{att}L_2)$ , where  $A = \pi(a/2)^2$  with  $a$  is the diameter of the receiver aperture,  $\alpha_{att}$  denotes the attenuation coefficient in  $\text{km}^{-1}$ , and  $L_2$  is the transmission distance of the FSO

<sup>3</sup>It is assumed that the fading coefficient is normalized so that the mean intensity of the propagating wave is conserved, i.e.,  $\mathbb{E}[|h_2|^2] = 1$ , with  $\mathbb{E}[\cdot]$  is the statistical expectation.



link [118].

#### 4.4.2. $\mathcal{M}$ Atmospheric Turbulence Model

The  $\mathcal{M}$ -distribution statistically models an FSO channel taking into account three components: (1) a LOS component  $U_L$ , (2) a component  $U_S^C$  which is coupled to the  $U_L$  and quasi-forward scattered by the eddies on the propagation axis, and (3)  $U_S^G$  component which is due to energy that is scattered to the receiver by off-axis eddies. The PDF of  $h_2 \sim \mathcal{M}(\alpha, \beta, \rho, \tau, \Omega)$  can be given as [119, 120]

$$f_{h_2}(h_2) = \chi \sum_{k=1}^{\beta} a(k) h_2^{\frac{\alpha+k}{2}-1} K_{\psi} \left( 2\sqrt{\frac{\alpha\beta h_2}{\tau\beta + \Omega'}} \right), \quad (4.9)$$

where  $K_{\psi}(\cdot)$  is the modified Bessel function of the second kind and order  $\psi$ , with  $\psi = \alpha - k$ . Corresponding to channel  $h_2$ , the positive parameter  $\alpha$  represents the effective number of large scale cells of the scattering process,  $\beta$  is a natural number that represents amount of turbulence-induced fading<sup>4</sup>. Other parameters in (5.7) are expressed as follows.

$$\chi = \frac{2\alpha^{\frac{\alpha}{2}}}{\tau^{1+\frac{\alpha}{2}}\Gamma(\alpha)} \left( \frac{\tau\beta}{\tau\beta + \Omega'} \right)^{\beta+\frac{\alpha}{2}}, \quad \tau = 2b_0(1 - \rho), \quad (4.10)$$

$$a(k) = \binom{\beta-1}{k-1} \frac{(\tau\beta + \Omega')^{1-\frac{k}{2}}}{(k-1)!} \left( \frac{\Omega'}{\tau} \right)^{(k-1)} \left( \frac{\alpha}{\beta} \right)^{\frac{k}{2}}, \quad (4.11)$$

$$\Omega' = \Omega + 2\rho b_0 + 2\sqrt{2b_0\rho\Omega}\cos(\phi_1 - \phi_2). \quad (4.12)$$

Here,  $2b_0$  is the average power of total scattered component (i.e.,  $(U_S^G + U_S^C)$ ).  $\rho$  ( $0 \leq \rho \leq 1$ ) represents the amount of scattering power coupled to the LOS component, and thus the turbulence intensity reduces as the parameter  $\rho$  increases.  $\Omega$  is the average power of the LOS component  $U_L$ ,  $\phi_1$  and  $\phi_2$  are the deterministic phases of the LOS component  $U_L$  and the coupled-to-LOS component  $U_S^C$ , respectively.  $\Gamma(\cdot)$

---

<sup>4</sup>The notation  $\beta$  is limited to a natural number so that (5.7) will have a finite summation. It is noteworthy that there is a generalized expression of (5.7) given in [119, (22)] for  $\beta$  being a real number. However, this case is less interesting due to the high degree of freedom of the proposed distribution and the infinite summation.

denotes Gamma function defined as  $\Gamma(w) \triangleq \int_0^\infty t^{w-1} e^{-t} dt$ , and  $\binom{\cdot}{\cdot}$  denotes the binomial coefficient.

### 4.4.3. Pointing Errors Models

The statistical characterization of the pointing error impairments with *zero boresight effects* is given in [112], where a Gaussian spatial intensity profile is assumed for the beam waist. Thus, the PDF of the pointing error coefficient  $h_p$  is given as

$$f_{h_p}(h_p) = \frac{\xi^2}{A_0^{\xi^2}} h_p^{\xi^2-1}, \quad 0 \leq h_p \leq A_0, \quad (4.13)$$

where  $A_0$  is a constant term defining the pointing loss given by  $A_0 = [\text{erf}(\varsigma)]^2$ , with  $\text{erf}(z) \triangleq \frac{2}{\sqrt{\pi}} \int_0^z e^{-t^2} dt$  is the error function,  $\varsigma = \sqrt{\pi}\varepsilon/(\sqrt{2}w_z)$  where  $\varepsilon$  is the radius of the detection aperture, and  $w_z$  is the beam waist.  $\xi$  is the ratio between the equivalent beam radius at the receiver and the pointing error displacement standard deviation (jitter) at the receiver (i.e., when  $\xi \rightarrow \infty$ , (5.12) corresponds to the *non-pointing errors* case).

### 4.4.4. Composite Atmospheric Channel Model

The joint distribution of  $h_{RD} = a_2 h_2 h_p$  can be derived as

$$\begin{aligned} f_{h_{RD}}(h_{RD}) &= \int_{h_{RD}/(a_2 A_0)}^\infty f_{h_2}(h_2) f_{h_{RD}|h_2}(h_{RD}|h_2) dh_{h_2} \\ &= \int_{h_{RD}/(a_2 A_0)}^\infty f_{h_2}(h_2) \frac{h_{RD}}{h_2 a_2} f_{h_p}\left(\frac{h_{RD}}{h_2 a_2}\right) dh_2. \end{aligned} \quad (4.14)$$

By applying simple random variable transformation on (5.7) and using (5.13), we obtain the PDF of  $h_{RD}$  as

$$f_{h_{RD}}(h_{RD}) = \frac{\xi^2 \chi}{2 h_{RD}} \sum_{k=1}^{\beta} a(k) \Theta^{-\frac{\alpha+k}{2}} G_{1,3}^{3,0} \left( \frac{\Theta h_{RD}}{a_2 A_0} \left| \begin{matrix} \xi^2 + 1 \\ \xi^2, \alpha, k \end{matrix} \right. \right), \quad (4.15)$$

where  $G_{p,q}^{m,n}(\cdot | \cdot)$  is the Meijer's G function [116, (9.301)]<sup>5</sup>, and  $\Theta = \frac{\alpha\beta}{\tau\beta + \Omega'}$ . Denoting  $B = \frac{\xi^2\Theta(\tau + \Omega')}{\xi^2 + 1}$  and following the result for the IM/DD detection technique case obtained in [121], the PDF of  $\gamma_2$  can be derived as

$$f_{\gamma_2}(\gamma_2) = \frac{\xi^2\chi}{4\gamma_2} \sum_{k=1}^{\beta} a(k) \Theta^{-\frac{\alpha+k}{2}} G_{1,3}^{3,0} \left( B \sqrt{\frac{\gamma_2}{\mu}} \middle| \begin{matrix} \xi^2 + 1 \\ \xi^2, \alpha, k \end{matrix} \right), \quad (4.16)$$

where  $\mu = \frac{\xi^2(\xi^2+1)^{-2}(\xi^2+2)(\tau+\Omega')}{\alpha^{-1}(\alpha+1)[2\xi(\xi+2\Omega')+\Omega'^2(1+1/\beta)]} \bar{\gamma}_2$  is the electrical SNR of (4.16), and  $\bar{\gamma}_2$  is the average electrical SNR of the FSO link.

## 4.5. Statistical Characteristics of The End-to-end SNR, $\gamma_{e2e}$

### 4.5.1. Cumulative Distribution Function

The CDF of the end-to-end instantaneous electrical SNR  $\gamma_{e2e}$  can be expressed as

$$\begin{aligned} F_{\gamma_{e2e}}(\gamma) &= \Pr \left( \frac{\gamma_1\gamma_2}{\gamma_2 + 1} < \gamma \right) \\ &= \int_0^{\infty} \Pr \left( \frac{\gamma_1\gamma_2}{\gamma_2 + 1} < \gamma \mid \gamma_2 \right) f_{\gamma_2}(\gamma_2) d\gamma_2 = \int_0^{\infty} F_{\gamma_1} \left( \frac{1 + \gamma_2}{\gamma_2} \gamma \right) f_{\gamma_2}(\gamma_2) d\gamma_2. \end{aligned} \quad (4.17)$$

With the help of (4.8) and the binomial expansion in [116, (1.111)], (7.3) can

---

<sup>5</sup>The Meijer's G function provides a simple and tractable mathematical solution and can be easily computed using standard software packages such as Mathematica and Matlab.

be rewritten as

$$F_{\gamma_{e2e}}(\gamma) = 1 - \int_0^\infty \left[ \exp(-K) \exp\left(-\Phi \left(1 + \frac{1}{\gamma_2}\right) \gamma\right) \sum_{l=0}^\infty \sum_{n=0}^l \sum_{m=0}^n \frac{K^l (\Phi \gamma)^n}{l! n!} \binom{n}{m} \gamma_2^{-m} \right] \times f_{\gamma_2}(\gamma_2) d\gamma_2. \quad (4.18)$$

Now, some manipulations are made in (4.18) by using the Meijer's G function representation of an exponential function as [122, (11)] and the identity to invert the argument in the Meijer's G-function as [116, (9.312)], we then have

$$\exp\left(-\frac{\Phi \gamma}{\gamma_2}\right) = G_{0,1}^{1,0} \left[ \frac{\Phi \gamma}{\gamma_2} \middle| 0 \right] = G_{1,0}^{0,1} \left[ \frac{\gamma_2}{\Phi \gamma} \middle| 1 \right]. \quad (4.19)$$

Substituting (4.16) and (4.19) into (4.18), with the help of [122, (21)], (4.18) can be solved in a closed-form expression as

$$F_{\gamma_{e2e}}(\gamma) = 1 - \frac{\xi^2 \chi \exp(-K - \Phi \gamma)}{16\pi} \sum_{l=0}^\infty \sum_{n=0}^l \sum_{m=0}^n \sum_{k=1}^\beta \frac{K^l (\Phi \gamma)^{n-m}}{l! n!} \binom{n}{m} 2^{\alpha+k} a(k) \Theta^{-\frac{\alpha+k}{2}} \times G_{2,7}^{7,0} \left[ \frac{B^2 \Phi \gamma}{16\mu} \middle| \begin{matrix} \Xi_1 \\ \Xi_2 \end{matrix} \right]. \quad (4.20)$$

where  $\Xi_1 = \{\frac{\xi^2+1}{2}, \frac{\xi^2+2}{2}\}$  and  $\Xi_2 = \{\frac{\xi^2}{2}, \frac{\xi^2+1}{2}, \frac{\alpha}{2}, \frac{\alpha+1}{2}, \frac{k}{2}, \frac{k+1}{2}, m\}$ .

**Asymptotic Analysis:** Using [123, Eq. (07.34.06.0006.01)] when  $\bar{\gamma}_2 \rightarrow \infty$ , the asymptotic expression for the CDF in (4.20) *at high SNR* can be derived in terms of basic elementary functions as

$$F_{\gamma_{e2e}}(\gamma) \underset{\bar{\gamma}_2 \gg 1}{\approx} 1 - \frac{\xi^2 \chi \exp(-K - \Phi \gamma)}{16\pi} \sum_{l=0}^\infty \sum_{n=0}^l \sum_{m=0}^n \sum_{k=1}^\beta \frac{K^l (\Phi \gamma)^{n-m}}{l! n!} \binom{n}{m} 2^{\alpha+k} a(k) \Theta^{-\frac{\alpha+k}{2}} \times \sum_{i=1}^7 \left( \frac{B^2 \Phi \gamma}{16\bar{\gamma}_2} \right)^{\Xi_{2,i}} \frac{\prod_{j=1, j \neq i}^7 \Gamma(\Xi_{2,j} - \Xi_{2,i})}{\prod_{j=1}^2 \Gamma(\Xi_{1,j} - \Xi_{2,i})}, \quad (4.21)$$

where  $\Xi_{u,v}$  represents the  $v$ th-term of  $\Xi_u$ , with  $u \in \{1, 2\}$ ,  $v \in \{i, j\}$ .

### 4.5.2. Probability Density Function

The PDF of  $\gamma_{e2e}$  can be derived by differentiating (4.20) with respect to  $\gamma$ . By applying [123, (07.34.20.0001.01)] and [123, (07.34.16.0001.01)], we obtain the derivative of  $G_{2,7}^{7,0} \left[ \begin{matrix} B^2\Phi\gamma \\ 16\bar{\gamma}_2 \end{matrix} \middle| \begin{matrix} \Xi_1 \\ \Xi_2 \end{matrix} \right]$  with respect to  $\gamma$  as

$$\frac{\partial}{\partial \gamma} G_{2,7}^{7,0} \left[ \begin{matrix} B^2\Phi\gamma \\ 16\bar{\gamma}_2 \end{matrix} \middle| \begin{matrix} \Xi_1 \\ \Xi_2 \end{matrix} \right] = \frac{B^2\Phi}{16\bar{\gamma}_2} G_{3,8}^{7,1} \left[ \begin{matrix} B^2\Phi\gamma \\ 16\bar{\gamma}_2 \end{matrix} \middle| \begin{matrix} -1, \Xi_1 - 1 \\ \Xi_2 - 1, 0 \end{matrix} \right] = \frac{1}{\gamma} G_{3,8}^{7,1} \left[ \begin{matrix} B^2\Phi\gamma \\ 16\bar{\gamma}_2 \end{matrix} \middle| \begin{matrix} 0, \Xi_1 \\ \Xi_2, 1 \end{matrix} \right]. \quad (4.22)$$

After some mathematical manipulations, the PDF of  $\gamma_{e2e}$  can be expressed in a closed-form expression in terms of the Meijer's G functions as

$$\begin{aligned} f_{\gamma_{e2e}}(\gamma) = & \frac{\xi^2 \chi \exp(-K - \Phi\gamma)}{16\pi} \left\{ \sum_{l=0}^{\infty} \sum_{n=0}^l \sum_{m=0}^n \sum_{k=1}^{\beta} \frac{K^l \Phi (\Phi\gamma)^{n-m}}{l!n!} \binom{n}{m} 2^{\alpha+k} a(k) \Theta^{-\frac{\alpha+k}{2}} G_{2,7}^{7,0} \left[ \begin{matrix} B^2\Phi\gamma \\ 16\bar{\gamma}_2 \end{matrix} \middle| \begin{matrix} \Xi_1 \\ \Xi_2 \end{matrix} \right] \right. \\ & - \sum_{l=0}^{\infty} \sum_{n=0}^l \sum_{m=0}^n \sum_{k=1}^{\beta} \frac{K^l \Phi (n-m) (\Phi\gamma)^{n-m-1}}{l!n!} \binom{n}{m} 2^{\alpha+k} a(k) \Theta^{-\frac{\alpha+k}{2}} G_{2,7}^{7,0} \left[ \begin{matrix} B^2\Phi\gamma \\ 16\bar{\gamma}_2 \end{matrix} \middle| \begin{matrix} \Xi_1 \\ \Xi_2 \end{matrix} \right] \\ & \left. - \sum_{l=0}^{\infty} \sum_{n=0}^l \sum_{m=0}^n \sum_{k=1}^{\beta} \frac{K^l (\Phi\gamma)^{n-m}}{l!n!} \binom{n}{m} 2^{\alpha+k} a(k) \Theta^{-\frac{\alpha+k}{2}} \frac{1}{\gamma} G_{3,8}^{7,1} \left[ \begin{matrix} B^2\Phi\gamma \\ 16\bar{\gamma}_2 \end{matrix} \middle| \begin{matrix} 0, \Xi_1 \\ \Xi_2, 1 \end{matrix} \right] \right\}. \quad (4.23) \end{aligned}$$

From (4.23), the closed-form expression of  $f_{\gamma_{e2e}}$  can be further simplified as

$$\begin{aligned} f_{\gamma_{e2e}}(\gamma) = & \frac{\xi^2 \chi \exp(-K - \Phi\gamma)}{16\pi} \sum_{l=0}^{\infty} \sum_{n=0}^l \sum_{m=0}^n \sum_{k=1}^{\beta} \frac{K^l (\Phi\gamma)^{n-m}}{l!n!} \binom{n}{m} 2^{\alpha+k} a(k) \Theta^{-\frac{\alpha+k}{2}} \\ & \times \left\{ \left( \Phi - \frac{n-m}{\gamma} \right) G_{2,7}^{7,0} \left[ \begin{matrix} B^2\Phi\gamma \\ 16\bar{\gamma}_2 \end{matrix} \middle| \begin{matrix} \Xi_1 \\ \Xi_2 \end{matrix} \right] - \frac{1}{\gamma} G_{3,8}^{7,1} \left[ \begin{matrix} B^2\Phi\gamma \\ 16\bar{\gamma}_2 \end{matrix} \middle| \begin{matrix} 0, \Xi_1 \\ \Xi_2, 1 \end{matrix} \right] \right\}. \quad (4.24) \end{aligned}$$

### 4.5.3. Moment Generating Function

Using integration by parts, the MGF of  $\gamma_{e2e}$  can be expressed in terms of the CDF of  $\gamma_{e2e}$  as

$$M_{\gamma_{e2e}}(s) = s \int_0^{\infty} \exp(-\gamma s) F_{\gamma_{e2e}}(\gamma) d\gamma. \quad (4.25)$$

Substituting (4.20) into (5.19), with the help of [116, (3.310)], [122, (11)], and [122, (21)], the MGF can be written as

$$M_{\gamma_{e2e}}(s) = 1 - \frac{s\xi^2\chi \exp(-K)}{16\pi(s+\Phi)} \sum_{l=0}^{\infty} \sum_{n=0}^l \sum_{m=0}^n \sum_{k=1}^{\beta} \frac{K^l}{l!n!} \left(\frac{\Phi}{s+\Phi}\right)^{n-m} \binom{n}{m} 2^{\alpha+k} a(k) \Theta^{-\frac{\alpha+k}{2}} \\ \times G_{3,7}^{7,1} \left[ \frac{B^2\Phi}{16\bar{\gamma}_2(s+\Phi)} \middle| \begin{matrix} m-n, \frac{\xi^2+1}{2}, \frac{\xi^2+k}{2} \\ \frac{\xi^2}{2}, \frac{\xi^2+1}{2}, \frac{\alpha}{2}, \frac{\alpha+1}{2}, \frac{k}{2}, \frac{k+1}{2}, m \end{matrix} \right]. \quad (4.26)$$

**Asymptotic Analysis:** Using [123, Eq. (07.34.06.0006.01)] when  $\bar{\gamma}_2 \rightarrow \infty$ , the asymptotic expression for the MGF in (4.26) at high SNR can be derived in terms of basic elementary functions as

$$M_{\gamma_{e2e}}(s) \underset{\bar{\gamma}_2 \gg 1}{\approx} 1 - \frac{s\xi^2\chi \exp(-K)}{16\pi(s+\Phi)} \sum_{l=0}^{\infty} \sum_{n=0}^l \sum_{m=0}^n \sum_{k=1}^{\beta} \frac{K^l}{l!n!} \left(\frac{\Phi}{s+\Phi}\right)^{n-m} \binom{n}{m} 2^{\alpha+k} a(k) \Theta^{-\frac{\alpha+k}{2}} \\ \times \sum_{i=1}^7 \left(\frac{B^2\Phi}{16\bar{\gamma}_2(s+\Phi)}\right)^{\Xi_{2,i}} \frac{\prod_{j=1, j \neq i}^7 \Gamma(\Xi_{2,j} - \Xi_{2,i}) \Gamma(1 + \Xi_{2,i} - m + n)}{\prod_{j=2}^3 \Gamma(\Xi_{1,j} - \Xi_{2,i})}. \quad (4.27)$$

### 4.5.4. Remarks

It is noted that the single-fold infinite summation in (4.20), (4.24), and (4.26), is widely accepted in the literature as a closed-form solution due to the increased computational capabilities of the current standard software packages such as Matlab or Mathematica. In addition, since the summands in (4.20), (4.24), and (4.26) decay exponentially with the increase of  $l$  and  $n$  due to the factors  $\frac{1}{l!}$  and  $\frac{1}{n!}$ , only a finite number of terms will be sufficient to guarantee a high accuracy of the summation.

## 4.6. Performance Analysis

### 4.6.1. Outage Probability

The outage probability is an important performance metric for evaluating wireless systems over fading channels. At a given transmission rate  $R_b$ , the outage probability can be defined as  $P_{out} = \Pr(\mathbb{C}(\gamma) < R_b)$ , where  $\mathbb{C}(\gamma)$  is the instantaneous capacity of the channel, and  $\gamma$  is the instantaneous SNR. Since  $\mathbb{C}(\cdot)$  is a monotonically increasing function with respect to  $\gamma$ , the outage probability can be obtained as

$$P_{out} = \Pr(\gamma < \gamma_{th}), \quad (4.28)$$

where  $\gamma_{th} = \mathbb{C}^{-1}(R_b)$  is the predetermined threshold SNR required to support the data rate  $R_b$ . In AF relaying, as the relay node simply scales the received signal without any decoding, the outage probability of the system is also defined as the probability that the end-to-end instantaneous SNR  $\gamma_{e2e}$  falls below the threshold  $\gamma_{th}$ . Hence, based on (6.13), the end-to-end outage probability of the considered system can be expressed as

$$P_{out} = F_{\gamma_{e2e}}(\gamma_{th}). \quad (4.29)$$

Substituting (4.20) into (4.29), the closed-form expression for the outage probability of the considered system can be obtained. Furthermore, the asymptotic approximation of the outage probability can be obtained by substituting  $\gamma_{th}$  for  $\gamma$  in (4.21).

### 4.6.2. Average BER

In this subsection, the BER of the mixed mmWave RF/FSO system is derived for the SIM-based  $M$ -ary quadrature amplitude modulation ( $M$ -QAM), and  $M$ -ary phase shift keying ( $M$ -PSK) under the impact of pointing errors. It is well known that

the BER of  $M$ -PSK and  $M$ -QAM signal constellations over an AWGN channel can be expressed as a linear summation of the Gaussian  $Q$ -function defined as  $Q(x) \triangleq \frac{1}{\sqrt{2\pi}} \int_0^\infty e^{-t^2/2} dt$ . Therefore, in order to evaluate the error performance of  $M$ -ary modulation schemes over a fading channel, we need to evaluate integrals of the form

$$P(e, \vartheta) = \int_0^\infty Q\left(\sqrt{\vartheta_i \gamma}\right) f_{\gamma_{e2e}}(\gamma) d\gamma, \quad (4.30)$$

where  $\vartheta$  depends on the modulation type [124]. Using the result in [125], (4.30) can be expressed in terms of the CDF of the SNR as

$$P(e, \vartheta) = \frac{1}{\sqrt{2\pi}} \int_0^\infty F_{\gamma_{e2e}}\left(\frac{t^2}{\vartheta}\right) \exp\left(-\frac{t^2}{2}\right) dt. \quad (4.31)$$

Making the change of variable  $x = t^2$ , (4.31) can be expressed as

$$P(e, \vartheta) = \frac{1}{\sqrt{2\pi}} \int_0^\infty F_{\gamma_{e2e}}\left(\frac{x}{\vartheta}\right) \exp\left(-\frac{x}{2}\right) \frac{dx}{2\sqrt{x}}. \quad (4.32)$$

Using [116, (3.361.2)], [122, (11)], and [122, (21)], (4.32) can be expressed in a closed-form expression as

$$\begin{aligned} P(e, \vartheta) = & \frac{1}{2} - \frac{\xi^2 \chi \exp(-K)}{32\pi\sqrt{2\pi}} \sum_{l=0}^{\infty} \sum_{n=0}^l \sum_{m=0}^n \sum_{k=1}^{\beta} \binom{K^l}{l!n!} \left(\frac{\Phi}{\vartheta}\right)^{n-m} \left(\frac{\Phi}{\vartheta} + \frac{1}{2}\right)^{m-n-\frac{1}{2}} \\ & \times \binom{n}{m} 2^{\alpha+k} a(k) \Theta^{-\frac{\alpha+k}{2}} \\ & \times G_{3,7}^{7,1} \left[ \frac{B^2 \Phi}{8\bar{\gamma}_2(2\Phi + \vartheta)} \left| \begin{array}{c} m-n+\frac{1}{2}, \frac{\xi^2+1}{2}, \frac{\xi^2+2}{2} \\ \frac{\xi^2}{2}, \frac{\xi^2+1}{2}, \frac{\alpha}{2}, \frac{\alpha+1}{2}, \frac{k}{2}, \frac{k+1}{2}, m \end{array} \right. \right]. \end{aligned} \quad (4.33)$$

Using the unified approximation from [124], the average BER for  $M$ -PSK constellations with Gray coding operating over a fading channel is given by

$$P_{MPSK}(e) \cong \frac{2}{\max(\log_2 M, 2)} \sum_{i=1}^{\max(\frac{M}{4}, 1)} P(e, \vartheta_{i, MPSK}), \quad (4.34)$$

where  $\vartheta_{i, MPSK} = 2(\log_2 M) \sin^2\left((2i-1)\frac{\pi}{M}\right)$ . The corresponding average BER for



$M$ -QAM constellations with Gray coding is

$$P_{MQAM}(e) \cong \frac{4}{\log_2 M} \left(1 - \frac{1}{\sqrt{M}}\right) \sum_{i=1}^{\frac{\sqrt{M}}{2}} P(e, \vartheta_{i, MQAM}), \quad (4.35)$$

where  $\vartheta_{i, MQAM} = 3(2i - 1)^2 \frac{(\log_2 M)}{M-1}$ . Substituting (4.34) and (4.35) into (4.33), the closed-form expressions for the ABER of the considered system using  $M$ -PSK and  $M$ -QAM can be obtained, respectively.

**Asymptotic Analysis:** Using [123, Eq. (07.34.06.0006.01)] when  $\bar{\gamma}_2 \rightarrow \infty$ , the asymptotic expression for the ABER in (4.33) *at high SNR* can be derived in terms of basic elementary functions as

$$\begin{aligned} P(e, \vartheta) \underset{\bar{\gamma}_2 \gg 1}{\approx} & \frac{1}{2} - \frac{\xi^2 \chi \exp(-K)}{32\pi\sqrt{2\pi}} \sum_{l=0}^{\infty} \sum_{n=0}^l \sum_{m=0}^n \sum_{k=1}^{\beta} \binom{K^l}{l!n!} \left(\frac{\Phi}{\vartheta}\right)^{n-m} \left(\frac{\Phi}{\vartheta} + \frac{1}{2}\right)^{m-n-\frac{1}{2}} \\ & \times \binom{n}{m} 2^{\alpha+k} a(k) \Theta^{-\frac{\alpha+k}{2}} \\ & \times \sum_{i=1}^7 \left(\frac{B^2 \Phi}{8\bar{\gamma}_2(2\Phi + \vartheta)}\right)^{\Xi_{2,i}} \frac{\prod_{j=1, j \neq i}^7 \Gamma(\Xi_{2,j} - \Xi_{2,i}) \Gamma\left(\frac{1}{2} + \Xi_{2,i} - m + n\right)}{\prod_{j=2}^3 \Gamma(\Xi_{1,j} - \Xi_{2,i})}. \end{aligned} \quad (4.36)$$

### 4.6.3. Average Capacity Analysis

It is well-known that the atmospheric turbulence over FSO links is slow in fading. Since the coherence time of the channel is in the order of milliseconds (ms), turbulence induced fading remains constant over a large number of transmitted bits [126]. Without any delay constraints, if the codeword extends over at least several atmospheric turbulence time, which allows coding across both deep and shallow fade channel realizations, the fast fading regime can be assumed. The average capacity, in this context, is the expectation with respect to the gains of the instantaneous capacity [127]. In this subsection, we provide a lower-bound average capacity formula by

using the complementary CDF (CCDF)-based approach as

$$\bar{C} = \frac{1}{\ln 2} \int_0^\infty \frac{F_{\gamma e^{2e}}^c(\gamma)}{\left(1 + \frac{e}{2\pi}\gamma\right)} d\gamma, \quad (4.37)$$

where  $F_{\gamma e^{2e}}^c(\gamma) = 1 - F_{\gamma e^{2e}}(\gamma)$  is the CCDF of  $\gamma e^{2e}$  [106]. With the help of [128],  $\frac{1}{\left(1 + \frac{e}{2\pi}\gamma\right)}$  can be expressed in terms of the Meijer's G function as  $G_{1,1}^{1,1} \left[ \frac{e}{2\pi}\gamma \middle| \begin{matrix} 0 \\ 0 \end{matrix} \right]$ . Next, plugging (4.20) into (4.37), with the help of [129, (6)] and [130, (20)], the closed-form expression of the average capacity can be obtained in terms of the extended bivariate Meijer's G function (EGBMGF)<sup>6</sup> as

$$\bar{C} = \frac{\xi^2 \chi \exp(-K)}{16\pi\Phi \ln 2} \sum_{l=0}^{\infty} \sum_{n=0}^l \sum_{m=0}^n \sum_{k=1}^{\beta} \left( \frac{K^l}{l!n!} \right) \binom{n}{m} 2^{\alpha+k} a(k) \Theta^{-\frac{\alpha+k}{2}} S \left[ \begin{matrix} \left[ \begin{matrix} 1 & 0 \\ 0 & 0 \\ 1 & 1 \\ 0 & 0 \\ 0 & 7 \\ 2 & 0 \end{matrix} \right] & \left| \begin{matrix} \Psi; - \\ 0; 0 \\ \Xi_1; \Xi_2 \end{matrix} \right. & \left. \begin{matrix} \frac{e}{2\pi\Phi} \\ \frac{B^2}{16\gamma^2} \end{matrix} \right] \right], \quad (4.38)$$

where  $S[\cdot]$  is the EGBMGF,  $\Psi = (n - m + 1)$ ,  $\Xi_1$  and  $\Xi_2$  are defined in (4.20).

## 4.7. Numerical Results

For the FSO channel, we use the similar set of turbulence parameters for  $\mathcal{M}$  channels as in [119]– [121]. In particular,  $(\alpha = 2.296, \beta = 2)$ ,  $(\alpha = 4.2, \beta = 3)$ , and  $(\alpha = 8, \beta = 4)$  for strong, moderate and weak turbulence conditions. Other parameters for  $\mathcal{M}$  channels include  $\Omega = 1.3265, b_0 = 0.1079, \phi_1 - \phi_2 = \pi/2$ . It is noted that  $\rho = 1$  (then  $\tau = 0, \Omega' = 1$ ) corresponds to the special case of *Gamma-*

<sup>6</sup>It is noted that the EGBMGF cannot be directly computed by current versions of standard software packages such as Matlab and Mathematica. In general, it must be computed by its definition in terms of the double Mellin-Barnes type integrals [129, (1)]. With the help of [130] and [131], [132], the two-fold Mellin-Barnes integral can be accurately evaluated by Mathematica and Matlab, respectively. The use of EGBMGF as a closed-form solution has been widely accepted in the literature.

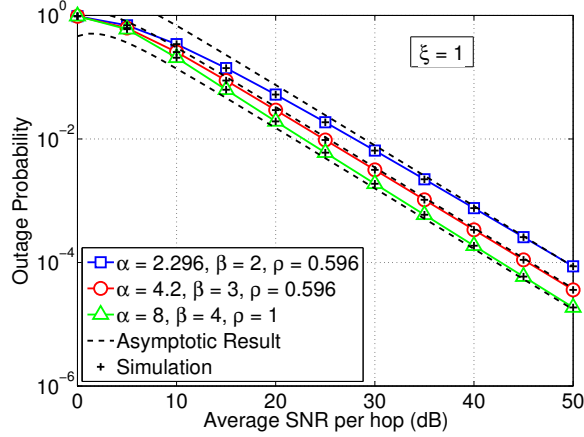


**Figure 4.5:** Outage probability versus the average SNR per hop ( $\bar{\gamma}_1 = \bar{\gamma}_2$ ) under different turbulence conditions,  $\gamma_{th} = 0$  dB,  $\xi = 1$  (i.e., strong pointing errors).

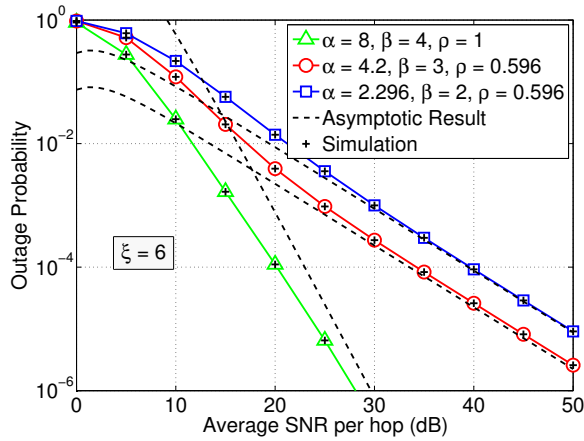


**Figure 4.6:** Outage probability versus the average SNR per hop ( $\bar{\gamma}_1 = \bar{\gamma}_2$ ) under different turbulence conditions,  $\gamma_{th} = 0$  dB,  $\xi = 6$  (i.e., weak pointing errors).

*Gamma distribution.* As for the RF channel, the Rician factor,  $K = 6$  dB, is used<sup>7</sup>. The effect of pointing errors is investigated in two cases when  $\xi = 1$  and  $\xi = 6$  [12].

The outage probability performance of the considered system versus the average SNR per hop (i.e.,  $\bar{\gamma}_1 = \bar{\gamma}_2$ ) under the combined effect of various atmospheric turbulence conditions and pointing errors is investigated in Fig. 4.5 with  $\xi = 1$  (i.e., strong pointing errors) and Fig. 4.6 with  $\xi = 6$  (i.e., weak pointing errors). It is first confirmed that analytical results are perfectly matched with M-C simulations. It is seen in Fig. 4.5 that severe pointing errors combined with the atmospheric turbulence

<sup>7</sup>Obtained from experimental results of 28 GHz directional small-scale fading measurements with vertical-to-horizontal antenna polarization configurations, the  $K$  factor is selected in the range of 3 to 7 dB [110].

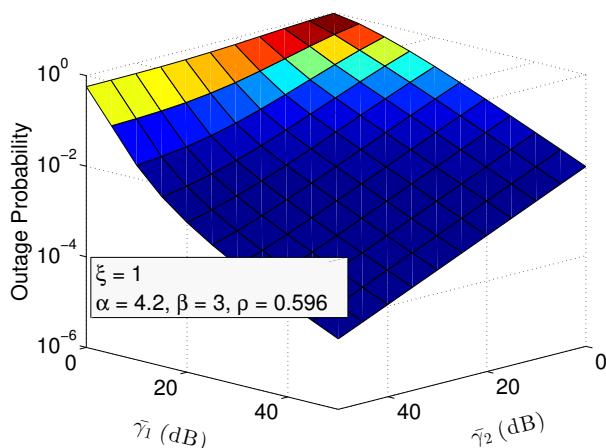


**Figure 4.7:** Outage probability versus the average SNRs of the RF ( $\bar{\gamma}_1$ ) and FSO links ( $\bar{\gamma}_2$ ) under the moderate turbulence condition,  $\gamma_{th} = 0$  dB,  $\xi = 1$  (i.e., strong pointing errors).

significantly deteriorates the outage performance of the system. Especially, under the impact of strong turbulence and pointing errors with  $\xi = 1$ , the outage can only reach to  $10^{-4}$  even when the system operating in the high SNR regime (e.g., 50 dB). On the other hand, in Fig. 4.6, as the effect of pointing errors becomes weaker, e.g.,  $\xi = 6$ , the outage probability can be lowered to  $10^{-5}$  when the turbulence is strong and the system is in the high SNR regime. Additionally, in both Fig. 4.5 and Fig. 4.6, the asymptotic results at high SNR are also provided along with the analytical ones. It can be observed that the asymptotic expression, which utilizes the Meijer's G function asymptotic expansion, converges to the exact result in the high SNR regime. This proves the tightness of the derived asymptotic approximation.

When the SNR of each hop is different ( $\bar{\gamma}_1 \neq \bar{\gamma}_2$ ), Fig. 4.7 and Fig. 4.8 illustrate the outage probability versus the average SNRs of the mmWave RF and FSO links under the impact of moderate atmospheric turbulence and pointing errors. It is observed in both figures that the performance of the considered system is better when the average SNR of the RF link ( $\bar{\gamma}_1$ ) is larger than that of the FSO link ( $\bar{\gamma}_2$ ). Fig. 4.7 and Fig. 4.8 also reveals that strong pointing errors significantly degrade the outage performance of the overall system.

In Fig. 4.9 and Fig. 4.10, assuming  $\bar{\gamma}_1 = \bar{\gamma}_2$ , the ABER performance of sys-

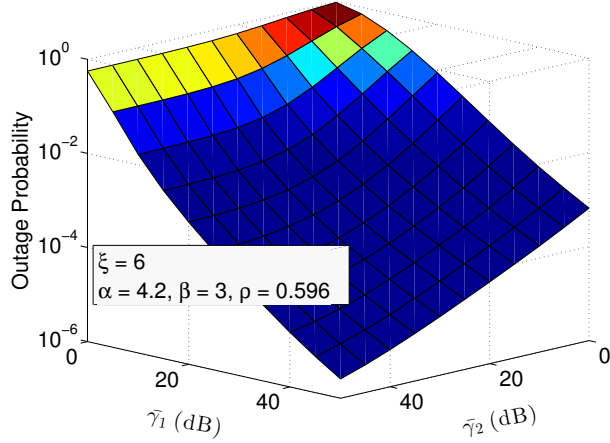


**Figure 4.8:** Outage probability versus the average SNRs of the RF ( $\bar{\gamma}_1$ ) and FSO links ( $\bar{\gamma}_2$ ) under the moderate turbulence condition,  $\gamma_{th} = 0$  dB,  $\xi = 6$  (i.e., weak pointing errors).

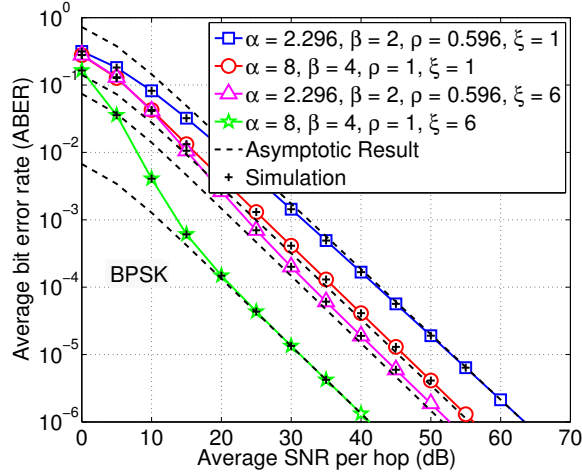


**Figure 4.9:** ABER versus the average SNRs per hop ( $\bar{\gamma}_1 = \bar{\gamma}_2$ ) under different turbulence conditions and pointing errors: systems employing BPSK.

tems using BPSK and QAM schemes for varying effects of atmospheric turbulence and pointing errors is illustrated. Also, it is seen that analytical results are perfectly matched with M-C simulations. There are two important observations that can be deduced from these figures. First, as expected, the impact of strong atmospheric turbulence results in a worse ABER performance. Specifically, compared to systems operating under the impact of weak turbulence, the performance loss of about 7 dB and 11 dB (in Fig. 4.9), and 6 dB and 10 dB (in Fig. 4.10) at the ABER of  $10^{-6}$  when  $\xi = 1$  and  $\xi = 6$ , respectively, can be seen. Second, as the effect of pointing

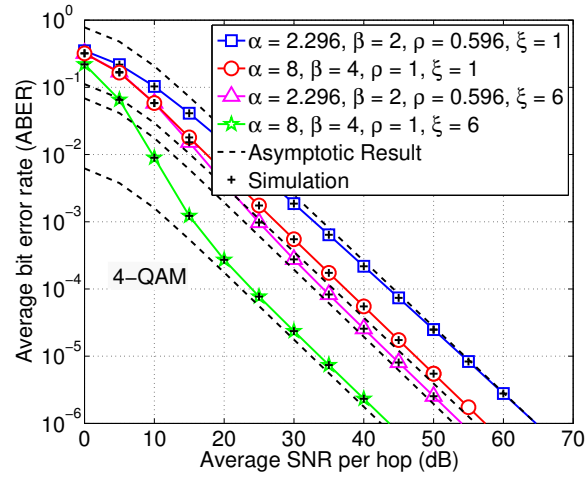


**Figure 4.10:** ABER versus the average SNRs per hop ( $\bar{\gamma}_1 = \bar{\gamma}_2$ ) under different turbulence conditions and pointing errors: systems employing 4-QAM.

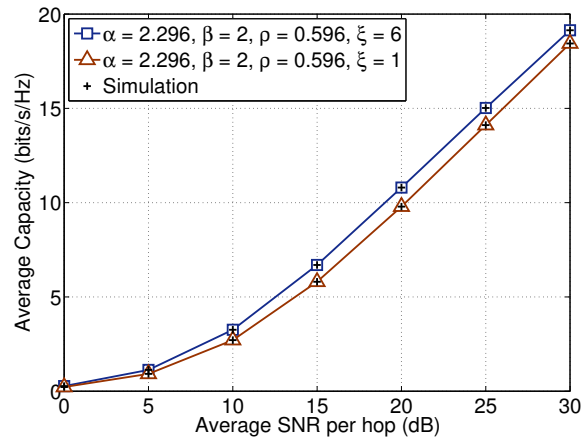


**Figure 4.11:** Average capacity versus the average SNRs per hop ( $\bar{\gamma}_1 = \bar{\gamma}_2$ ) under different turbulence conditions and pointing errors: strong turbulence.

errors decreases ( $\xi \rightarrow \infty$ ), the respective performance is considerably improved. For instance, when  $\xi$  increases from 1 to 6, the attained ABER performance gain is approximately 10 dB and 14 dB (in Fig. 4.9), and 9 dB and 13 dB (in Fig. 4.10) at the ABER of  $10^{-6}$  under strong and weak turbulence conditions, respectively. In addition, the asymptotic results further confirm the tightness of the derived asymptotic approximation in the high SNR regime.

Finally, Fig. (4.11) and Fig. (4.12) depict the average capacity of the considered system under the effect of various turbulence conditions and pointing errors.  $\bar{\gamma}_1$  is assumed to be equal to  $\bar{\gamma}_2$ . It can be observed that the achievable average capacity

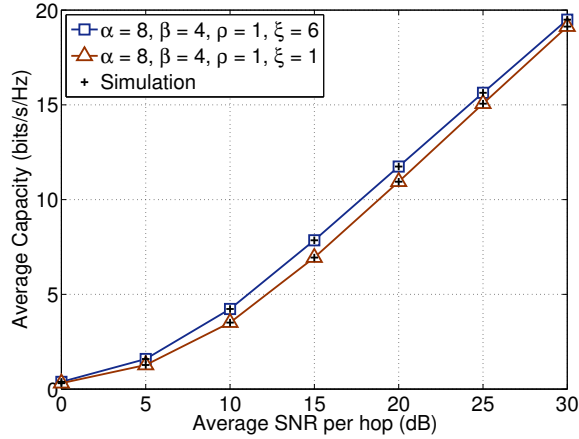


**Figure 4.12:** Average capacity versus the average SNRs per hop ( $\bar{\gamma}_1 = \bar{\gamma}_2$ ) under different turbulence conditions and pointing errors: weak turbulence.

is increased when the atmospheric turbulence is relaxed. Furthermore, the pointing errors exert a considerable effect on the average capacity. More specifically, when the pointing errors become weaker, the average capacity increases (i.e., when  $\xi$  is increased, the average capacity becomes higher).

## 4.8. Conclusions

In this paper, the outage probability, the ABER performance, and the average capacity of mixed mmWave RF/FSO systems over Rician and  $\mathcal{M}$  fading channels were theoretically analyzed. The considered system could be a high-capacity, scalable and cost-effective backhaul solution for the 5G mobile networks. New closed-form expressions for the outage probability, the ABER performance, and the average capacity of the proposed system under various channel conditions were analytically derived. In addition, we derived asymptotic expressions at high SNR regime for the outage probability and the ABER by utilizing the Meijer's G function asymptotic expansion. Our numerical results confirmed that the combined effect of atmospheric turbulence and pointing errors severely degrades the system performance and the quality of the mmWave RF link is of great importance in the overall system performance.

# Chapter 5

## Two-Way Relaying FSO Systems

### 5.1. Introduction

Free space optical (FSO) systems provide a number of benefits compared to radio frequency (RF) counterparts, such as license-free operation, simple installation, low power, and large bandwidth for multiple users [68, 71]. One of the main challenging issues in the design of FSO systems is the impact of weather and atmosphere conditions, especially the atmospheric turbulence, occurring in the free-space channel [118]. As these impairments are distance-dependent [133], relaying FSO has become an effective solution to enhance overall performance and to extend communication coverage [134]. In half-duplex one-way relaying FSO systems [134], the complete data exchange between two terminals over a relay required three or four time phases. This leads to a loss in spectral efficiency due to the pre-log factor one-half in corresponding expressions for the achievable rate (capacity). To overcome the spectral loss, two-way relaying transmission is utilized, in which the relay helps two terminals to exchange their information in two time phases, and hence to achieve the full rate transmission [135].

Recently, two-way transmission has been studied in relaying FSO systems employing either amplify-and-forward (AF) or decode-and-forward (DF) schemes [136]-[144]. In DF-based systems, the received signal at the relay is fully decoded and then



re-encoded before being transmitted to the destination. The performance of two-way DF relaying FSO systems has been intensively studied taking into account different turbulence channel models, from weak-moderate (log-normal) to strong (Gamma-Gamma), with and without pointing errors due to misalignments between the transmitter and the receiver [136]- [142]. On the other hand, the AF-based systems simply amplify the received signal and forward it to the destination, and as a result, they are more attractive due to the simplicity in signal processing at the relay and less power requirements [145]. Recently, the performance of two-way AF relaying FSO systems over Gamma-Gamma channel with pointing errors has been investigated [143, 144]. In these AF relaying systems, however, the *electrical* amplifier is employed. As a result, the overall system bandwidth is limited and additional components for optical/electrical/optical conversion are required [134]. These requirements are daunting from an implementation perspective for Gigabits per second (Gbps)-based FSO links.

Motivated by the fact that *all-optical* AF relaying technique, where amplifying process is performed in optical domain by an optical amplifier, has been recently proposed [117], [146]- [148], the performance of a two-way all-optical AF relaying FSO system over atmospheric turbulence channel is investigated in this paper. For the turbulence channel, we employ the generalized Málaga ( $\mathcal{M}$ ) distribution, which can represent most of existing atmospheric turbulence channel models, including log-normal, Gamma-Gamma, K and Exponential models, as its special cases [119], [120]. The *key contribution* of the paper is the derivation of exact closed-form expressions, in terms of extended generalized bivariate Meijer's G-function (EGBMGF), for the moment generating function (MGF) and the cumulative distribution function (CDF) of the end-to-end signal-to-noise ratio (SNR) over independent but not necessarily identically distributed (i.n.i.d)  $\mathcal{M}$  turbulence channels, with and without pointing errors. These new results are then applied to study the outage probability, the average bit error rate (ABER), and the ergodic achievable-rate of the proposed FSO system. All analytical results are verified via Monte-Carlo (M-C) simulations.

The remainder of the paper is organized as follows. Section 5.2 describes the sys-

tem and channel models accounting for the  $\mathcal{M}$  atmospheric turbulence and pointing errors. In Section 5.3, exact closed-form expressions for the statistical characteristics of the end-to-end SNR including the MGF and the CDF are derived. Subsequently, the performance metrics in terms of outage probability, ABER, and ergodic achievable-rate are analyzed in Section 6.4. Finally, Section 6.5 presents some analytical results validated by M-C simulations, followed by conclusions of the paper in Section 6.6.

## 5.2. System and Channel Models

### 5.2.1. System Model

As illustrated in Fig. 5.1, we consider a dual-hop two-way optical AF relaying FSO system, utilizing the optical subcarrier intensity modulation (SIM) with intensity modulation/direct detection (IM/DD) [149], where two terminals  $T_1$  and  $T_2$  exchange information with the help of a relay terminal  $R$  through the turbulence-induced fading channels with pointing errors. The channel state information (CSI) of all FSO links is assumed to be available at  $T_1$  and  $T_2$  in the beginning of the communication process. All terminals operate in half-duplex fashion, and there is no direct connection between  $T_1$  and  $T_2$ . Each terminal has one transmit aperture to send its information and one receive aperture for receiving the data. The transmission takes place in two phases, namely *multiple-access (MA) phase* and *broadcast (BC) phase*.

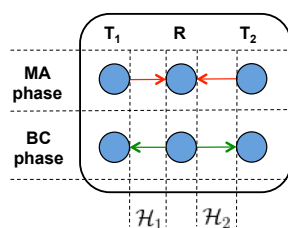


**Figure 5.1:** System model of a two-way all-optical AF relaying FSO system.

In the *MA phase*, the source data at  $T_1$  and  $T_2$  are modulated onto the RF subcarrier signals  $x_1(t)$  and  $x_2(t)$ , respectively. After being properly biased, the RF

signals are used to modulate the irradiance of continuous wave optical beams at the laser transmitters, and the output optical signals can be expressed as

$$y_{T_1}(t) = P_{T_1}(1 + \eta x_1(t)) \text{ and } y_{T_2}(t) = P_{T_2}(1 + \eta x_2(t)), \quad (5.1)$$

where  $P_{T_1}$ ,  $P_{T_2}$  are the transmit optical powers at  $T_1$  and  $T_2$ , respectively.  $\eta$  is the modulation index satisfying the conditions  $-1 < \eta x_1(t) < 1$  and  $-1 < \eta x_2(t) < 1$  to avoid overmodulation. The output optical signals are then transmitted simultaneously to the relay  $R$ . At both receiving lens of  $R$ , received optical signals include data signal and background noise. The received optical signals from  $T_1$  and  $T_2$  are then combined by an optical coupler and the combined optical signal, denoted as  $y_R(t)$ , can be expressed as

$$y_R(t) = P_{T_1}(1 + \eta x_1(t))\mathcal{H}_1 + P_{T_2}(1 + \eta x_2(t))\mathcal{H}_2 + n_R(t), \quad (5.2)$$

where  $\mathcal{H}_1$  and  $\mathcal{H}_2$  are independent  $\mathcal{M}$ -distributed fading channel gains of  $T_1 \rightarrow R$  and  $T_2 \rightarrow R$  links. Without loss of generality, we assume that all channels are reciprocal (i.e., the channel gains of  $T_i \rightarrow R$  and  $R \rightarrow T_i$  ( $i \in \{1, 2\}$ ) links are identical).  $n_R \sim \mathcal{N}(0, N_0)$  is the additive white Gaussian noise (AWGN) with zero mean and variance  $N_0$  at the relay, due to the background noise [117]. After the DC components of  $y_R(t)$  are filtered out and assuming that  $P_{T_1} = P_{T_2} = P_T$ , (5.2) can be rewritten as

$$y_R(t) = \eta P_T \mathcal{H}_1 x_1(t) + \eta P_T \mathcal{H}_2 x_2(t) + n_R(t). \quad (5.3)$$

To meet the average transmit power constraint at  $R$ , the combined optical signal is then amplified by an optical amplifier with a variable gain  $G$ , which can be expressed as

$$G = \sqrt{\frac{P_R}{P_T (\eta \mathcal{H}_1)^2 + P_T (\eta \mathcal{H}_2)^2 + N_0}}, \quad (5.4)$$

where  $P_R$  is the transmitted power at the relay. Without loss of generality, we assume

that  $P_T = P_R = P_0$ , and  $P_0 \gg N_0$  [135].

In the **BC phase**, the amplified optical signal, together with amplified spontaneous emission (ASE) noise at the output of the optical amplifier<sup>8</sup>, is forwarded to both terminals  $T_1$  and  $T_2$ . At terminal  $T_i$ , the received optical intensity is converted into an electrical signal through direct detection at the photodetector<sup>9</sup>. Thus, the received photocurrent at terminal  $T_i$  can be expressed as

$$y_{T_i}(t) = \Re \mathcal{H}_i(1 + \eta G y_R(t)) + n_{T_i}(t), \quad (5.5)$$

where  $\Re$  is the responsivity of the photodetector, and  $n_{T_i} \sim \mathcal{N}(0, N_0)$  is AWGN. Substituting (5.3) and (5.4) into (5.5) and after filtering out the DC component and removing the self-interference terms, the instantaneous SNRs of terminal  $T_i$  in the BC phase can be given as [135], [150]

$$\Gamma_{T_i} = \frac{\gamma_i \gamma_j}{2\gamma_i + \gamma_j} = \left( \frac{1}{\gamma_i} + \frac{2}{\gamma_j} \right)^{-1}, \quad (5.6)$$

where  $\gamma_i = \frac{\Re \eta^2 P_0 (\mathcal{H}_i)^2}{N_0}$  and  $\gamma_j = \frac{\Re \eta^2 P_0 (\mathcal{H}_j)^2}{N_0}$  ( $i, j \in \{1, 2\}$  and  $i \neq j$ ) are the instantaneous SNRs for  $T_i \rightarrow R$  and  $R \rightarrow T_j$  links, respectively.

### 5.2.2. Channel Model

The channel coefficient  $\mathcal{H}_i = h_{a_i} h_{m_i}$ , where  $i \in \{1, 2\}$ , incorporates the atmospheric turbulence-induced fading coefficient  $h_{a_i}$  and pointing errors  $h_{m_i}$ . We assume that the receive aperture is sufficiently isolated so that the scintillation sequences are uncorrelated [151]. Due to this assumption, the channels in the analysis are considered to be independent but not necessarily identical (i.n.i.d) [141]. All channels are also assumed to be quasi-static for two time phases.

<sup>8</sup>As background illumination is by far the dominant noise in FSO systems [117, 146], the impact of ASE noise is therefore neglected in our analysis.

<sup>9</sup>In practice, a precise characterization of photodetectors requires a complicated statistical model, which is analytically intractable. When the intensity of the received signal is sufficiently high and the background radiation is dominant, particularly in all-optical relaying FSO systems [117], [146], the noise can be modeled as AWGN with high accuracy [149].

### 5.2.2.1. $\mathcal{M}$ Atmospheric Turbulence Model

The fading coefficient  $h_{a_i}$  ( $h_{a_i} > 0$ ) is assumed to be distributed with  $\mathcal{M}$ -distribution. This  $\mathcal{M}$  distribution unifies most of the statistical models (including the most widely used log-normal<sup>10</sup> and Gamma-Gamma as special cases) derived until now in the literature in a closed-form expression [21, Table 1], and also provides an excellent agreement with simulation data over the whole range of turbulence conditions (i.e., weak to strong). The main contribution of the  $\mathcal{M}$  distribution is the inclusion of the additional *scattered component* coupled to the *line-of-sight (LOS) component* of the propagating optical beam (see [21, Fig. 1]), which is commonly ignored in other turbulence models.

The  $\mathcal{M}$ -distribution statistically models an FSO channel taking into account three components: (1) a LOS component  $U_L$ , (2) a component  $U_S^C$  which is coupled to the  $U_L$  and quasi-forward scattered by the eddies on the propagation axis, and (3)  $U_S^G$  component which is due to energy that is scattered to the receiver by off-axis eddies. The probability density function (PDF) of  $h_{a_i} \sim \mathcal{M}(\alpha_i, \beta_i, \rho_i, \tau_i, \Omega_i)$  can be given as

$$f_{h_{a_i}}(h_{a_i}) = \chi_i \sum_{k=1}^{\beta_i} a_i(k) h_{a_i}^{\frac{\alpha_i+k}{2}-1} K_{v_i} \left( 2 \sqrt{\frac{\alpha_i \beta_i h_{a_i}}{\tau_i \beta_i + \Omega_i'}} \right), \quad (5.7)$$

where  $K_{v_i}(\cdot)$  is the modified Bessel function of the second kind and order  $v_i$ , with  $v_i = \alpha_i - k$ . Corresponding to channel  $h_{a_i}$ , the positive parameter  $\alpha_i$  represents the effective number of large scale cells of the scattering process,  $\beta_i$  is a natural number that represents amount of turbulence-induced fading<sup>11</sup>. Other parameters in (5.7) are

<sup>10</sup>It is noted that the log-normal distribution does not have an exact relation with  $\mathcal{M}$  distribution, instead it is an approximate special case of  $\mathcal{M}$  distribution [119].

<sup>11</sup>The notation  $\beta_i$  is limited to a natural number so that (5.7) will have a finite summation. It is noteworthy that there is a generalized expression of (5.7) given in [21, (22)] for  $\beta_i$  being a real number. However, this case is less interesting due to the high degree of freedom of the proposed distribution and the infinite summation.

expressed as follows.

$$\chi_i = \frac{2\alpha_i^{\frac{\alpha_i}{2}}}{\tau_i^{1+\frac{\alpha_i}{2}} \Gamma(\alpha_i)} \left( \frac{\tau_i \beta_i}{\tau_i \beta_i + \Omega'_i} \right)^{\beta_i + \frac{\alpha_i}{2}}, \quad (5.8)$$

$$\tau_i = 2b_{0_i} (1 - \rho_i), \quad (5.9)$$

$$a_i(k) = \binom{\beta_i - 1}{k - 1} \frac{(\tau_i \beta_i + \Omega'_i)^{1 - \frac{k}{2}}}{(k - 1)!} \left( \frac{\Omega'_i}{\tau_i} \right)^{(k-1)} \left( \frac{\alpha_i}{\beta_i} \right)^{\frac{k}{2}}, \quad (5.10)$$

$$\Omega'_i = \Omega_i + 2\rho_i b_{0_i} + 2\sqrt{2b_{0_i} \rho_i \Omega_i} \cos(\phi_{1_i} - \phi_{2_i}). \quad (5.11)$$

Here,  $2b_{0_i}$  is the average power of total scattered component (i.e.,  $(U_S^G + U_S^C)$ ).  $\rho_i$  ( $0 \leq \rho_i \leq 1$ ) represents the amount of scattering power coupled to the LOS component, and thus the turbulence intensity reduces as the parameter  $\rho_i$  increases.  $\Omega_i$  is the average power of the LOS component  $U_L$ ,  $\phi_{1_i}$  and  $\phi_{2_i}$  are the deterministic phases of the LOS component  $U_L$  and the coupled-to-LOS component  $U_S^C$ , respectively.  $\Gamma(\cdot)$  denotes Gamma function defined as  $\Gamma(w) \triangleq \int_0^\infty t^{w-1} e^{-t} dt$ , and  $\binom{\cdot}{\cdot}$  denotes the binomial coefficient.

### 5.2.2.2. Pointing Errors Model

The statistical characterization of the pointing error impairments is given in [112], where a Gaussian spatial intensity profile is assumed for the beam waist. The PDF of pointing error coefficient  $h_{m_i}$  is given as

$$f_{h_{m_i}}(h_{m_i}) = \frac{\xi_i^2}{A_0^{\xi_i^2}} h_{m_i}^{\xi_i^2 - 1}, \quad 0 \leq h_{m_i} \leq A_0, \quad (5.12)$$

where  $A_0$  is a constant term defining the pointing loss given by  $A_0 = [\text{erf}(v)]^2$ , with  $\text{erf}(z) \triangleq \frac{2}{\sqrt{\pi}} \int_0^z e^{-t^2} dt$  is the error function,  $v = \sqrt{\pi}\varepsilon/(\sqrt{2}w_z)$  where  $\varepsilon$  is the radius of the detection aperture, and  $w_z$  is the beam waist.  $\xi_i$  is the ratio between the equivalent beam radius at the receiver and the pointing error displacement standard deviation (jitter) at the receiver (i.e., when  $\xi \rightarrow \infty$ , (5.12) corresponds to the *non-pointing errors* case).

### 5.2.2.3. Composite Atmospheric Channel Model

The joint distribution of  $\mathcal{H}_i = h_{a_i}h_{m_i}$  can be derived by utilizing

$$\begin{aligned} f_{\mathcal{H}_i}(\mathcal{H}_i) &= \int_{\mathcal{H}_i/A_0}^{\infty} f_{h_{a_i}}(h_{a_i}) f_{\mathcal{H}_i|h_{a_i}}(\mathcal{H}_i|h_{a_i}) dh_{h_{a_i}} \\ &= \int_{\mathcal{H}_i/A_0}^{\infty} f_{h_{a_i}}(h_{a_i}) \frac{\mathcal{H}_i}{h_{a_i}} f_{h_{m_i}}\left(\frac{\mathcal{H}_i}{h_{a_i}}\right) dh_{h_{a_i}}. \end{aligned} \quad (5.13)$$

By applying simple random variable transformation on (5.7) and using (5.13), we obtain the PDF of  $\mathcal{H}_i$  as

$$f_{\mathcal{H}_i}(\mathcal{H}_i) = \frac{\xi_i^2 \chi_i}{2\mathcal{H}_i} \sum_{k=1}^{\beta_i} a_i(k) (\Theta_i)^{-\frac{\alpha_i+k}{2}} G_{1,3}^{3,0} \left( \frac{\Theta_i \mathcal{H}_i}{A_0} \middle| \begin{matrix} \xi_i^2 + 1 \\ \xi_i^2, \alpha_i, k \end{matrix} \right), \quad (5.14)$$

where  $G_{p,q}^{m,n}(\cdot | \cdot)$  is the Meijer's G function [27, (9.301)]<sup>12</sup>, and  $\Theta_i = \frac{\alpha_i \beta_i}{\tau_i \beta_i + \Omega_i}$ . The unified performance analysis of FSO links over  $\mathcal{M}$  turbulence channels with pointing errors was recently reported in [152].

---

<sup>12</sup>The Meijer's G function provides a simple and tractable mathematical solution and can be easily computed using standard software packages such as Mathematica and Matlab.

### 5.3. Statistical Characterization of The End-to-end SNR, $\Gamma_{T_i}$

Under the combined effects of turbulence fading and pointing errors, the instantaneous SNR  $\gamma_i$  ( $i \in \{1, 2\}$ ) can be expressed as  $\gamma_i = (\bar{\gamma}_i/A_0^2) (\mathcal{H}_i)^2$ , where  $\bar{\gamma}_i = \frac{\Re\eta^2 A_0^2 P_0 \mathbb{E}\{\mathcal{H}_i^2\}}{N_0}$  is the corresponding average SNR, with  $\mathbb{E}\{\mathcal{H}_i^2\}$  is the respective variance of  $\mathcal{H}_i$  and  $\mathbb{E}\{\cdot\}$  denotes the statistical average operator. Hence, the PDF of  $\gamma_i$  can be written as

$$f_{\gamma_i}(\gamma_i) = \frac{\xi_i^2 \chi_i}{4\gamma_i} \sum_{k=1}^{\beta_i} a_i(k) (\Theta_i)^{-\frac{\alpha_i+k}{2}} G_{1,3}^{3,0} \left( \Theta_i \sqrt{\frac{\gamma_i}{\bar{\gamma}_i}} \left| \begin{matrix} \xi_i^2 + 1 \\ \xi_i^2, \alpha_i, k \end{matrix} \right. \right). \quad (5.15)$$

#### Lemma 1

The MGF of a  $\mathcal{M}$ -distributed random variable  $\frac{1}{\gamma_i}$  is given by

$$\begin{aligned} \mathcal{M}_{\frac{1}{\gamma_i}}(s) &= \frac{\xi_i^2 \chi_i}{16\pi} \sum_{k=1}^{\beta_i} 2^{\alpha_i+k} a_i(k) (\Theta_i)^{-\frac{\alpha_i+k}{2}} \\ &\times G_{2,7}^{7,0} \left( \frac{\Theta_i^2 s}{16\bar{\gamma}_i} \left| \begin{matrix} \frac{\xi_i^2+1}{2}, \frac{\xi_i^2+2}{2} \\ \frac{\xi_i^2}{2}, \frac{\xi_i^2+1}{2}, \frac{\alpha_i}{2}, \frac{\alpha_i+1}{2}, \frac{k}{2}, \frac{k+1}{2}, 0 \end{matrix} \right. \right), \end{aligned} \quad (5.16)$$

**Proof:** The MGF of  $\frac{1}{\gamma_i}$  can be written as  $\mathcal{M}_{\frac{1}{\gamma_i}}(s) = \int_0^\infty \exp\left(\frac{-s}{\gamma_i}\right) f_{\gamma_i}(\gamma_i) d\gamma_i$  [153]. Now substituting  $f_{\gamma_i}(\gamma_i)$  in (5.15) and using [27, (9.31.2)] together with the identity  $e^{-x} = G_{0,1}^{1,0}\left(x \left| \begin{matrix} - \\ 0 \end{matrix} \right. \right)$  [30, (11)] and integrating with the help of [30, (21)],  $\mathcal{M}_{\frac{1}{\gamma_i}}(s)$  can be derived as in (5.16).

#### Lemma 2



The MGF of a  $\mathcal{M}$ -distributed random variable  $\frac{2}{\gamma_j}$  is given by

$$\begin{aligned} \mathcal{M}_{\frac{2}{\gamma_j}}(s) &= \frac{\xi_j^2 \chi_j}{16\pi} \sum_{l=1}^{\beta_j} 2^{\alpha_j+l} a_j(l) (\Theta_j)^{-\frac{\alpha_j+l}{2}} \\ &\times G_{2,7}^{7,0} \left( \frac{\Theta_j^2 s}{8\gamma_j} \middle| \frac{\xi_j^2+1}{2}, \frac{\xi_j^2+2}{2} \right. \\ &\left. \middle| \frac{\xi_j^2}{2}, \frac{\xi_j^2+1}{2}, \frac{\alpha_j}{2}, \frac{\alpha_j+1}{2}, \frac{l}{2}, \frac{l+1}{2}, 0 \right), \end{aligned} \quad (5.17)$$

**Proof:** It is straightforward to obtain the MGF of  $\frac{2}{\gamma_j}$  as

$$\mathcal{M}_{\frac{2}{\gamma_j}}(s) = \int_0^\infty \exp\left(\frac{-2s}{\gamma_j}\right) f_{\gamma_j}(\gamma_j) d\gamma_j. \quad (5.18)$$

Following the same approach as in the Proof of Lemma 1,  $\mathcal{M}_{\frac{2}{\gamma_j}}(s)$  can be derived as in (5.17).

### Theorem 1

The MGF of  $\Gamma_{T_i}$ , denoted as  $\mathcal{M}_{\Gamma_{T_i}}$  can be given in a closed-form expression as

$$\begin{aligned} \mathcal{M}_{\Gamma_{T_i}}(s) &= 1 - \frac{\xi_i^2 \xi_j^2 \chi_i \chi_j}{128\pi^2} \sum_{k=1}^{\beta_i} \sum_{l=1}^{\beta_j} 2^{\alpha_i+\alpha_j+k+l} a_i(k) a_j(l) \\ &\times \Theta_i^{-\frac{\alpha_i+k}{2}} \Theta_j^{-\frac{\alpha_j+l}{2}} S \left[ \begin{array}{c} \left[ \begin{array}{cc} 1 & 0 \\ 1 & 0 \\ 0 & 7 \\ 2 & 0 \\ 0 & 7 \\ 2 & 0 \end{array} \right] \middle| \begin{array}{c} 1, 0; - \\ \Xi_1; \Xi_2 \\ \Xi_3; \Xi_4 \end{array} \middle| \begin{array}{c} \frac{\Psi_1}{s} \\ \frac{\Psi_2}{s} \end{array} \end{array} \right], \end{aligned} \quad (5.19)$$

where  $\Psi_1 = \frac{\Theta_i^2}{16\gamma_i}$ ,  $\Psi_2 = \frac{\Theta_j^2}{8\gamma_j}$ ,  $\Xi_1 = \left\{ \frac{\xi_i^2+1}{2}, \frac{\xi_i^2+2}{2} \right\}$ ,  $\left\{ \Xi_2 = \frac{\xi_i^2}{2}, \frac{\xi_i^2+1}{2}, \frac{\alpha_i}{2}, \frac{\alpha_i+1}{2}, \frac{k}{2}, \frac{k+1}{2}, 0 \right\}$ ,  $\left\{ \Xi_3 = \frac{\xi_j^2+1}{2}, \frac{\xi_j^2+2}{2} \right\}$ , and  $\left\{ \Xi_4 = \frac{\xi_j^2}{2}, \frac{\xi_j^2+1}{2}, \frac{\alpha_j}{2}, \frac{\alpha_j+1}{2}, \frac{l}{2}, \frac{l+1}{2}, 0 \right\}$ .

**Proof:** From (5.6), the MGF of  $\Gamma_{T_i}$  can be written as [30, (3)]

$$\begin{aligned} \mathcal{M}_{\Gamma_{T_i}}(s) &= 1 - \sqrt{s} \int_0^{\pi/2} \frac{\sec^2(\varphi)}{\sqrt{\tan(\varphi)}} J_1\left(2\sqrt{\tan(\varphi)s}\right) \\ &\quad \times \mathcal{M}_{\frac{1}{\gamma_i}}(\tan(\varphi)) \mathcal{M}_{\frac{2}{\gamma_j}}(\tan(\varphi)) d(\varphi), \end{aligned} \quad (5.20)$$

where  $J_v(\cdot)$  represents the Bessel function of the first kind and order  $v$ . By changing the variable  $\tan(\varphi) = p^2$ , (5.20) is rewritten as

$$\mathcal{M}_{\Gamma_{T_i}}(s) = 1 - 2\sqrt{s} \int_0^\infty J_1(2\sqrt{sp}) \mathcal{M}_{\frac{1}{\gamma_i}}(p^2) \mathcal{M}_{\frac{2}{\gamma_j}}(p^2) dp. \quad (5.21)$$

Applying Lemma 1 and Lemma 2, (5.21) can be expressed as

$$\begin{aligned} \mathcal{M}_{\Gamma_{T_i}}(s) &= 1 - \frac{\sqrt{s} \xi_i^2 \xi_j^2 \chi_i \chi_j}{128\pi^2} \sum_{k=1}^{\beta_i} \sum_{l=1}^{\beta_j} 2^{\alpha_i + \alpha_j + k + l} a_i(k) a_j(l) \\ &\quad \times \Theta_i^{-\frac{\alpha_i + k}{2}} \Theta_j^{-\frac{\alpha_j + l}{2}} \int_0^\infty I(p) dp, \end{aligned} \quad (5.22)$$

where  $I(p) = J_1(2\sqrt{sp}) G_{2,7}^{7,0} \left( \Psi_1 p^2 \left| \begin{matrix} \Xi_1 \\ \Xi_2 \end{matrix} \right. \right) G_{2,7}^{7,0} \left( \Psi_2 p^2 \left| \begin{matrix} \Xi_3 \\ \Xi_4 \end{matrix} \right. \right)$ . Using [31, (6)], the multiplication of two Meijer's G-functions in (5.22) can be written in terms of a EGBMGF denoted as  $S[\cdot]$  [32, (1.1)]<sup>13</sup>. Then, integrating with the use of identity [32, (3.4)], the exact closed-form expression of  $\mathcal{M}_{\Gamma_{T_i}}(s)$  is obtained as given in (5.19).

### Corollary 1

<sup>13</sup>It is noted that the EGBMGF cannot be directly computed by current versions of standard software packages such as Matlab and Mathematica. In general, it must be computed by its definition in terms of the double Mellin-Barnes type integrals [32, (1.1)]. With the help of [131] and [130], the two-fold Mellin-Barnes integral can be accurately evaluated by Matlab and Mathematica, respectively. The use of EGBMGF as a closed-form solution has been widely accepted in the literature.

Using Theorem 1, the CDF of  $\Gamma_{T_i}$ , denoted as  $\mathcal{F}_{\Gamma_{T_i}}(\gamma)$ , is given as

$$\mathcal{F}_{\Gamma_{T_i}}(\gamma) = 1 - \frac{\xi_i^2 \xi_j^2 \chi_i \chi_j}{256 \pi^2} \sum_{k=1}^{\beta_i} \sum_{l=1}^{\beta_j} 2^{\alpha_i + \alpha_j + k + l} a_i(k) a_j(l) \times \Theta_i^{-\frac{\alpha_i + k}{2}} \Theta_j^{-\frac{\alpha_j + l}{2}} \mathcal{S} \left[ \begin{array}{c|c|c} \left[ \begin{array}{c} 0 \\ 1 \end{array} \right] & 0; - & \Psi_1 \gamma \\ \left( \begin{array}{c} 0 \\ 2 \end{array} \right) & \Xi_1; \Xi_2 & \Psi_2 \gamma \\ \left( \begin{array}{c} 0 \\ 2 \end{array} \right) & \Xi_3; \Xi_4 & \end{array} \right]. \quad (5.23)$$

**Proof:** The CDF of  $\Gamma_{T_i}$  is defined as  $\mathcal{F}_{\Gamma_{T_i}}(\gamma) = \mathcal{L}^{-1} \left[ \frac{1}{s} \mathcal{M}_{\Gamma_{T_i}}(s) \right]$ , where  $\mathcal{L}^{-1}$  denotes the inverse Laplace transform operator. Substituting  $\mathcal{M}_{\Gamma_{T_i}}(s)$  from (5.19) and using the identity [32, (2.7)], a closed-form expression of  $\mathcal{F}_{\Gamma_{T_i}}(\gamma)$  is obtained as in (7.3).

## 5.4. Performance Analysis

### 5.4.1. Outage probability

The outage probability at  $T_i$ , denoted as  $P_{\text{out}, T_i}(\gamma_{th})$ , is defined as the probability that the instantaneous SNR falls below a given threshold  $\gamma_{th}$ , which can be expressed as

$$P_{\text{out}, T_i}(\gamma_{th}) = \Pr(\gamma_{T_i} < \gamma_{th}) = \mathcal{F}_{\Gamma_{T_i}}(\gamma_{th}), \quad (5.24)$$

where  $\mathcal{F}_{\Gamma_{T_i}}(\gamma_{th})$  is the CDF of the instantaneous SNR at terminal  $T_i$  in (7.3) evaluated at  $\gamma = \gamma_{th}$ . Hence, the novel exact closed-form expression of the outage probability of all-optical two-way AF relaying FSO systems can be derived by using (7.3) and (5.24). The outage probability at both terminals  $T_1$  and  $T_2$  are the same since reciprocal channels are assumed. Following the same approach, the outage probability for non-

reciprocal channels can also be derived.

### 5.4.2. Average Bit Error Rate

The average bit error rate (ABER) is a useful measure of evaluating the performance of wireless communication applications. Conventionally, the ABER at terminal  $T_i$  is computed by determining the PDF of the end-to-end SNR at terminal  $T_i$  (denoted as  $\mathcal{P}_{\Gamma_{T_i}}$ ) and then averaging the conditional bit error probability (BEP) in an AWGN channel (denoted as  $P_b(e|\gamma)$ ), over this PDF. Therefore, the ABER, denoted as  $P_b(e)$ , can be expressed as

$$P_b(e) = \int_0^{\infty} P_b(e|\gamma) \mathcal{P}_{\Gamma_{T_i}}(\gamma) d\gamma, \quad (5.25)$$

where  $P_b(e|\gamma) = Q(\sqrt{\kappa\gamma})$  given by [155], with  $\kappa$  is a constant and  $Q(x) \triangleq \frac{1}{\sqrt{2\pi}} \int_0^{\infty} e^{-t^2/2} dt$  is the Gaussian Q-function. After integration by parts,  $P_b(e)$  can be rewritten as

$$P_b(e) = \frac{1}{\sqrt{2\pi}} \int_0^{\infty} \mathcal{F}_{\Gamma_{T_i}}\left(\frac{t^2}{\kappa}\right) e^{-\frac{t^2}{2}} dt. \quad (5.26)$$

Making the change of variable  $x = t^2$ ,  $P_b(e)$  is expressed as

$$P_b(e, \kappa) = \frac{1}{\sqrt{2\pi}} \int_0^{\infty} \mathcal{F}_{\Gamma_{T_i}}\left(\frac{x}{\kappa}\right) e^{-\frac{x}{2}} \frac{dx}{2\sqrt{x}}. \quad (5.27)$$

Now plugging (7.3) into (5.27), then using [27, (3.361.2)] and [32, (2.1)], (5.27) can be derived in a closed-form expression as

$$P_b(e) = \frac{1}{2} - \frac{\xi_i^2 \xi_j^2 \chi_i \chi_j}{512 \pi^{5/2}} \sum_{k=1}^{\beta_i} \sum_{l=1}^{\beta_j} 2^{\alpha_i + \alpha_j + k + l} a_i(k) a_j(l)$$

$$\times \Theta_i^{-\frac{\alpha_i + k}{2}} \Theta_j^{-\frac{\alpha_j + l}{2}} S \left[ \begin{array}{c} \left[ \begin{array}{c} 1 \\ 1 \\ 0 \\ 2 \\ 0 \\ 2 \end{array} \right] \\ \left[ \begin{array}{c} 0 \\ 7 \\ 0 \\ 7 \\ 2 \\ 0 \end{array} \right] \end{array} \middle| \begin{array}{c} \frac{1}{2}, 0; - \\ \Xi_1; \Xi_2 \\ \Xi_3; \Xi_4 \end{array} \middle| \begin{array}{c} \\ \frac{2\Psi_1}{\kappa} \\ \frac{2\Psi_2}{\kappa} \end{array} \right]. \quad (5.28)$$

The ABER of  $M$ -ary phase shift keying ( $M$ -PSK) constellations with Gray coding can be approximated as [156]

$$P_{b,MP SK}(e) \cong \frac{2}{\max(\log_2 M, 2)} \sum_{p=1}^{\max(\frac{M}{4}, 1)} P_b(e, \kappa_{p,MP SK}), \quad (5.29)$$

where  $\kappa_{p,MP SK} = 2(\log_2 M) \sin^2((2p-1)\frac{\pi}{M})$ , and  $P_b(e, \kappa_{p,MP SK})$  can be derived in a closed-form expression by substituting  $\kappa_{p,MP SK}$  with  $\kappa$  in (5.28). Similarly, the corresponding ABER for  $M$ -ary quadrature amplitude modulation ( $M$ -QAM) constellations with Gray coding is also approximated as [156]

$$P_{b,MQ AM}(e) \cong \frac{4}{\log_2 M} \left(1 - \frac{1}{\sqrt{M}}\right) \sum_{q=1}^{\frac{\sqrt{M}}{2}} P_b(e, \kappa_{q,MQ AM}), \quad (5.30)$$

where  $\kappa_{q,MQ AM} = 3(2q-1)^2 \frac{\log_2 M}{M-1}$ , and  $P_b(e, \kappa_{q,MQ AM})$  can be derived by substituting  $\kappa_{q,MQ AM}$  into (5.28).

### 5.4.3. Ergodic Achievable-Rate

It is well known that atmospheric turbulence over FSO link results in slowly-varying fading. Since the coherence time of the channel is about 1–100 ms, turbulence-

induced fading remains constant over a large number of transmitted bits. Since the coherence time of the FSO fading channel is in the order of milliseconds, a single fade can obliterate millions of bits at Gbps data rates. Therefore, the average (i.e., ergodic) capacity of the channel, represents the best achievable capacity of an FSO link. The ergodic capacity in our analysis is valid under the presence of pointing errors with the assumption that the information symbol is long enough to ensure the long-term ergodic properties of the turbulence process [152], [126].

The ergodic achievable-rate of two-way AF relaying FSO systems is defined as the summation of the ergodic capacities  $\mathcal{C}_1$  and  $\mathcal{C}_2$  when information flows from  $T_1 \rightarrow R \rightarrow T_2$  and  $T_2 \rightarrow R \rightarrow T_1$ , respectively. Let  $\mathcal{A}_{sum}$  denote the ergodic achievable-rate, we have

$$\mathcal{A}_{sum} = \sum_{i=1}^2 \mathcal{C}_i, \quad (5.31)$$

in which  $\mathcal{C}_i$  can be expressed as  $\mathcal{C}_i = \frac{1}{2\ln 2} \int_0^\infty \frac{1}{s} (1 - e^{-s}) \mathcal{M}_{\frac{1}{\Gamma_{T_i}}}(s) ds$ , where  $\frac{1}{2}$  is due to the half-duplex relaying and  $\mathcal{M}_{\frac{1}{\Gamma_{T_i}}}$  is the MGF of the inverse of  $\Gamma_{T_i}$  [144]. From (5.6), since  $\gamma_i$  and  $\gamma_j$  are statistically independent random variables, we have  $\mathcal{M}_{\frac{1}{\Gamma_{T_i}}}(s) = \mathcal{M}_{\frac{1}{\gamma_i}}(s) \times \mathcal{M}_{\frac{2}{\gamma_j}}(s)$ . Thus,  $\mathcal{C}_i$  can be rewritten as

$$\mathcal{C}_i = \frac{1}{2\ln 2} (I_1 - I_2), \quad (5.32)$$

where  $I_1 = \int_0^\infty \frac{1}{s} \mathcal{M}_{\frac{1}{\gamma_i}}(s) \times \mathcal{M}_{\frac{2}{\gamma_j}}(s) ds$  and  $I_2 = \int_0^\infty \frac{1}{s} e^{-s} \mathcal{M}_{\frac{1}{\gamma_i}}(s) \times \mathcal{M}_{\frac{2}{\gamma_j}}(s) ds$ .

To evaluate  $\mathcal{C}_i$ , we will derive closed-form expressions for  $I_1$  and  $I_2$  separately. Firstly, the closed-form expression of  $I_1$  can be derived by substituting (5.16) and (5.17) into  $I_1$ , and integrating with the help of [30, (21)]. Thus,  $I_1$  can be expressed

as

$$I_1 = \frac{\xi_i^2 \xi_j^2 \chi_i \chi_j}{256\pi^2} \sum_{k=1}^{\beta_i} \sum_{l=1}^{\beta_j} 2^{\alpha_i + \alpha_j + k + l} a_i(k) a_j(l) \Theta_i^{-\frac{\alpha_i + k}{2}} \Theta_j^{-\frac{\alpha_j + l}{2}} \times G_{9,9}^{7,7} \left( \begin{matrix} \Psi_2 \bar{\gamma}_1 \\ \Psi_1 \bar{\gamma}_2 \end{matrix} \middle| \begin{matrix} \Upsilon_1, 1, \Upsilon_2 \\ \Upsilon_3, 0, \Upsilon_4 \end{matrix} \right), \quad (5.33)$$

where

$$\Upsilon_1 = \left\{ \frac{2 - \xi_i^2}{2}, \frac{1 - \xi_i^2}{2}, \frac{2 - \alpha_i}{2}, \frac{1 - \alpha_i}{2}, \frac{2 - k}{2}, \frac{1 - k}{2} \right\}, \quad (5.34)$$

$$\Upsilon_2 = \left\{ \frac{\xi_j^2 + 1}{2}, \frac{\xi_j^2 + 2}{2} \right\}, \quad (5.35)$$

$$\Upsilon_3 = \left\{ \frac{\xi_j^2}{2}, \frac{\xi_j^2 + 1}{2}, \frac{\alpha_j}{2}, \frac{\alpha_j + 1}{2}, \frac{l}{2}, \frac{l + 1}{2} \right\}, \quad (5.36)$$

$$\Upsilon_4 = \left\{ \frac{1 - \xi_i^2}{2}, \frac{-\xi_i^2}{2} \right\}. \quad (5.37)$$

Secondly, the closed-form expression of  $I_2$  can be derived by substituting (5.16) and (5.17) into  $I_2$  and applying [31, (6)], then integrating with the help of [32, (2.1)].

Thus,  $I_2$  can be expressed as

$$I_2 = \frac{\xi_i^2 \xi_j^2 \chi_i \chi_j}{256\pi^2} \sum_{k=1}^{\beta_i} \sum_{l=1}^{\beta_j} 2^{\alpha_i + \alpha_j + k + l} a_i(k) a_j(l) \Theta_i^{-\frac{\alpha_i + k}{2}} \Theta_j^{-\frac{\alpha_j + l}{2}} \times S \left[ \begin{matrix} \left[ \begin{matrix} 1 & 0 \\ 0 & 0 \end{matrix} \right] \\ \left( \begin{matrix} 0 & 7 \\ 2 & 0 \end{matrix} \right) \\ \left( \begin{matrix} 0 & 7 \\ 2 & 0 \end{matrix} \right) \end{matrix} \middle| \begin{matrix} 0, -, - \\ \Xi_1; \Xi_2 \\ \Xi_3; \Xi_4 \end{matrix} \right. \left. \begin{matrix} \Psi_1 \\ \Psi_2 \end{matrix} \right], \quad (5.38)$$

where  $\Xi_1, \Xi_2, \Xi_3, \Xi_4, \Psi_1$ , and  $\Psi_2$  are defined in (5.19). Substituting (5.33) and (5.38) into (5.32), a closed-form expression for  $\mathcal{C}_i$  can be straightforwardly obtained, and hence we finally derive the closed-form expression for  $\mathcal{A}_{sum}$  in (5.31).

## 5.5. Numerical Results

In this section, FSO links are considered with link lengths of  $L = 1$  km and wavelength of  $\lambda = 785$  nm. The refractive structure index, denoted as  $C_n^2$ , is considered in three cases as  $C_n^2 = 1.2 \times 10^{-13} \text{ m}^{-2/3}$ ,  $C_n^2 = 10^{-11} \text{ m}^{-2/3}$ , and  $C_n^2 = 2.8 \times 10^{-14} \text{ m}^{-2/3}$ . These parameters are then utilized to obtain the Rytov variance  $\sigma_R^2 = 1.23C_n^2(2/\pi)^{7/6}L^{11/6}$  defining the effects of atmospheric turbulence as  $\alpha_1 = \alpha_2 = 2.296$ ,  $\beta_1 = \beta_2 = 2$  (i.e., strong turbulence),  $\alpha_1 = \alpha_2 = 4.2$ ,  $\beta_1 = \beta_2 = 3$  (i.e., moderate turbulence), and  $\alpha_1 = \alpha_2 = 8$ ,  $\beta_1 = \beta_2 = 4$  (i.e., weak turbulence) [152]. Some other parameters used in our analysis are chosen as  $\Omega_1 = \Omega_2 = 1.3265$ ,  $b_{01} = b_{02} = 0.1079$ ,  $\phi_{1i} - \phi_{2i} = \pi/2$  [119, 120, 152]. Furthermore, from (5.6) we define the average SNR of the  $T_i \rightarrow R$  link as  $\bar{\gamma}_i = \delta_i \gamma_0$  ( $i \in \{1, 2\}$ ), where  $\gamma_0$  is the *average transmit SNR* and  $\delta_i = \mathbb{E}\{\mathcal{H}_i^2\}$  is the respective variance of  $\mathcal{H}_i$ , to compare two cases of i.n.i.d (e.g.,  $\delta_1 = 3, \delta_2 = 5$ ) and i.i.d (e.g.,  $\delta_1 = \delta_2 = 1$ ). It is confirmed in all figures that analytical results are perfectly matched with M-C simulations<sup>14</sup>.

Fig. 5.2 shows the outage probability versus  $\gamma_0$  with  $\gamma_{th} = 0$  dB at terminal  $T_2$  when the turbulence channels are i.i.d (Fig. 5.2(a)) and i.n.i.d (Fig. 5.2(b)). There are three important observations which can be drawn from Fig. 5.2. *Firstly*, it is observed that the outage performance improves as the values of the parameters  $\xi_1$  and  $\xi_2$  increase in all cases of turbulence conditions. This is due to the fact that the parameter  $\xi_i$  ( $i \in \{1, 2\}$ ) has an inversely proportional relation with the pointing error displacement standard deviation. *Secondly*, as the effect of the atmospheric turbulence decreases, the outage performance improves. It is noted that  $\rho_1 = \rho_2 = 1$  (then  $\tau_1 = \tau_2 = 0$ ,  $\Omega'_1 = \Omega'_2 = 1$ ) corresponds to the special case of *Gamma-Gamma distribution* and the turbulence intensity also reduces as the parameter  $\xi_i$  increases [119]. *Finally*, the outage performance of the considered i.n.i.d case is better than that of the i.i.d case. For instance, under weak turbulence condition, the performance

<sup>14</sup>In Matlab, a  $\mathcal{M}$  turbulent channel random variable can be generated via squaring the absolute value of a Rician-shadowed random variable [119].



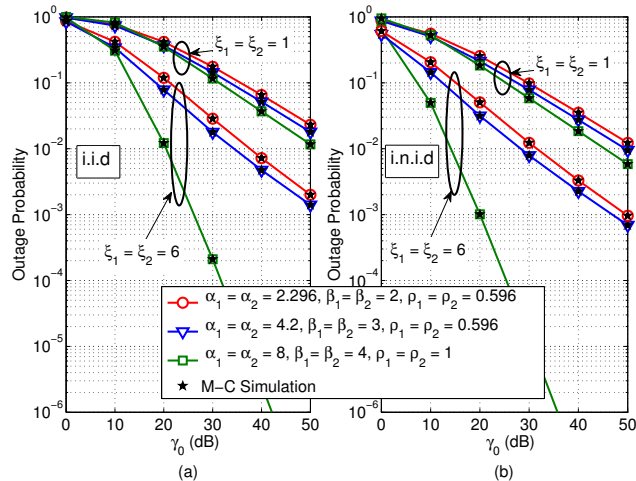


**Figure 5.2:** Outage probability for the two-way AF relaying FSO system at terminal  $T_2$  under different turbulence and pointing errors conditions.

improvement at the outage probability of  $10^{-6}$  is about 6 dB.

In Fig. 5.3, the ABER of the considered system is investigated under the impact of i.n.i.d moderate turbulence channels. Fig. 5.3(a) shows the ABER performance of  $M$ -PSK constellation (Fig. 5.3(a)) and  $M$ -QAM constellation (Fig. 5.3(b)) with respect to  $\gamma_0$  in two cases of severe pointing errors ( $\xi_1 = \xi_2 = 1$ ) and no pointing errors ( $\xi_1 \rightarrow \infty, \xi_2 \rightarrow \infty$ ). It is generally deduced from Fig. 5.3 that the ABER performance cannot reach  $10^{-3}$  even when operating at high average transmit SNR (e.g.,  $\gamma_0 = 50$  dB) due to the adverse effect of pointing errors. On the other hand, when the effect of pointing errors is mitigated, the error performance is significantly improved. It can also be observed that for a given turbulence strength and pointing error severity, the higher order of modulation will result in a worse error performance of the system.

Finally, Fig. 5.4 illustrates the ergodic achievable-rate of the two-way AF relaying FSO system with respect to  $\gamma_0$  under the combined effect of atmospheric turbulence and pointing errors in two cases of i.i.d (Fig. 5.4(a)) and i.n.i.d (Fig. 5.4(b)) channels. As expected, the ergodic achievable-rate is increased when the atmospheric turbulence strength is reduced. It is also observed that the pointing errors exert a considerable effect on the achievable-rate. For example, when the pointing errors severity reduces (e.g., from  $\xi = 1$  to  $\xi = 6$ ) and with  $\alpha_1 = \alpha_2 = 2.296$ ,  $\beta_1 = \beta_2 = 2$ , a

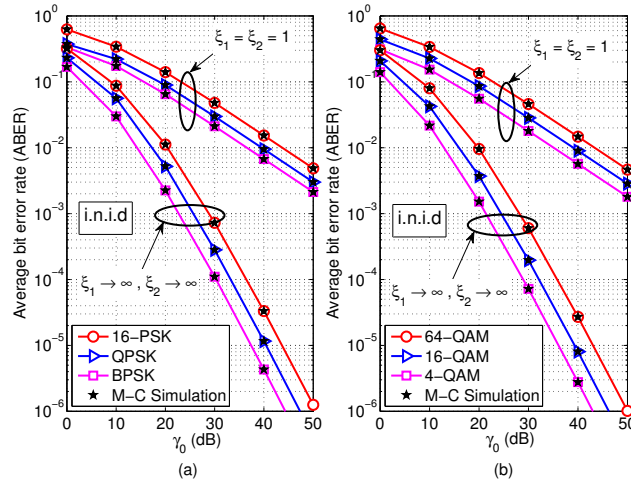


**Figure 5.3:** ABER for the two-way AF relaying FSO system at terminal  $T_2$  with  $\alpha_1 = \alpha_2 = 4.2$ ,  $\beta_1 = \beta_2 = 3$ ,  $\rho_1 = \rho_2 = 1$ .

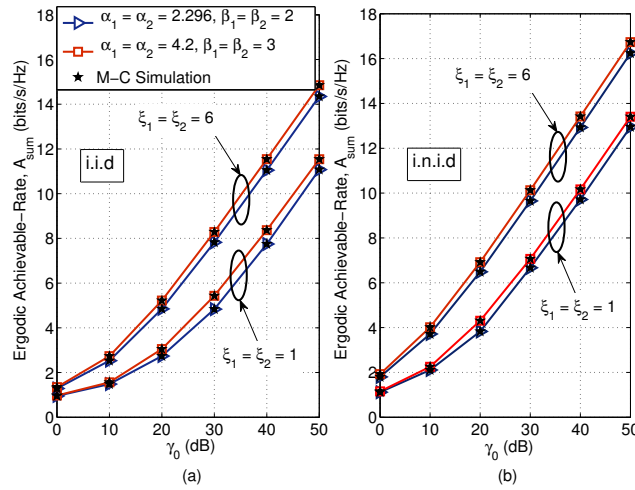


**Figure 5.4:** Ergodic achievable-rate for the two-way AF relaying FSO system with varying atmospheric turbulence strength and pointing errors severity,  $\rho_1 = \rho_2 = 0.596$ .

SNR gain of 10 dB can be achieved at the ergodic achievable-rate of 11 (bits/s/Hz) and 13 (bits/s/Hz) for i.i.d and i.n.i.d cases, respectively.

## 5.6. Conclusions

This paper analyzed the performance of two-way all-optical AF relaying FSO systems over i.n.i.d  $\mathcal{M}$  distributed atmospheric turbulence-induced fading channels with pointing errors. Novel exact closed-form expressions for the MGF and CDF of the end-to-end SNR were presented in terms of extended generalized bivariate

Meijer's G-functions. Utilizing these results, we analyzed the end-to-end performance of the proposed FSO system in terms of outage probability, average bit error rate, and ergodic achievable-rate. Monte-Carlo simulations were performed to confirm the validity of the theoretical analysis.

# Chapter 6

## Multihop Relaying WDM/FSO Systems

### 6.1. Introduction

Free-space optics (FSO) has recently received much attention in the first-mile access environment owing to a number of advantages over radio-frequency communications, including much higher bandwidth with license-free spectrum, better energy efficiency and possibly higher security. Compared to fiber optical communications, FSO also offers fiber-like data rate while being more flexible and cost-effective, as well as quicker and easier for deployment and re-deployment [157]. Currently, wavelength division multiplexed (WDM) transmission, which allows to carry many separate and independent optical channels, can support Terabits per second capacities, and it can be easily integrated into FSO systems to considerably increase the bit rate [158]. This WDM/FSO combination is therefore a promising solution to meet the unprecedented growth in the global demand for broadband applications and services [159, 160]. In this paper, we propose a novel concept of all-optical access networks using multi-hop WDM/FSO to provide high-bandwidth connections for multiple users in an extended coverage. System performance is comprehensively analyzed taking into account crucial physical-layer impairments, including atmospheric attenuation, turbulence, inter-

channel crosstalk, and pulse broadening.

### 6.1.1. Related Studies and Motivations

Several WDM/FSO systems have been successfully demonstrated [158, 161]. WDM-Passive Optical Network (PON) using FSO in the distribution links to support multiple users at high bit rates is an appealing proposal [162–164]. In this hybrid WDM-PON/FSO network, the WDM channels suffer from interchannel crosstalk, while the FSO channels are affected by atmospherically induced scintillation, i.e., atmospheric turbulence. The combination of these two impairments results in turbulence-accentuated crosstalk effect, which severely degrades the overall system performance, particularly in the upstream transmission [163]. Practically, FSO could be an extension of optical fiber since both links share the identical transmission wavelengths and system components. Especially, using a pair of FSO terminals (FSOT), which can be transparently connected to single-mode fiber lines, FSO systems can be fully compatible with optical fiber networks [165].

FSO nevertheless is confined to short-haul applications since its reliability is degraded due to the distance-dependent atmospheric turbulence-induced fading and loss [133]. To extend the coverage of FSO systems, relaying FSO has been considered as a suitable solution [134, 146, 166–170]. Many previous studies mainly focused on electrical relaying, where all signal processes are implemented in the electrical domain [134, 166, 167]. This technique is daunting from an implementation perspective for Gigabit per second (Gbps)-rate FSO links since it requires complex optoelectronics and decoding/encoding hardware. Therefore, the all-optical relaying technique, i.e., optical amplify-and-forward (OAF), where the signal processing is only performed in the optical domain so that the full bandwidth of an optical signal can be used, has been recently studied [117, 146, 168, 169]. It is generally deduced from these studies that OAF relaying is faster and simpler to implement and achieves a better performance than electrical relaying unless the number of relays is large, in which case the accumulation of background and amplified spontaneous emission (ASE) noises

impose a negative impact on the system performance.

On the other hand, the signal dispersion (pulse broadening) is another important factor in FSO system performance. In recent studies, the Gaussian pulse propagation model was employed so that both atmospheric turbulence and pulse broadening could be investigated in the performance of FSO systems [171, 172]. However, the pulse broadening issue has not been clarified in WDM/FSO systems.

### 6.1.2. Main Contributions

The main contributions in this paper can be summarized as follows.

First, we propose a novel concept of all-optical access networks using multi-hop WDM/FSO to provide high-bandwidth connections for multiple users. This proposition takes advantage of both the all-optical relaying technique and the WDM transmission, hence resulting in a low cost, reliable, flexible, and high-speed access network. This proposed network can be compatibly combined with the pre-deployed fiber network to further increase the network coverage. Therefore, it could be a realistic solution for the first-mile ‘bottleneck’ problem, especially when fiber installation is not favorable.

Secondly, we employ the  $M$ -ary pulse position modulation ( $M$ -PPM) combined with the OAF relaying technique to combat against the turbulence-accentuated interchannel crosstalk effect, which is the main impairment in WDM/FSO systems. In previous studies,  $M$ -PPM has been employed as an energy-efficient transmission method [173–175]. Additionally, the use of PPM also avoids adaptive threshold adjustments required in on-off keying (OOK) [176].

Thirdly, for performance analysis, we take into account effects of all noises and atmospheric impairments, including turbulence and pulse broadening. The atmospheric turbulence is modeled by a Gamma-Gamma channel, which is suitable for a wide range of turbulence conditions [99], while the pulse broadening is characterized by the Gaussian pulse propagation model. Our numerical results, which are validated by Monte-Carlo (M-C) simulations, show that the proposed WDM/FSO system using

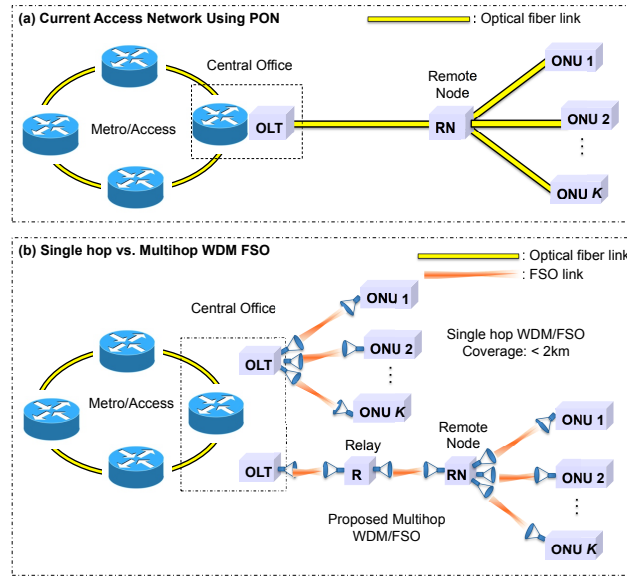


**Figure 6.1:** (a) PON optical fiber access network; (b) Proposed all-optical multi-hop WDM/FSO access network.

PPM combined with OAF relaying technique is a feasible solution for optical access networks.

## 6.2. Proposed System Descriptions

### 6.2.1. Network Model

Fig. 6.1(a) shows the model of a typical PON using optical fiber links, which consists of optical network units (ONUs), a passive splitter at the remote node (RN), and an optical line terminal (OLT). Typically, PON can reach the distance of up to 20 km, and it is capable of delivering upstream to 1.2 Gbps and 2.4 Gbps downstream to the port with current standards [177]. As the next step in fiber access evolution, the ITU-T is defining the second next generation PON (NG-PON2), which is primarily based on time and wavelength division multiplexing (TWDM) since it is most compatible with the high volume residential application. The NG-PON2 could offer 40 Gbps aggregate downstream capacity and 10 Gbps upstream [178]. Nevertheless, it is not always economical or possible to have optical fiber installation due to the high cost, especially in vast, low-density remote areas, difficult terrains, the limitation of running additional cables (such as city centers, historical areas), or the need

of temporary connection only. A solution for these issues is to use FSO instead of the optical fiber [163,164]. As shown in the upper part of Fig. 6.1(b), FSO is combined with WDM/PON to form a hybrid optical access network with lower cost and higher flexibility. The coverage of single-hop FSO links in the distribution network is however limited (to about 2 kilometers) due to the negative impacts of atmospheric and weather conditions [163].

To address above-mentioned issues, we propose a cost-effective, flexible, and reliable network model using multi-hop WDM/FSO, as shown in the lower part of Fig. 6.1(b). For the extended distance from the OLT to the RN, multi-hop WDM/FSO relaying with erbium-doped fiber amplifiers (EDFAs) is employed. In this WDM/FSO network, FSO links can be configured in different topologies, such as point-to-point, point-to-multipoint, ring, or mesh connections. The cost of deploying WDM/FSO network can be significantly lower than that of conventional PONs because no fibers are required between the OLT and service areas, leading to a substantial reduction of fiber installation and maintenance expenses. Besides, the WDM/FSO systems can be fully compatible with the terrestrial fiber communication in metro networks, which provide not only the multi-gigabit link capacity but also the link stability and reliability [165]. Moreover, based on full-optical FSO systems, advanced Radio over FSO (RoFSO) systems have also been developed with the capability of transferring multiple wireless signals using WDM/FSO channels [179]. Above-mentioned advantages make our proposed multi-hop WDM/FSO system become a promising solution for all-optical access networks.

### 6.2.2. System Model

For performance analysis purpose, we use a model of multi-hop OAF relaying WDM/FSO access network shown in Fig. 6.2. For both downstream and upstream directions, the OLT communicates with ONUs through  $N$  intermediate relays ( $R_i$ ,  $i = 1, 2, \dots, N$ ), including the RN. The total transmission distance is  $L = \sum_{i=1}^{N+1} d_i$ , where  $d_i$  is the transmission distance from the  $(i - 1)$ -th node to the  $i$ -th node (with



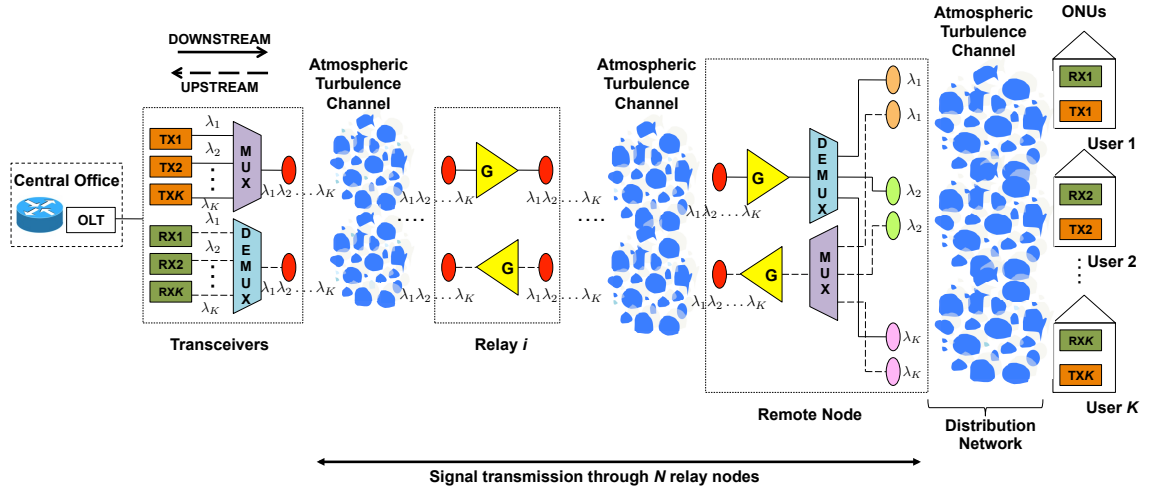


**Figure 6.2:** Multi-hop OAF relaying WDM/FSO systems for optical access networks.

node 0 is the OLT and node  $N + 1$  is the ONU).

In the downstream transmission, signals from  $K$  transmitters, each with a unique wavelength  $(\lambda_1, \lambda_2, \dots, \lambda_K)$  are combined by a WDM mux and then transmitted via multi-hop FSO channels to the RN. The optical wavelengths are chosen in the C band (i.e., around 1550 nm) with channel spacing of 100 GHz, since 1550 nm light suffers from less atmospheric attenuation and it is suitable for EDFA technology and high quality transceivers [180]. At each relay node, an optical amplifier (EDFA) is used to directly amplify the optical signals. A single EDFA can simultaneously amplify many data channels at different wavelengths within the gain region. However, the advantage of an optical amplifier comes at the cost of introducing ASE noise, which somewhat offsets the performance gain. After that, at the RN, WDM demux separates the multiplexed optical signals into constituent wavelengths. Due to the defectiveness of the demux and transmitting lenses at the RN, the end-user may receive the optical signal of undesired wavelengths, i.e., interferers. This phenomenon is also known as interchannel crosstalk, which was previously studied in [180, 181]. There also exists several losses of mux/demux, which comprise the signal mux, demux losses (denoted as  $L_{mx}$ ,  $L_{dx}$ , respectively), and  $L_{dx,XT}$ , which indicates the crosstalk level from the interferer at the demux. Finally, in the distribution network, signals with constituent wavelengths are delivered to the corresponding end-users (ONUs)

in a point-to-point scheme. At each receiver, PIN photodiode is used to convert the electrical field into the photocurrent.

In the upstream direction, interchannel crosstalk arises due to the imperfection of the demux at the OLT when separating different wavelengths to corresponding receivers. However, the interchannel crosstalk effect in this situation becomes more severe, since the atmospheric turbulence in the distribution network results in a fluctuating crosstalk effect. It is also called as the turbulence-accentuated interchannel crosstalk, which arises when the signal and crosstalk paths are independently turbulent, i.e., physically totally distinct, as in the case of the upstream. The effect of turbulence-accentuated interchannel crosstalk in WDM-PON integrated with FSO networks was investigated in [163]. It is also worthy to note that there may exist intrachannel crosstalk in the upstream transmission if a portion of the transmitted power falls in the field of view of an unexpected receiving lens due to the beam spreading effect. Nevertheless, intrachannel crosstalk can be neglected, since we can generally arrange the position of ONUs to avoid the near identical transmission paths.

For each wavelength,  $M$ -ary PPM scheme is employed. At the transmitter, input data is first modulated at a PPM modulator, where each block of  $b$  bits is mapped to one of  $M$  possible symbols  $(s_0, s_1, \dots, s_M)$ , where  $M = 2^b$ . The symbol interval,  $T_w$ , is divided into  $M$  time-disjoint time slots and an electrical pulse is sent in one of these  $M$  time slots while remaining  $(M - 1)$  time slots are empty. This pulse is then converted into an optical pulse with constant power of  $P_{t,sig}$  by a laser diode. Denoting  $R_b$  as the bit rate of the system, the symbol interval has a duration given by  $T_w = \frac{b}{R_b} = \frac{\log_2 M}{R_b}$ , and time slots have the duration of  $T_s = \frac{T_w}{M}$ .

At the input of each relay, optical signals include not only data signal but also background noise and interferer signal with the average powers of  $P_b$  and  $P_{t,int}$ , respectively. Here, the case of a single interferer is assumed. These signals are amplified by an EDFA with the fixed gain  $G$ , which is set to keep the average relay output power constant at  $P_{t,sig}$  [146], [168]. The signals are then transmitted to the next relay together with ASE noise, which can be described by additive zero-mean

white Gaussian model with the optical power given by  $P_A = h_P f (G - 1) n_{sp} B_0$ , where  $h_P$  is the Planck's constant,  $f$  is the frequency,  $n_{sp}$  is the amplifier spontaneous emission parameter, and  $B_0$  is the optical bandwidth [182]. Over multiple relays, background and ASE noises are amplified and accumulated.

At the destination, the received signal, including the background noise at the receiver, is converted into the photocurrent by a PIN photodetector. Next, integrated photocurrents over  $M$  time slots are compared at the PPM demodulator to find the position of the slot with the highest current, which determines the transmitted symbol. Finally, detected symbol is converted to the binary data by a symbol-to-bit converter.

### 6.3. FSO Dispersive Turbulence Channel Model

This section presents the mathematical model of FSO channel with  $h_i$ , ( $i = 1, 2, \dots, N + 1$ ), which is the channel state modeling the random attenuation of the propagation channel between the  $(i - 1)$ -th node and the  $i$ -th node. In the proposed system, each hop is assumed to be equidistant (i.e.,  $d_1 = \dots = d_i = \dots = d_{N+1} = \frac{L}{N+1}$ ), and the channel state between every pair of relays is considered to be independent and identically distributed. In our model,  $h_i$  arises due to two factors: channel loss ( $h_i^l$ ) including the geometric spreading of the optical beam, atmospheric attenuation, and pulse broadening; and atmospheric turbulence ( $h_i^a$ ). The channel coefficient hence can be described as  $h_i = h_i^l h_i^a$ .

#### 6.3.1. Atmospheric Dispersive Model

To evaluate time-domain spreading of a pulse wave propagating through atmospheric turbulence, we assume that the transmitted waveform in each PPM time slot is a Gaussian pulse. The amplitude of the Gaussian pulse is described by

$$U_t(t) = \sqrt{P_0} \exp\left(-\frac{t^2}{T_0^2}\right), \quad (6.1)$$

where  $P_0$  and  $T_0$  are the average power and the half-width (at the  $1/e$  point) of the input pulse, respectively [183]. The relation between the average power of Gaussian pulse ( $P_0$ ) and the average power per time slot ( $P_{t,sig}$ ) is given by

$$P_0 = \frac{\sqrt{2}T_s}{\sqrt{\pi}T_0} P_{t,sig}, \quad (6.2)$$

where  $T_s$  is the duration of the time slot [171].

Over a transmission distance  $d_i$ , the received optical signal is attenuated by the propagation loss including the geometrical spreading of the optical beam and atmospheric attenuation. It is easy to obtain the value of loss due to geometric spreading as a function of the area of the receiver aperture  $A$  and the angle of divergence  $\theta$ . On the other hand, the atmospheric attenuation can be described by the exponential Beer-Lambert's law. As a result, the total of atmospheric attenuation and geometric spreading can be formulated as

$$a_{att} = \frac{A}{\pi \left(\frac{\theta}{2}d_i\right)^2} \exp(-a_l d_i), \quad (6.3)$$

where  $A = \pi(a)^2$  with  $a$  is the radius of the receiver aperture, and  $a_l$  is the atmospheric attenuation coefficient. In addition, the optical pulse obtained at the receiver is broadened due to the atmospheric turbulence, and its average power is reduced. Therefore, the received signal at the distance of  $d_i$  meters from the transmitter, taking into consideration the effects of geometrical spreading of the optical beam, atmospheric attenuation, and pulse broadening, can be mathematically expressed as [171]

$$U_r(t) = \sqrt{P_0 a_{att}} \frac{T_0}{\sqrt{T_0^2 + 8\delta}} \exp\left(-\frac{t^2}{T_0^2 + 8\delta}\right). \quad (6.4)$$

The parameter  $\delta$ , which governs the scale of pulse broadening and average power reduction, is given by  $\delta = \frac{0.3908 C_n^2 d_i L_0^{5/3}}{c^2}$ , where  $C_n^2$  stands for the altitude-dependent index of the refractive structure parameter, and  $L_0$  is the outer scale of turbulence, and  $c$  is the light velocity [183].

As pulse is spread out of the time slot owing to pulse broadening, the average power per PPM time slot at the receiver ( $P_r$ ) is reduced compared to  $P_{t,sig}$ . Therefore, the power loss coefficient caused by atmospheric attenuation and pulse broadening can be determined by

$$h_i^l = \frac{P_r}{P_{t,sig}} = \frac{1}{P_{t,sig}T_s} \int_{-T_s/2}^{T_s/2} |U_r(t)|^2 dt. \quad (6.5)$$

### 6.3.2. Atmospheric Turbulence Model

An optical wave propagating through the atmosphere will experience irradiance (i.e., intensity) fluctuations, or scintillation. Scintillation is caused by the inhomogeneities in the temperature and pressure of the atmosphere leading to refractive index variations (i.e., atmospheric turbulence). To characterize the whole range of atmospheric turbulence effects (i.e., weak, moderate, and strong), Gamma-Gamma (G-G) distribution has been found to be a suitable choice since it is able to model both small-scale and large-scale fluctuations [99]. The G-G probability density function (pdf) of  $h_i^a > 0$  is given as

$$f_{h_i^a}(h_i^a) = \frac{2(\alpha\beta)^{(\alpha+\beta)/2}}{\Gamma(\alpha)\Gamma(\beta)} (h_i^a)^{\frac{\alpha+\beta}{2}-1} \times K_{\alpha-\beta} \left( 2\sqrt{\alpha\beta h_i^a} \right), \quad (6.6)$$

where  $\Gamma(\cdot)$  denotes Gamma function defined as  $\Gamma(w) \triangleq \int_0^\infty t^{w-1} e^{-t} dt$ ,  $K_{\alpha-\beta}(\cdot)$  is the modified Bessel function of the second kind of order  $(\alpha - \beta)$ ,  $\alpha > 0$  and  $\beta > 0$  are the effective numbers of small-scale and large-scale eddies of scattering environment, respectively. Assuming a plane wave propagation of the optical beam,  $\alpha$  and  $\beta$  are given as

$$\alpha \cong \left[ \exp \left( \frac{0.49\sigma_R^2}{(1 + 1.11\sigma_R^{12/5})^{7/6}} \right) - 1 \right]^{-1}, \quad (6.7)$$

$$\beta \cong \left[ \exp \left( \frac{0.51\sigma_R^2}{(1 + 0.69\sigma_R^{12/5})^{5/6}} \right) - 1 \right]^{-1}, \quad (6.8)$$

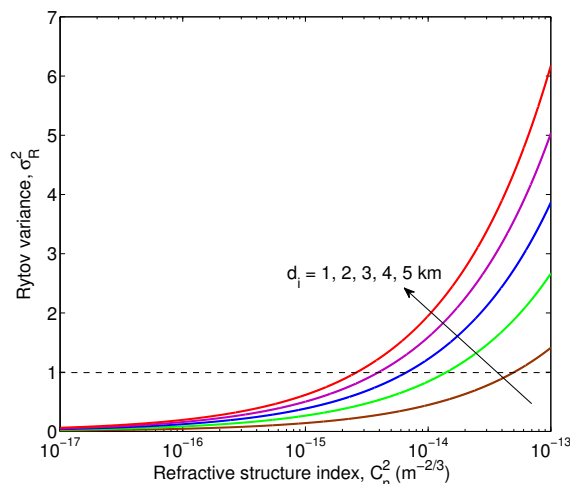


**Figure 6.3:** Rytov variance versus the refractive structure index for different transmission distances.

where  $\sigma_R^2$  is the Rytov variance which is defined as

$$\sigma_R^2 \triangleq 1.23 \left( \frac{2\pi}{\lambda} \right)^{7/6} C_n^2 d_i^{11/6}, \quad (6.9)$$

with  $\lambda$  is the optical wavelength [99]. In general,  $C_n^2$  varies from  $10^{-13} m^{-2/3}$  to  $10^{-17} m^{-2/3}$  [184], and a table reporting  $C_n^2$  for different weather conditions can be found in [185]. Illustratively, Fig. 6.3 shows the Rytov variance  $\sigma_R^2$  versus  $C_n^2$  for different transmission distances. Typically, weak, moderate, and strong turbulence conditions respectively correspond to  $\sigma_R^2 < 1$ ,  $\sigma_R^2 \approx 1$ , and  $\sigma_R^2 > 1$ . The saturation regime is defined by  $\sigma_R^2 \rightarrow \infty$  [199].

## 6.4. Bit-Error Rate Analysis

Once the PPM symbol is detected, it is mapped to a string of  $\log_2(M)$  bits via the inverse of the encoding mapping. There are  $M/2$  symbol errors that will produce an error in a given bit in the string, and there are  $(M - 1)$  unique symbol errors. Thus, assuming all symbol errors are equally likely, and denoting  $P_e$  as the symbol error probability (SEP), the bit error rate (BER) of the system then can be derived as

$$\text{BER} = \frac{M}{2(M - 1)} P_e. \quad (6.10)$$

We assume that the transmitted data is large enough that the probabilities of sending any symbols are the same. At the receiver, the photocurrent  $I_u$  corresponds to the  $u$ -th slot ( $0 \leq u \leq M - 1$ ) of the received symbol. Without the loss of generality, we assume that symbol  $s_0$  is transmitted, i.e.,  $I_0$  is the signal current corresponding to the signal slot (slot 0).

In the downstream direction, the signal and interferer can be assumed to experience the same atmospheric turbulence as the crosstalk arises before the distribution link (i.e.,  $(N + 1)$ -th hop). The downstream interchannel crosstalk is not turbulence-accentuated since it traverses the same atmospheric path as the signal (neglecting slight wavelength difference impact on  $\sigma_R^2$ ). Hence, the G-G pdfs for both signal and interferer can be considered to be the same. Applying the union bound, the SEP for the downstream transmission can be expressed as

$$\begin{aligned}
 P_e &\leq 1 - \Pr\{I_0 > I_u | u \in \{1, \dots, M - 1\}, s = s_0\} \\
 &\leq (M - 1) \Pr\{I_0 \leq I_u | u \in \{1, \dots, M - 1\}, s = s_0\} \\
 &\leq \frac{M-1}{2} \int_0^\infty dh_1^a \cdots \int_0^\infty dh_i^a \cdots \int_0^\infty dh_{N+1}^a \\
 &\quad f_{h_1^a}(h_1^a) \cdots f_{h_i^a}(h_i^a) \cdots f_{h_{N+1}^a}(h_{N+1}^a) \operatorname{erfc}\left(\sqrt{\frac{\text{SNR}}{2}}\right). \tag{6.11}
 \end{aligned}$$

In the upstream direction, the signal and interferer first travel over physically distinct paths in the  $(N + 1)$ -th hop (from ONUs to the RN). Therefore, their G-G distributions can be assumed to be independent. In our analysis, the channel states of the  $(N + 1)$ -th hop for signal and interferer are denoted as  $h_{N+1, \text{sig}} = h_{N+1, \text{sig}}^l h_{N+1, \text{sig}}^a$  and  $h_{N+1, \text{int}} = h_{N+1, \text{int}}^l h_{N+1, \text{int}}^a$ , respectively. Similarly, the upper bound of the SEP for the upstream transmission can be expressed as

$$\begin{aligned}
 P_e &\leq \frac{M-1}{2} \int_0^\infty dh_1^a \cdots \int_0^\infty dh_i^a \cdots \int_0^\infty dh_{N+1}^a \int_0^\infty dh_{N+1, \text{int}}^a \\
 &\quad f_{h_1^a}(h_1^a) \cdots f_{h_i^a}(h_i^a) \cdots f_{h_{N+1, \text{sig}}^a}(h_{N+1, \text{sig}}^a) \\
 &\quad \times f_{h_{N+1, \text{int}}^a}(h_{N+1, \text{int}}^a) \operatorname{erfc}\left(\sqrt{\frac{\text{SNR}}{2}}\right). \tag{6.12}
 \end{aligned}$$

In (6.11) and (6.12),  $\Pr\{\cdot\}$  denotes the probability of the given event,  $s$  represents the transmitted symbol and  $\text{erfc}(z) \triangleq \frac{2}{\sqrt{\pi}} \int_z^\infty e^{-t^2} dt$  is the complementary error function. Following (6.6),  $f_{h_i^a}(h_i^a)$  is the G-G pdf of  $h_i^a$  of the  $i$ -th hop for the signal ( $i = 1, 2, \dots, N + 1$ ), and  $f_{h_{N+1,int}^a}(h_{N+1,int}^a)$  is the G-G pdf of  $h_{N+1,int}^a$  of the  $(N + 1)$ -th hop for the interferer. SNR is the electrical signal to noise ratio in case of PPM signaling, which is defined as

$$\text{SNR} = \frac{(\mu_0 - \mu_u)^2}{\sigma_0^2 + \sigma_u^2}. \quad (6.13)$$

In (6.13),  $\sigma_0^2$  and  $\sigma_u^2$  are receiver noise variances of signal currents in 0 and  $u$  slots, which can be expressed as

$$\begin{bmatrix} \sigma_0^2 \\ \sigma_u^2 \end{bmatrix} = \begin{bmatrix} \sigma_{sig}^2 + \sigma_{int}^2 + \sigma_{b,r}^2 + \sigma_{ASE,r}^2 + \sigma_{b,d}^2 + \sigma_{ASE,d}^2 + \sigma_T^2 \\ \sigma_{int}^2 + \sigma_{b,r}^2 + \sigma_{ASE,r}^2 + \sigma_{b,d}^2 + \sigma_{ASE,d}^2 + \sigma_T^2 \end{bmatrix}, \quad (6.14)$$

where  $\sigma_{sig}^2$ ,  $\sigma_{int}^2$ ,  $\sigma_{b,r}^2$ ,  $\sigma_{ASE,r}^2$ ,  $\sigma_{b,d}^2$ ,  $\sigma_{ASE,d}^2$ , and  $\sigma_T^2$  are variances of signal shot noise, interferer shot noise, accumulated amplified background noise over multiple relays, accumulated amplified ASE noise over multiple relays, background noise at the destination, ASE noise resulted from the amplifier at the RN received at the destination, and receiver thermal noise, respectively.  $\mu_0 = I_{sig} + I_{int}$  and  $\mu_u = I_{int}$  are respectively the mean values of signal currents in 0 and  $u$  slots, in which  $I_{sig}$  and  $I_{int}$  are the signal and interferer currents.

Since the atmospheric turbulence in the  $(N + 1)$ -th hop is treated similarly in the downstream direction and independently in the upstream direction for the signal and interferer, the calculation of signal and interferer currents as well as receiver noise variances is derived differently.



### 6.4.1. Downstream Analysis

For the downstream transmission,  $I_{sig}$  and  $I_{int}$  can be expressed as

$$\begin{bmatrix} I_{sig} \\ I_{int} \end{bmatrix} = \begin{bmatrix} \Re P_{t,sig} \left( \prod_{i=1}^N G_i h_i^l h_i^a \right) h_{N+1}^l h_{N+1}^a L_{mx} L_{dx} \\ \Re P_{t,int} \left( \prod_{i=1}^N G_i h_i^l h_i^a \right) h_{N+1}^l h_{N+1}^a L_{mx} L_{dx} L_{dx,XT} \end{bmatrix}, \quad (6.15)$$

where  $\Re$  is the responsivity of the PIN photodiode,  $G_i$  is the optical amplifier fixed-gain at the  $i$ -th relay (assuming that  $G_1 = \dots = G_i = \dots = G_N$ ). In (6.14), the variances of receiver noises can be expressed as

$$\sigma_{sig}^2 = 2q \Re P_{t,sig} \left( \prod_{i=1}^N G_i h_i^l h_i^a \right) h_{N+1}^l h_{N+1}^a L_{mx} L_{dx} B_e, \quad (6.16)$$

$$\sigma_{int}^2 = 2q \Re P_{t,int} \left( \prod_{i=1}^N G_i h_i^l h_i^a \right) h_{N+1}^l h_{N+1}^a L_{mx} L_{dx} L_{dx,XT} B_e, \quad (6.17)$$

$$\sigma_{b,r}^2 = 2q \Re P_b \left( \sum_{i=1}^N \prod_{k=i}^N G_k h_{k+1}^l h_{k+1}^a \right) L_{dx} B_e, \quad (6.18)$$

$$\sigma_{ASE,r}^2 = 2q \Re \left( \sum_{i=1}^{N-1} \prod_{k=i+1}^N G_k h_k^l h_k^a h_{N+1}^l h_{N+1}^a P_A^i \right) L_{dx} B_e, \quad (6.19)$$

$$\sigma_{ASE,d}^2 = 2q \Re P_A^{N+1} h_{N+1}^l h_{N+1}^a L_{dx} B_e, \quad (6.20)$$

$$\sigma_{b,d}^2 = 2q \Re P_b B_e, \quad (6.21)$$

$$\sigma_T^2 = \frac{4k_B T}{R_L} B_e, \quad (6.22)$$

where  $q$  is the electron charge;  $k_B$  is the Boltzmann's constant;  $T$  is the absolute temperature;  $R_L$  is the load resistance;  $B_e$  is the effective noise bandwidth defined as  $B_e = \frac{1}{T_s} = \frac{MR_b}{\log_2(M)}$ ;  $P_A^i$  is the average power of ASE noise at the  $i$ -th relay, assuming that  $P_A^1 = \dots = P_A^i = \dots = P_A^N$ .

### 6.4.2. Upstream Analysis

By substituting  $h_{N+1,sig}^l h_{N+1,sig}^a$  and  $h_{N+1,int}^l h_{N+1,int}^a$  for  $h_{N+1}^l h_{N+1}^a$  from (6.15) to (6.17), we respectively obtain  $I_{sig}$ ,  $I_{int}$ , and  $\sigma_{sig}^2$ ,  $\sigma_{int}^2$  for the upstream transmission. To obtain  $\sigma_{ASE,d}^2$ ,  $h_{N+1}^l h_{N+1}^a$  in (6.20) is replaced by  $h_1 = h_1^l h_1^a$  because this ASE noise

experiences turbulence from the first hop when considering the direction from ONUs to the OLT. For  $\sigma_{b,r}^2$ ,  $\sigma_{ASE,r}^2$ ,  $\sigma_{b,d}^2$ , and  $\sigma_T^2$ , the calculation is the same as in (6.18), (6.19), (6.21), and (6.22), respectively.

## 6.5. Numerical Results

In this section, we numerically investigate the BER of the proposed system under the assumption of a single interferer for both downstream and upstream transmissions. The derivation of closed-form expression for BER is relatively complex when all noises (including signal dependent ones) and interference are considered. In some special cases, when noise is assumed as signal independent Gaussian, the closed-form expression for BER can be derived [134], [166]. In this study, we base on exact-form upper bound expressions shown in (6.11) and (6.12) to investigate the BER for both cases of the upstream and the downstream. M-C simulations are also performed to validate the tight upper bound analysis.

It is noted that, for a fair comparison, the performance of the proposed system is examined under a constraint on the average power per information bit; that means, the average transmitted power of the PPM symbol,  $P_{t,sig}$  can be given by  $P_{t,sig} = (M \log_2 M)P_s$  with  $P_s$  is the average transmitted power per information bit. The required  $P_s$  here is considered for achieving the BER of  $10^{-6}$  so that the operational performance (when  $BER = 10^{-9}$ ) can be achieved when forward error correction (FEC) is applied. For the downstream transmission, the signal and interferer are assumed to have the same launch average power ( $P_{t,sig} = P_{t,int}$ ) and distance to RN. On the contrary, in the upstream transmission, we also assume  $P_{t,sig} = P_{t,int}$  but the distances to RN from the signal and interferer are separately examined. The system parameters and constants used in the analysis are shown in Table 6.1.

### 6.5.1. Downstream Transmission

First, Fig. 6.4(a) and Fig. 6.4(b) show BER versus  $P_s$  for the downstream transmission in cases of OOK and 4-PPM with different numbers of relays  $N$  within a fixed

**Table 6.1:** System Parameters and Constants.

Name	Symbol	Value
Boltzmann's constant	$k_B$	$1.38 \times 10^{-23}$ W/K/Hz
Planck's constant	$h_P$	$6.626 \times 10^{-34}$
Electron charge	$q$	$1.6 \times 10^{-19}$ C
Optical bandwidth	$B_0$	125 GHz
Load resistor	$R_L$	50 $\Omega$
Receiver temperature	$T$	300 K
PD responsivity	$\mathfrak{R}$	1 A/W
ASE parameter	$n_{sp}$	5
Attenuation coefficient	$a_l$	0.1 dB/km
Receiver radius	$a$	10 cm
Divergence angle	$\theta$	1 mrad
Background power	$P_b$	-40 dBm
Wavelength	$\lambda$	1550 nm
Mux loss	$L_{mx}$	-3.5 dB
Demux loss	$L_{dx}$	-3.5 dB

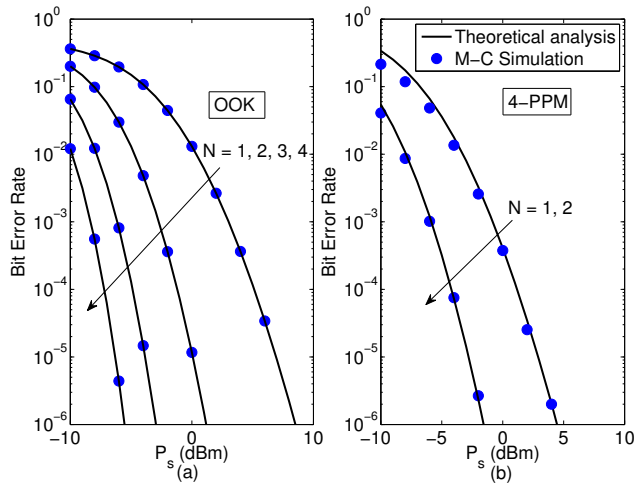


**Figure 6.4:** Downstream transmission: BER versus the average transmitted power per information bit  $P_s$ , with  $R_b = 1$  Gbps,  $L_{dx,XT} = -30$  dB,  $L = 4$  km, and  $C_n^2 = 5 \times 10^{-15}$  for different numbers of relays  $N$  in systems using OOK (a) and 4-PPM (b).

distance of 4 km. It is confirmed that the system performance could be significantly improved by increasing  $N$ . In Fig. 6.4(a) for systems using OOK, when  $N$  increases from 1 to 2 relays, 2 to 3 relays, and 3 to 4 relays, the performance improvements are 7 dB, 4 dB, and 2.5 dB, respectively. The decrease of the performance improvements is due to the accumulation of amplified background and ASE noises over multiple relays. On the other hand, in Fig. 6.4(b) for systems using 4-PPM, it is observed that

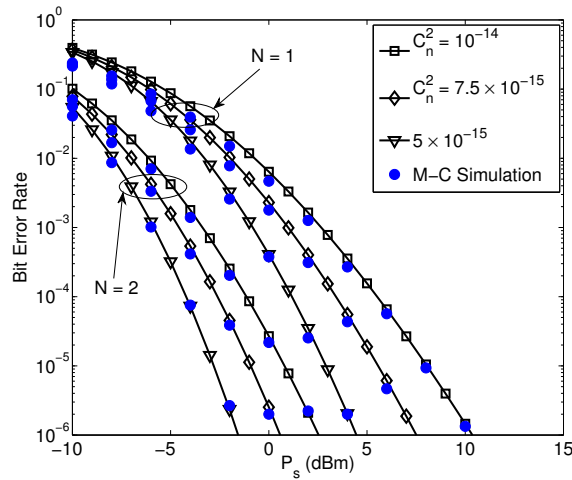


**Figure 6.5:** Downstream transmission: BER versus the average transmitted power per information bit  $P_s$ , with 4-PPM,  $R_b = 1$  Gbps,  $L_{dx,XT} = -30$  dB, and  $L = 4$  km, for different turbulence strengths  $C_n^2$ .

PPM-based systems outperform OOK-based ones. Compared to OOK-based systems with the cases of  $N = 1$  and  $N = 2$ , PPM-based systems attain the performance improvements of 4 dB and 3 dB, respectively. Therefore, PPM combined with OAF relaying is a good solution to improve the system performance, avoiding the adaptive threshold required in optimum-performing OOK-modulated FSO systems.

Next, Fig. 6.5 illustrates BER of the proposed system using 4-PPM versus  $P_s$  for the downstream transmission with various turbulence strengths. Within the total distance of 4 km, the BER performance is constantly deteriorated when the turbulence becomes stronger (i.e., higher  $C_n^2$ ). With only one relay, the required  $P_s$  to attain BER of  $10^{-6}$  are 10.5 dBm, 7.5 dBm, and 4.5 dBm corresponding to  $C_n^2$  of  $10^{-14}$ ,  $7.5 \times 10^{-15}$ , and  $5 \times 10^{-15}$ . With two relays, the BER performance is significantly improved. More specifically, compared to the case when  $N = 1$ , the performance improvements when  $N = 2$  are 8 dB, 7 dB, and 6 dB for  $C_n^2$  of  $10^{-14}$ ,  $7.5 \times 10^{-15}$ , and  $5 \times 10^{-15}$ , respectively.

In Fig. 6.6, we investigate BER versus the total transmission distance for different numbers of relays (Fig. 6.6(a)) and orders of PPM scheme (Fig. 6.6(b)). In Fig. 6.6(a), the total transmission distance  $L$  could be further increased by increasing  $N$ . For instance, using 4-PPM, the maximum distances (calculated at BER =  $10^{-6}$ ) achieved with  $N = 1$ ,  $N = 3$ ,  $N = 5$ , and  $N = 7$  are 3 km, 5 km, 6.5 km, and 7.6

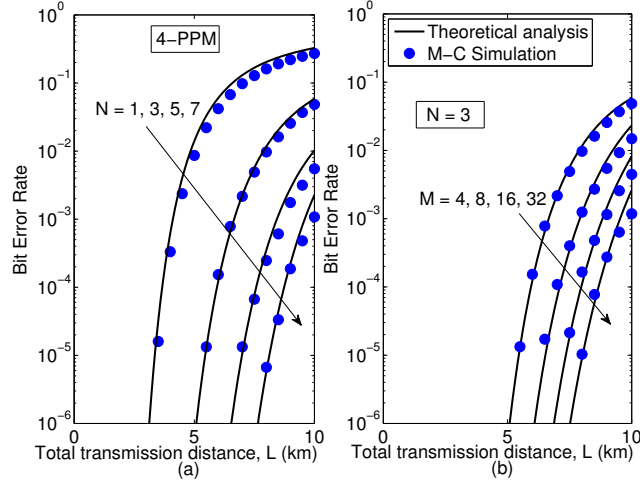


**Figure 6.6:** Downstream transmission: BER versus the transmission distance  $L$ ,  $P_s = 0$  dBm,  $R_b = 1$  Gbps,  $L_{dx,XT} = -30$  dB, and  $C_n^2 = 5 \times 10^{-15}$  for different numbers of relays (a) and orders of PPM modulation (b).

km, respectively. It is also noticed that the distance improvements decrease with the increase of  $N$  due to background and ASE noises accumulation, for example, the distance improvements are 2 km, 1.5 km, and 1.1 km, when  $N$  is increased from 1 to 3, 3 to 5, and 5 to 7, respectively. However, it is not always economically or technically feasible to deploy additional relays. Therefore, another choice to improve the transmission distance is to increase the modulation order  $M$  of PPM scheme. Fig. 6.6(b) shows BER versus  $L$  by fixing  $N = 3$  and increasing  $M$  to investigate the achievable performance improvement of  $M$ -PPM. The distances achieved by employing  $M = 4$ ,  $M = 8$ ,  $M = 16$ , and  $M = 32$  are 5 km, 6.1 km, 6.9 km, and 7.5 km, respectively. The distance improvements tend to decrease when higher orders  $M$  are employed. This is because the pulses are shortened with high values of  $M$ , which are more affected by the pulse broadening due to atmospheric turbulence.

Fig. 6.7 depicts BER versus the transmission bit rate  $R_b$  in Gbps with  $P_s = 0$  dBm and  $L = 4$  km for different PPM modulation orders  $M$  in cases of  $N = 1$  (Fig. 6.7(a)) and  $N = 2$  (Fig. 6.7(b)). It is seen that higher transmission rates are achieved by increasing  $M$ . More specifically, in Fig. 6.7(a), at BER =  $10^{-6}$ , we can achieve  $R_b = 2$  Gbps with 16-PPM and  $N = 1$ . On the other hand in Fig. 6.7(b), much higher  $R_b$  is reached by adding one more relay (i.e.,  $N = 2$ ). For example,  $R_b = 6.5$

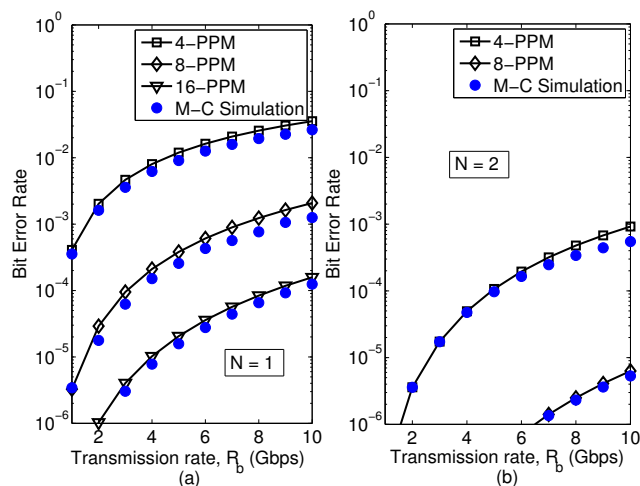


**Figure 6.7:** Downstream transmission: BER versus the transmission rate  $R_b$ ,  $P_s = 0$  dBm,  $L_{dx,XT} = -30$  dB, and  $C_n^2 = 5 \times 10^{-15}$ , and  $L = 4$  km for different orders of PPM modulation with  $N = 1$  (a) and  $N = 2$  (b).

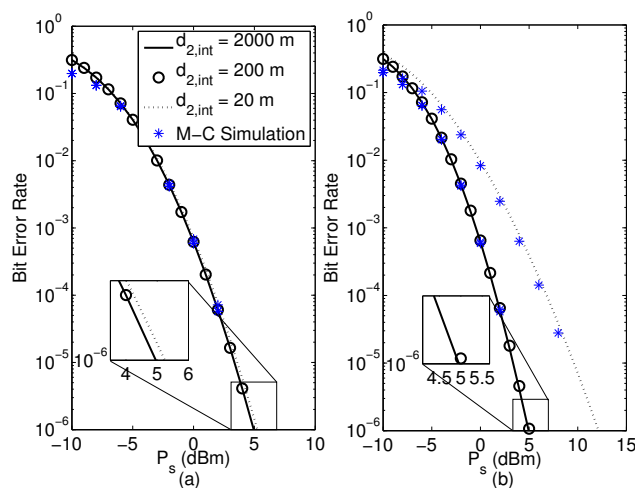


**Figure 6.8:** Upstream transmission: BER versus the average transmitted power per information bit  $P_s$ , with  $L_{dx,XT} = -30$  dB (a) and  $L_{dx,XT} = -15$  dB (b);  $C_n^2 = 5 \times 10^{-15}$ ,  $M = 4$ ,  $N = 1$ ,  $L = 4$  km.

Gbps can be achieved with 8-PPM at  $\text{BER} = 10^{-6}$ , which means 4.5 Gbps higher than the case of one relay with 16-PPM.

### 6.5.2. Upstream Transmission

For the upstream transmission, in the  $(N + 1)$ -th hop, the distances from the desired user (signal) and unwanted user (interferer) to the RN are respectively denoted as  $d_{N+1,sig}$  and  $d_{N+1,int}$ . Fig. 6.8 shows the impact of interchannel crosstalk on the

upstream transmission by evaluating BER versus  $P_s$  within the transmission distance of 4 km with  $N = 1$  (i.e.,  $d_{2, sig} = 2000$  m), for different FSO link lengths from the interferer to the RN  $d_{2, int}$  in two cases, using good demux ( $L_{dx, XT} = -30$  dB) and poor demux ( $L_{dx, XT} = -15$  dB) devices. If a good demux device is used (Fig. 6.8(a)), at  $\text{BER} = 10^{-6}$ , the effect of crosstalk is negligible as  $P_s$  stays the same in both cases of  $d_{2, int} = d_{2, sig} = 2000$  m and  $d_{2, int} = 200$  m. When the interferer is very close to the RN, i.e.,  $d_{2, int} = 20$  m, the impact of crosstalk is still very small as  $P_s$  increases only about 0.2 dB compared to the case when  $d_{2, int} = 2000$  m and  $d_{2, int} = 200$  m. In Fig. 6.8(b), with a poor demux device, the effect of crosstalk is also fragile when  $d_{2, int}$  decreases from 2000 m to 200 m as the required  $P_s$  increases only about 0.1 dB. However, when the interferer is closer to the RN, e.g.,  $d_{2, int} = 20$  m,  $P_s$  increases nearly 7 dB to achieve  $\text{BER} = 10^{-6}$ , compared to the case of  $d_{2, int} = 2000$  m. This is due to the meagre performance of the demux together with the severe effect of turbulence-accentuated interchannel crosstalk.

Finally, Fig. 6.9 shows BER versus  $P_s$  for different  $N$  (Fig. 6.9(a)) and  $M$  (Fig. 6.9(b)) in the case of using poor demux devices and the interferer is very close to the RN (i.e.,  $d_{N+1, int} = 20$  m). To deal with the severe effect of turbulence-accentuated interchannel crosstalk, one can either increase the number of relays or the modulation order of PPM scheme. In Fig. 6.9(a) with 4-PPM, the system performance is considerably improved when more relays are added. Illustratively, the performance improvements when employing 2, 3, and 4 relays are 11 dB, 16 dB, and 18 dB compared to the case when  $N = 1$ . On the other hand, Fig. 6.9(b) shows the performance improvement by increasing  $M$  when only one relay is employed. It is observed that the performance gains are 3 dB, 2 dB, and 1 dB when  $M$  increases from 4 to 8, 8 to 16, and 16 to 32, respectively. The decrease of the performance gains is due to the pulse broadening effect which becomes more severe when  $M$  increases. The efficiency of  $M$ -PPM comes at the expense of large spectrum occupancy and additional synchronization difficulty with large-alphabet PPM. Thus, by suitably choosing  $M$ -PPM and number of relays  $N$  in practical deployment scenarios, the system performance

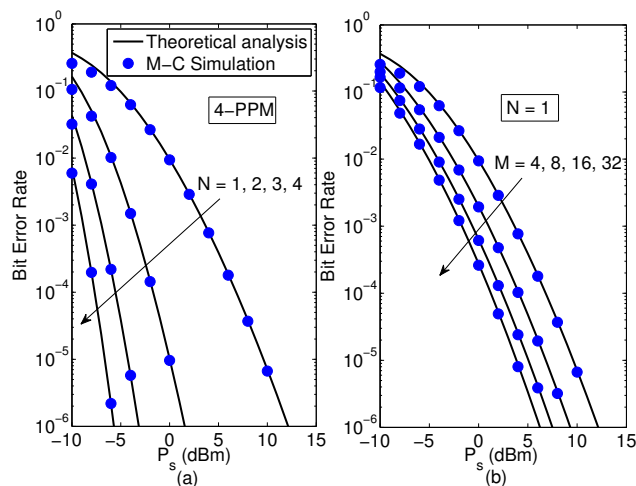


**Figure 6.9:** Upstream transmission: BER versus the average transmitted power per information bit  $P_s$ , with different numbers of relays  $N$  (a) and different PPM modulation orders  $M$  (b);  $L_{dx,XT} = -15$  dB,  $d_{N+1,int} = 20$  m,  $C_n^2 = 5 \times 10^{-15}$ ,  $L = 4$  km.

could be significantly enhanced.

## 6.6. Conclusions

This paper presented a new concept of full-optical access network that employed OAF relaying FSO systems incorporated with WDM. The novel model took advantage of both all-optical relaying FSO transmission and WDM technique, and it could be easily integrated with fiber optics in metro networks to form a low-cost, reliable, flexible, and high-speed optical network. The numerical results showed that atmospheric turbulence and accumulated background and ASE noises had a severe impact on the performance of the proposed system. Nevertheless, thanks to OAF technique combined with  $M$ -PPM modulation, the required  $P_s$  could be significantly reduced and the transmission distance was increased. The required  $P_s$  corresponding to specific values of BER, transmission distance, and turbulence strength were also quantitatively discussed. Finally, the negative effect of turbulence-accentuated interchannel crosstalk in the upstream transmission was thoroughly evaluated.



# Chapter 7

## Generalized Selection Combining in FSO Systems

### 7.1. Introduction

Free-space optical (FSO) communication refers to the transmission of modulated optical beam over the atmosphere, which provides a connectivity with cost-effectiveness, quick deployment, high data rates, and license-free [71]. The main physical impairment over FSO links is atmospheric turbulence-induced fading. To mitigate fading effects, previous studies investigated diversity reception for FSO systems. Several techniques to combine signals at the receiver were studied, including maximum ratio combining (MRC), equal gain combining (EGC), and selection combining (SC) [187], [188]. MRC/EGC provides superior performance, however, it is practically undesirable that the complexities of MRC/EGC are dependent on the number of available branches, which may vary with location and time [189]. In contrast, SC only selects the branch with the strongest instantaneous signal-to-noise ratio (SNR), thus relaxing complexities at the cost of the poorest performance.

For a compromise between MRC/EGC and SC in terms of performance and complexities, generalized selection combining (GSC) scheme combines a subset of  $M$  strongest branches with largest SNR values out of  $L$  available branches. As  $M$  is

decided *a priori*, the GSC( $M,L$ ) scheme has a fixed processing complexity. GSC receiver was extensively investigated in radio frequency (RF) systems [190], [191]. However, the current literature on FSO systems with GSC diversity reception is sparse, mostly due to the difficulty in finding analytical solutions for statistics of GSC output SNR. Threshold-GSC (T-GSC), originally appeared in [190], has been recently introduced for mobile FSO systems [192]. T-GSC slightly differs from GSC in the sense that it combines branches with SNR values larger than a predetermined performance threshold. Nevertheless, the performance analysis in [192] was based on numerical integration, which did not provide a closed-form solution for the output SNR of the T-GSC combiner.

To the best of authors' knowledge, a unified approach and an analytical solution for the GSC scheme in diversity reception FSO systems are currently not available in the literature. For a unified approach in performance analysis, it is necessary to obtain the moment generating function (MGF) of the GSC( $M,L$ ) output SNR. The MGF has played a crucial role in communication theory, as it enables for a simple characterization of the performance metrics of interest in closed-form [193]. In this paper, our contributions are highlighted as follows.

- We concisely derive a novel closed-form expression for the MGF of the GSC( $M,L$ ) output SNR, where the channel statistics in diversity branches are independent and identically distributed (i.i.d.). As the distances of branches are basically the same in FSO systems, the i.i.d. condition can be practically achieved when the separation between receive apertures is longer than the intensity coherence length, which is about 10-20 cm, depending on the link conditions [194].
- We offer a closed-form solution for the complementary incomplete MGF (IMGF) of SNR of a single FSO diversity branch, which is necessary to obtain the MGF of GSC( $M,L$ ) output SNR. IMGF is very useful for various scenarios of interest in communication theory; however, the closed-form expressions of the IMGF are largely unknown for fading distributions and only derived recently in [193], yet for particular applications in RF communications. Our study therefore provides

a complement for [193].

- Our results serve as a unified approach for analyzing GSC performance in FSO systems, since FSO channels are modeled by a mixture-Gamma (MG) distribution, which was lately proposed as an efficient model to capture statistical properties of the atmospheric turbulence-induced fading. MG distribution is used as a tractable approximation of verified turbulence distributions (e.g., Gamma-Gamma and Malaga) [195]- [198].
- Based on the newly derived MGF, the outage probability of FSO systems with GSC( $M,L$ ) scheme is analyzed and confirmed by Monte-Carlo (M-C) simulation. The receiver performs coherent detection and is assumed to have knowledge of each branch signal. The GSC( $M,L$ ) outage performance is further compared with other conventional schemes, including MRC, EGC, and SC.

## 7.2. System and Channel Models

### 7.2.1. System Model

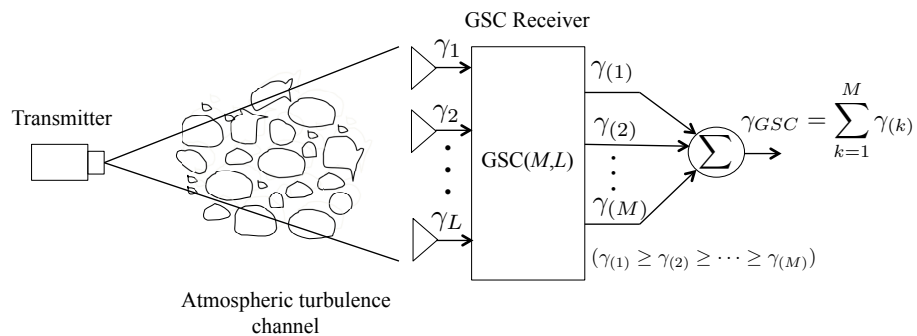


**Figure 7.1:** SIMO FSO System Model with GSC( $M,L$ ) Scheme.

We consider a coherent single-input multiple-output (SIMO) FSO system equipped with a single transmit aperture and  $L$  receive apertures, as illustrated in Fig. 7.1. The transmitter contains a laser source that transmits data modulated onto an optical beam to the  $L$ -aperture receiver. The optical beamwidth is assumed to be wide enough to cover the entire  $L$  apertures at the receiver. The received signal from  $L$

receive apertures, denoted as  $\mathbf{y}$ , is then given by  $\mathbf{y} = \eta \mathbf{I}x + \mathbf{n}$ , where  $\mathbf{I} = [I_1, \dots, I_L]^T$  denotes the turbulence-induced fading channel vector,  $x$  is the binary transmitted intensity signal,  $\eta$  is the effective photo-current conversion ratio of the receiver, and  $\mathbf{n} = [n_1, \dots, n_L]^T$  is the additive white Gaussian noise (AWGN) with variance  $\sigma_n^2$ . In coherent FSO systems,  $\gamma = \frac{(\eta I)}{\sigma_n^2}$  and  $\bar{\gamma} = \frac{(\eta \bar{I})}{\sigma_n^2}$  are the instantaneous electrical SNR and the average electrical SNR of a single diversity branch, respectively [196].

At the receiver, the GSC scheme aims to mitigate the degrading effects of deep fades on the received signal by applying an optimal linear combining rule to a subset of  $M$  highest-SNR diversity branches out of  $L$  available branches [191]. For a GSC( $M$ ,  $L$ ) receiver, ( $M \leq L$ ), in Fig. 7.1, it is defined that the SNR vector from  $L$  available receiving channels can be expressed as  $\boldsymbol{\gamma} = [\gamma_{m_1}, \gamma_{m_2}, \dots, \gamma_{m_k}, \dots, \gamma_{m_L}]^T$ , where  $\gamma_{m_k}$  is the instantaneous SNR of the  $m_k$ -th diversity branch, with  $m_k \in (1, 2, \dots, L)$  for  $1 \leq k \leq L$ , and  $(m_1, m_2, \dots, m_L)$  is a permutation of  $(1, 2, \dots, L)$ . All elements in  $\boldsymbol{\gamma}$  are then arranged in the descending order as  $\tilde{\boldsymbol{\gamma}} = [\gamma_{(1)}, \gamma_{(2)}, \dots, \gamma_{(L)}]^T$  such that  $\gamma_{(1)} \geq \gamma_{(2)} \geq \dots \geq \gamma_{(L)}$ . As a result, the output SNR at the GSC( $M$ ,  $L$ ) combiner is given as

$$\gamma_{GSC} = \sum_{k=1}^M \gamma_{(k)}. \quad (7.1)$$

### 7.2.2. Channel Model

In this section, we utilize an MG distribution to model the SNR of a single channel reception in GSC coherent FSO systems. The MG distribution serves as an effective model, which consists of a convex linear combination of Gamma distributions, to accurately approach well-known atmospheric turbulence-induced fading models, e.g., Gamma-Gamma and Malaga models [195], [196]. Following the same approach as in [195], we derive expressions of the probability density function (PDF)  $f_\gamma(\gamma)$  and cumulative distribution function (CDF)  $F_\gamma(\gamma)$  for a single channel reception,

respectively as

$$f_\gamma(\gamma) = \sum_{i=1}^N a_i \gamma^{b_i-1} e^{-\xi_i \gamma}, \quad (7.2)$$

$$F_\gamma(\gamma) = \int_0^\gamma f_\gamma(t) dt = \sum_{i=1}^N a_i \xi_i^{(-b_i)} \gamma(b_i, \xi_i \gamma), \quad (7.3)$$

where  $a_i$ ,  $b_i$ , and  $\xi_i$  are the parameters of an MG distribution,  $N$  is the number of mixture components, and  $\gamma(\cdot, \cdot)$  is the lower incomplete Gamma function [116, (8.350.1)]. Illustratively, to model a Gamma-Gamma fading channel, these parameters in coherent FSO systems are expressed as

$$\begin{aligned} a_i &= \frac{\theta_i}{\sum_{j=1}^N \theta_j \Gamma(b_j) \xi_j^{-b_j}}, \quad b_i = \alpha, \\ \xi_i &= \frac{\alpha \beta}{t_i \bar{\gamma}}, \quad \theta_i = \frac{(\alpha \beta)^\alpha w_i t_i^{-\alpha+\beta-1}}{\Gamma(\alpha) \Gamma(\beta) \bar{\gamma}^\alpha}, \end{aligned} \quad (7.4)$$

where  $\Gamma(\cdot)$  denotes the Gamma function [116, (8.310.1)].  $\alpha$  and  $\beta$  are the effective numbers of small-scale and large-scale fading parameters, respectively. They are given as

$$\alpha = \left[ \exp \left( \frac{0.49 \sigma_R^2}{(1 + 1.11 \sigma_R^{12/5})^{7/6}} \right) - 1 \right]^{-1} \quad (7.5)$$

$$\beta = \left[ \exp \left( \frac{0.51 \sigma_R^2}{(1 + 0.69 \sigma_R^{12/5})^{5/6}} \right) - 1 \right]^{-1}, \quad (7.6)$$

where  $\sigma_R^2$  is the Rytov variance which is defined as

$$\sigma_R^2 \triangleq 1.23 \left( \frac{2\pi}{\lambda} \right)^{7/6} C_n^2 d^{11/6}, \quad (7.7)$$

with  $\lambda$  is the wavelength,  $d$  is the transmission distance,  $C_n^2$  stands for the altitude-dependent index of the refractive structure parameter and varies from  $10^{-17} \text{ m}^{-2/3}$  to  $10^{-13} \text{ m}^{-2/3}$  [199].  $w_i$  denotes the weight factors that ensures  $\sum_{i=1}^N w_i = 1$  and

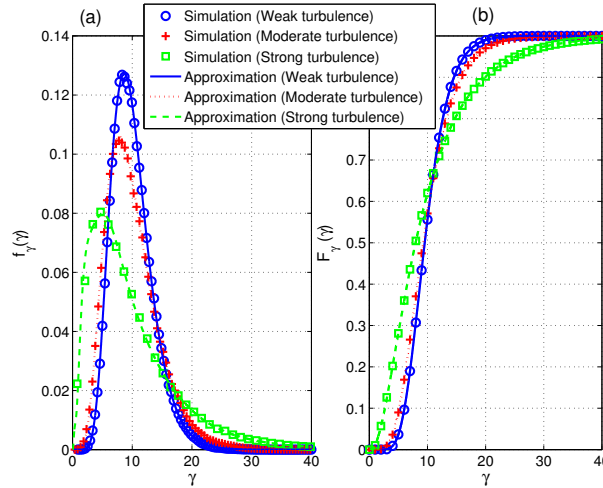


**Figure 7.2:** Plots for PDFs (a) and CDFs (b), respectively in (7.2) and (7.3), under weak ( $C_n^2 = 6 \times 10^{-15}$ ), moderate ( $C_n^2 = 10^{-14}$ ), and strong ( $C_n^2 = 4 \times 10^{-14}$ ) turbulence conditions.

$t_i$  are abscissas of the Laguerre polynomials [200, Table 25.9]. Particularly, Fig. 7.2 further verifies the approximated PDF and CDF in (7.2) and (7.3) with simulated Gamma-Gamma distributions, under the impact of various atmospheric turbulence conditions. It is seen that a small number of mixture components  $N = 10$  yields accurate approximation of the Gamma-Gamma distribution over a wide range of atmospheric turbulence conditions.

## 7.3. GSC Output Statistics and Outage Probability

### 7.3.1. MGF of GSC Output SNR

When  $M$  highest SNR diversity branches are selected out of  $L$  available i.i.d. diversity branches, the moment generating function (MGF) of  $\gamma_{GSC} = \sum_{k=1}^M \gamma_{(k)}$  can be transformed into a univariate integral, given as

$$\Phi_{\gamma_{GSC}}(s) = M \binom{L}{M} \int_0^{\infty} e^{-s\gamma} f_{\gamma}(\gamma) [F_{\gamma}(\gamma)]^{L-M} [\phi_{\gamma}(s, \gamma)]^{M-1} d\gamma, \quad (7.8)$$

where  $\binom{\cdot}{\cdot}$  denotes the binomial coefficient,  $\phi_\gamma(s, \gamma) = \int_\gamma^\infty e^{-st} f_\gamma(t) dt$  defines a complementary incomplete MGF for the instantaneous SNR of a single diversity branch [191]. With the help of (7.2) and [116, (3.381.3)],  $\phi_\gamma(s, \gamma)$  can be expressed as

$$\phi_\gamma(s, \gamma) = \sum_{i=1}^N a_i (s + \xi_i)^{-b_i} \Gamma(b_i, (s + \xi_i) \gamma), \quad (7.9)$$

where  $\Gamma(\cdot, \cdot)$  denotes the upper incomplete Gamma function [116, (8.350.2)].

### Theorem 1

The MGF of GSC( $M, L$ ) output SNR can be given in a closed-form expression as

$$\begin{aligned} \Phi_{\gamma_{GSC}}(s) = & M \binom{L}{M} \widetilde{\sum}_{\mathbb{S}^\Phi} \widetilde{\prod}_{i,n,l} A_{i,n,l}^\Phi \varepsilon^{-\nu} \Gamma(\nu) \\ & \times F_A \left( \nu; \sigma_1, \dots, \sigma_k, \dots, \sigma_{k_i}^\phi; \rho_1, \dots, \rho_k, \dots, \rho_{k_i}^\phi; \right. \\ & \left. \frac{\tau_1}{\varepsilon}, \dots, \frac{\tau_k}{\varepsilon}, \dots, \frac{\tau_{k_i}^\phi}{\varepsilon} \right), \quad (7.10) \\ & \left[ \rho_k > 0, \nu > 0, \sum \tau_k < \varepsilon \right], \end{aligned}$$

where  $\widetilde{\sum}_{\mathbb{S}^\Phi}$ ,  $\widetilde{\prod}_{i,n,l}$ ,  $A_{i,n,l}^\Phi$ ,  $\varepsilon$ ,  $\nu$ ,  $\sigma_k$ ,  $\rho_k$ , and  $\tau_k$  are defined in Appendix A.  $F_A(\cdot; \cdot; \cdot)$  denotes the Appell hypergeometric function defined as [116, (9.19)].

*Proof.* The proof is provided in Appendix A. □

### 7.3.2. CDF of GSC( $M, L$ ) Output SNR

#### Lemma 1

Let  $\mathbb{F}_{\gamma_{GSC}}(\gamma)$  denote the CDF of the GSC output SNR and be given in a closed-form expression as

$$\mathbb{F}_{\gamma_{GSC}}(\gamma) = M \binom{L}{M} \widetilde{\sum}_{\mathbb{S}^\Phi} \widetilde{\prod}_{i,n,l} A_{i,n,l}^\Phi B_{i,n}^\Phi \frac{\gamma^\nu}{\nu} \Phi(\nu; \nu + 1; -\xi_i \gamma), \quad (7.11)$$

where  $B_{i,n}^\Phi$  is defined in Appendix B. It is noted that the Kummer confluent hypergeometric function  $\Phi(\cdot; \cdot; \cdot)$  has a second notation as  ${}_1F_1(\cdot; \cdot; \cdot)$  [116, (9.210.1)].

*Proof.* The proof is provided in Appendix B. □

### 7.3.3. Outage Probability

At a given transmission rate  $R_b$ , the outage probability can be defined as  $P_{out} = \Pr(\mathbb{C}(\gamma) < R_b)$ , where  $\mathbb{C}(\gamma)$  is the instantaneous capacity of the channel, and  $\gamma$  is the instantaneous SNR. Since  $\mathbb{C}(\cdot)$  is a monotonically increasing function with respect to  $\gamma$ , the outage probability can be obtained as  $P_{out} = \Pr(\gamma < \gamma_{th})$ , where  $\gamma_{th} = \mathbb{C}^{-1}(R_b)$  is the predetermined threshold SNR required to support the data rate  $R_b$ . In practice,  $\gamma_{th}$  is chosen based on modulation scheme and targeted spectral efficiency. The outage probability of the GSC coherent FSO system is defined as the probability that the GSC output instantaneous SNR  $\gamma_{GSC}$  falls below the threshold  $\gamma_{th}$ . Thus, from *Lemma 1*, the outage probability of GSC coherent FSO systems can be expressed as  $P_{out} = \mathbb{F}_{\gamma_{GSC}}(\gamma_{th})$ .

## 7.4. Numerical Results

In this section, we investigate the outage performance of GSC coherent FSO systems under the effect of different turbulence conditions, which is verified by M-C simulation. The main parameters are set as  $\lambda = 1550$  nm,  $N = 10$ ,  $L = 5$ ,  $\gamma_{th} = 0$  dB, truncation values  $T_1 = T_2 = 30$ . From a theoretical viewpoint, GSC(1, $L$ ) and GSC( $L$ , $L$ ) are simply the classical SC and MRC (coherent detection) receivers, respectively [191]. For a comparison, simulated EGC outage performance is also plotted.

Firstly, Fig. 7.3 depicts the outage probability for GSC( $M$ ,5) as a function of the normalized average SNR per branch defined as  $(\bar{\gamma}/\gamma_{th})$ . From Fig. 7.3, it is useful that the mean SNR per branch to satisfy an outage requirement can be determined for GSC( $M$ ,5) coherent FSO systems. In addition, increasing the number of selected



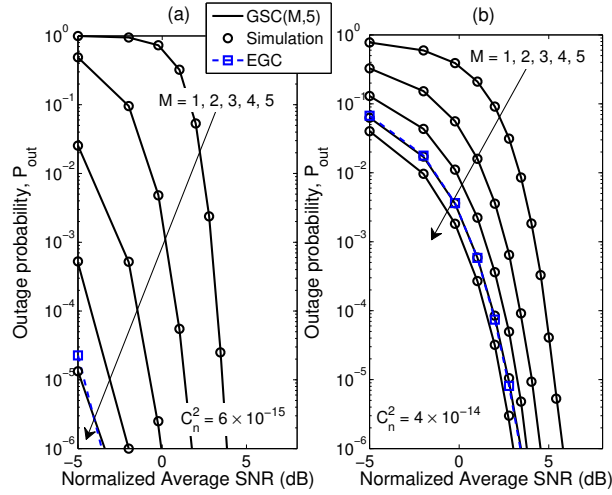


**Figure 7.3:** Outage probability versus the normalized average SNR per branch for GSC( $M,5$ ) under weak turbulence (a), and strong turbulence (b).

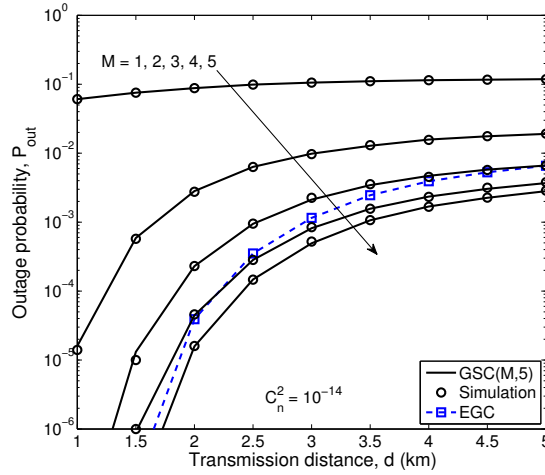


**Figure 7.4:** Outage probability versus the transmission distance  $d$  (km) for GSC( $M,5$ ) with  $C_n^2 = 10^{-14}$ .

branches  $M$  yields a better GSC performance. Although MRC (i.e., GSC(5,5)) provides the best outage performance, it brings little additional improvements when applying to low-SNR diversity branches under strong turbulence, while entailing extra hardware complexity. On the other hand, GSC excludes the low-SNR branches, thus relaxing complexities while achieving the performance close to that of MRC, and similar to that of EGC at GSC(4,5) (Fig. 7.3(b)). Finally, Fig. 7.4 shows  $P_{out}$  versus  $d$ , which reveals the maximum transmission distance achieved by GSC( $M,5$ ) with targeted  $P_{out} = 10^{-6}$ . This serves as a practical reference for engineering designs. It is also observed that EGC performs better than GSC(4,5) when communicating over

short distance (e.g.,  $d \leq 2$  km). Over long distance (e.g.,  $d > 2$  km), as turbulence becomes stronger, GSC(4,5) outperforms EGC by excluding the lowest SNR diversity branch that affects the outage performance.

## 7.5. Conclusions

The outage performance of GSC for coherent FSO systems was analytically studied and further verified by M-C simulation, when the received signals experience i.i.d. atmospheric turbulence-induced fading. The key contribution was the derivation of the MGF for the GSC( $M,L$ ) output SNR, which serves as the mathematical foundation for analyzing the system performance. Capitalizing on this novel result, the outage probability of GSC( $M,5$ ) was evaluated and compared with conventional schemes (i.e., MRC, EGC, and SC).

# Chapter 8

## Summary and Future Research

### 8.1. Summary

Current backhaul networks are mostly built with microwave links and fiber/copper-based links, which cannot cope with the capacity, latency, reliability, energy efficiency, and cost effectiveness required for the fifth generation (5G) of mobile networks. Therefore, the 5G backhaul research has been triggered, aiming at bridging the gap between the requirements stipulated by the 5G radio access network (RAN) and the realistic backhaul capabilities, from two different perspectives. The first consists of evolving the current backhaul (microwave, optical fiber, copper, etc.) to meet 5G expectations and encompassing new wireless technologies such as millimeter-wave (mmWave) and free-space optics (FSO). The other backhaul research perspective looks at adapting the 5G RAN to the available backhaul with realistic performance, such as investigating intermediate RAN architectures between the centralized RAN and the distributed RAN to fit the backhaul/fronthaul capabilities. In this thesis, the focus is on the channel modeling for the mixture of enabling wireless technologies including mmWave and FSO for 5G backhaul networks.

To enable the mixture of mmWave and FSO, how to accurately capture the channel characteristics of both mmWave and FSO under various transmission condi-

tions for performance evaluation is very important. To do so, the following problems need to be addressed. Firstly, the analysis with different channel models and effects induced by physical layer impairments would result in highly complex analytical problems. Secondly, the effectiveness of different signal processing and coding techniques needs to be investigated to optimize the performance of the mixed systems. Finally, comprehensive experimental implementation should be conducted to validate the analytical models and performance results.

To derive the analytical model for performance analysis, we strive to formulate mathematical models describing the effects of transmission channels and study the statistical characterization of the end-to-end signal-to-noise ratio (SNR) of the mixed systems. On the other hand, improvement techniques suitable for the mixture of mmWave and FSO systems are proposed, including two-way communications, relaying techniques, and diversity reception with generalized selection combining (GSC). Furthermore, comprehensive experiments based on real environmental data and computer-based Monte-Carlo simulations are implemented to evaluate the accuracy of the derived analytical model and performance results.

Against the above-mentioned background, the key contributions in this thesis are summarized as follows.

Chapter 4 studies the performance of mixed mmWave RF/FSO systems as a highly scalable and cost-effective solution for the 5G mobile backhaul networks, in which the mmWave RF and FSO fading channels are respectively modeled by the Rician and the generalized Malaga ( $\mathcal{M}$ ) distributions. The effect of pointing errors due to the misalignments between the transmitter and the receiver in the FSO link is also included. The key contributions in this chapter are the novel closed-form expressions for the cumulative distribution function (CDF), the probability density function (PDF), and the moment generating function (MGF) of the end-to-end received signal-to-noise ratio (SNR). Capitalizing on these new results, the outage probability, the average bit error rate (ABER), and the average capacity of the mixed mmWave RF/FSO systems could be analytically analyzed. Numerical results further validate

the mathematical analysis by Monte-Carlo (M-C) simulations.

Chapter 5 studies the implementation of two-way transmission in an amplify-and-forward (AF) relaying FSO system utilizing a relay with optical amplifier. The performance of the proposed FSO system using subcarrier intensity modulation (SIM) with intensity modulation/direct detection (IM/DD) over independent but not necessarily identically distributed (i.n.i.d) Malaga ( $\mathcal{M}$ ) atmospheric turbulence channels in presence of pointing errors is studied. The key contributions in this chapter are the exact closed-form expressions for the moment generating function (MGF) and cumulative distribution function (CDF) of the end-to-end signal-to-noise ratio (SNR) obtained in terms of extended generalized bivariate Meijer's G-functions (EGBMGF). Capitalizing on these new results, we derive exact closed-form expressions for various performance metrics of the considered FSO system including the outage probability, the average bit error rate (ABER), and the ergodic achievable-rate. All analytical results are thoroughly confirmed by M-C simulations.

In Chapter 6, the key contribution is the performance analysis of a newly proposed multi-hop FSO system employing optical amplify-and-forward (OAF) relaying technique and wavelength division multiplexing (WDM) for multiple users in areas where installation of optical fiber is unfavorable. In WDM/FSO systems, WDM channels suffer from the interchannel crosstalk while FSO channels can be severely affected by the atmospheric turbulence. These impairments together with the accumulation of background and amplifying noises over multiple relays significantly degrade the overall system performance. To deal with this problem, the use of the  $M$ -ary pulse position modulation ( $M$ -PPM) together with the OAF relaying technique is advocated as a powerful remedy to mitigate the effects of atmospheric turbulence. For the performance analysis, we use a realistic model of Gaussian pulse propagation to investigate major atmospheric effects, including signal turbulence and pulse broadening. We qualitatively discuss the impact of various system parameters, including the required average transmitted powers per information bit corresponding to specific values of bit error rate (BER), transmission distance, number of relays, and turbulence

strength. Our numerical results are also thoroughly validated by M-C simulations.

Chapter 7 investigates the outage performance of generalized selection combining (GSC) receiver that combines a subset of  $M$  strongest branches in terms of instantaneous signal-to-noise ratio (SNR) out of  $L$  available branches, i.e. GSC( $M,L$ ), for coherent free-space optical (FSO) communication systems. The key contribution is a closed-form solution for the moment generating function (MGF) of the GSC( $M,L$ ) output SNR, concisely derived when the total received signal experiences independent and identically distributed (i.i.d.) atmospheric turbulence-induced fading modeled by a mixture-Gamma distribution. As a result, the outage probability of the GSC receiver for coherent FSO systems is obtained and comprehensively studied. Numerical results show the crucial role of selected diversity branches under the effect of atmospheric turbulence channels, which are further verified by M-C simulations.

## 8.2. Future Research

### 8.2.1. Motivations

Current terrestrial backhauling/fronthauling solutions utilizing both wired or wireless are based on delivering the traffic of small cells to an aggregated point (i.e., central hub), which would be ideally located at an existing macrocell tower. In [201], the authors stated that the key challenge in designing such backhaul/fronthaul network is how to optimize the position of the central hubs. Such a problem may not have optimal solution since in ultra-dense small-cell networks (i.e., 40-50 small-cell base stations/ $km^2$ ) some small cells are difficult to reach and line-of-sight (LOS) propagation (using mmWave/FSO) is impossible. In such scenarios, RF non-LOS point-to-multipoint solutions that rely on licensed sub-6 GHz spectrum or microwave RF could be used at the expense of severe interference, congestion, and high deployment cost [202]. Therefore, a novel design of vertical backhaul/fronthaul for 5G networks was proposed in [203], utilizing unmanned aerial vehicles (UAVs) and FSO technolo-

gies. More specifically, UAVs are equipped with steerable FSO units with optical beam steering devices to establish wireless links with the radio access networks or hub points on ground via highly directional FSO beams.

### 8.2.2. Research Directions

The vertical backhaul/fronthaul for 5G networks proposed in [203] was innovative, as it introduced the UAV platform to solve the problem associated with deploying backhauling/fronthauling small cells in dense urban areas. To reduce the deployment cost of terrestrial FSO networks, the aggregation hub can be implemented in the stratosphere instead of ground where it is more likely to have a LOS between the small cells and flying UAVs. Although maintaining UAV platform everywhere may not be practical, the UAVs could be deployed in areas where urgent needs of high bandwidth connections are required (e.g., a football match at a stadium with 80,000 seats in Tokyo Olympic Games 2020) or in disaster areas, which provide the ability to adjust and adapt to the changes in the network in a flexible and timely manner. However, UAV-ground station links in a stand-alone system may not be a resilient solution when disasters happen (e.g., an earthquake or a tsunami). The terrestrial communications network in a large disaster area will be physically destroyed, and the connections between UAVs and ground core networks are lost. Under this massive damage, satellite communications are important from various perspectives, as satellites are the only wireless communications infrastructure not susceptible to damage from disasters [204].

Therefore, we propose to study a new architecture for the future 5G and beyond networks, which consists of interconnecting satellite platform with airborne UAV platform and ground-based cellular base stations via FSO links to provide all-optical Giga-bit vertical backhaul/fronthaul links and resilient networks for emergency responses, rescues, or relief situations, as depicted in Fig. 8.1. The objectives of our proposal are threefold. Firstly, since the UAVs are located in a cloud-free atmospheric altitude (e.g., 17-25 km above the ground), they are capable of providing reliable links between

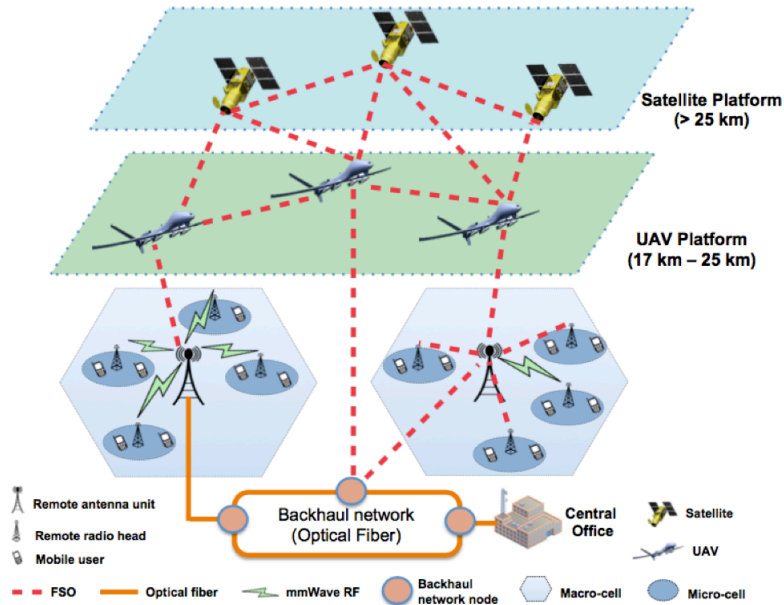


**Figure 8.1:** Future research: Relaying satellite-UAV-ground station for vertical backhaul/fronthaul in resilient 5G and beyond wireless networks.

different UAVs or between UAVs and satellites. Moreover, UAVs can act as relay stations to forward the high capacity optical data through the atmosphere to the ground, which vertically provide feasible LOS connection in almost all coverage areas, thereby causing less shadowing than terrestrial systems. Secondly, the satellite-to-ground link can be split in two relaying parts: satellite-to-UAV FSO link and UAV-to-ground FSO link. This would not only provide high capacity backhaul/fronthaul all-optical links but also relax the satellite front-end requirement and reduce its on-board processing time [205]. Finally, the integrated all-optical relaying satellite-UAV-ground station systems could help reduce the damage to communications systems inflicted by strong earthquakes in the future. With fully automatic transportable ground stations being deployed when terrestrial infrastructures are physically destroyed, the vertical relaying satellite-UAV-ground station networks can be used to provide broadcasting and broadband services over a wide coverage of disaster areas, which is particularly useful for recovery plans and emergency rescues. As Japan consists of several thousands of islands, the satellite and UAV platforms could further guarantee the availability of communications between islands in disaster areas.



# Acknowledgements

First and foremost, I would like to express my sincere gratitude to my supervisor, Professor Anh T. Pham, for his continuous support, guidance, and encouragement that enabled me to complete this research. His advices on both research and professional career have been priceless. I am immensely grateful and happy to be his student in Computer Communications Laboratory at the University of Aizu.

I would like to extend my special appreciation and thanks to my doctoral dissertation review committee, Professor Toshiaki Miyazaki, Professor Igor Lubashevsky, and Professor Truong Cong Thang, for providing insightful comments and suggestions to fulfill my research contributions.

Many thanks also goes to my lab mates, who made my Ph.D. life a wonderful and memorable experience. My most heartfelt acknowledgement is destined for my lover, Alona Sarmiento, whose love and supporting care bring happiness and joy to my life.

I gratefully acknowledge the financial support from Japanese government through MonbuKagaku-sho (MEXT) scholarship during my graduate studies at the University of Aizu. My thanks also goes to IEEE Communications Society, IEEE UK Communications Chapter, Marubun Research Promotion Foundation, Telecommunications Advancement Foundation, NEC C & C Foundation, and Research Foundation for the Electro-technology of Chubu for their travel grants to give me opportunities to attend international conferences.

Last but not least, my profound love and appreciation go to my parents, Trinh Viet Hung and Vu Ngoc Diep, and my younger brother, Trinh Viet Duc, for their constant support and trust in me. This dissertation is dedicated to them.

# Bibliography

- [1] Y. Kishiyama, A. Benjebbour, S. Nagata, Y. Okumura, and T. Nakamura, “NTT DOCOMO 5G Activities-Toward 2020 Launch of 5G Services,” *NTT DOCOMO Technical Journal*, vol. 17, no. 4, pp. 4–15, Apr. 2016.
- [2] M. Elkashlan, T. Q. Duong, and H.-H. Chen, “Millimeter-wave communications for 5G: fundamentals: Part I [Guest Editorial],” *IEEE Commun. Mag.*, vol. 52, no. 9, pp. 52–54, Sept. 2014.
- [3] K. -I. Kitayama, “Coordinated role of optical and radio network in 5G-era,” *In Proc. of the 2015 International Topical Meeting on Microwave Photonics (MWP)*, pp. 1–4, Paphos, Cyprus, October 2015.
- [4] M. Jaber, M. A. Imran, R. Tafazolli, and A. Tukmanov, “5G backhaul challenges and emerging research directions: A survey,” *IEEE Access*, vol. 4, pp. 1743–1766, May 2016.
- [5] P. V. Trinh, N. T. Dang, and A. T. Pham, “All-optical relaying FSO systems using EDFA combined with optical hard-limiter over atmospheric turbulence channels,” *IEEE/OSA J. Lightw. Technol.*, vol. 33, no. 19, pp. 4132–4144, October 2015.
- [6] H. T. T. Pham, P. V. Trinh, N. T. Dang, and A. T. Pham, “Secured relay-assisted atmospheric optical CDMA systems over turbulence channels,” *IET Commun.*, vol. 9, no. 5, pp. 241–248, Oct. 2015.
- [7] P. V. Trinh, T. C. Thang, and A. T. Pham, “Mixed mmWave RF/FSO relaying systems over generalized fading channels with pointing errors,” *IEEE Photon. J.*, vol. 9, no. 1, Art. no. 5500414, Feb. 2017.
- [8] V. V. Mai and A. T. Pham, “Performance analysis of parallel FSO/MMW systems with adaptive rate under weather effects,” *In Proc. of the IEEE 21st Asia-Pacific Conference on Communications (APCC)*, pp. 193–198, Kyoto, Japan, October 2015.
- [9] P. V. Trinh, T. V. Pham, H. V. Nguyen, S. X. Ng, and A. T. Pham, “Performance of free-space QKD systems using SIM/BPSK and dual-threshold/direct detection,” *In Proc. of the 2016 IEEE Globecom, Workshop on Quantum Communications and Information Technology*, Washington, DC USA, Dec. 2016.

- 
- [10] P. V. Trinh and A. T. Pham, "Design and secrecy performance of novel two-way free-space QKD protocol using standard FSO systems," *In Proc. of the International Conference on Communications (ICC)*, Paris, France, May 2017.
- [11] H. V. Nguyen, P. V. Trinh, A. T. Pham, Z. Babar, D. Alanis, P. Botsinis, D. Chandra, S. X. Ng, and L. Hanzo, "Network coding aided cooperative quantum key distribution over free-space optical channels," *IEEE Access*, Accepted for publication, Jun. 2017.
- [12] P. V. Trinh, T. C. Thang, and A. T. Pham, "Two-way all-optical AF relaying FSO systems over Malaga ( $\mathcal{M}$ ) channels with pointing errors," *In Proc. of the IEEE International Conference on Communications (ICC)*, May 2016.
- [13] P. V. Trinh, N. T. Dang, T. C. Thang, and A. T. Pham, "Performance of all-optical amplify-and-forward WDM/FSO relaying systems over atmospheric dispersive turbulence channels," *IEICE Trans. Commun.*, vol. E99-B, no. 6, pp. 1255–1264, Jun. 2016.
- [14] A. Gupta and R. K. Jha, "A survey of 5G network: architecture and emerging technologies," *IEEE Commun. Surveys Tuts.*, vol. 3, pp. 1206–1232, Aug. 2015.
- [15] K. R. Santhi, V. K. Srivastava, G. Senthil Kumaran, and A. Butare, "Goals of true broad bands wireless next wave (4G5G)," *In Proc. IEEE 58th Veh. Technol. Conf.*, vol. 4, pp. 2317–2321, Oct. 2003.
- [16] S. Sesia, I. Toufik, and M. Baker, *Eds.*, *LTE: The UMTS Long Term Evolution*. New York, NY, USA: Wiley, 2009.
- [17] Cisco, "Visual Networking Index," White paper, Feb. 2015 [Online]. Available: [www.cisco.com](http://www.cisco.com).
- [18] T. S. Rappaport, W. Roh, and K. Cheun, "Wireless engineers long considered high frequencies worthless for cellular systems. They couldnt be more wrong," *IEEE Spectr.*, vol. 51, no. 9, pp. 34–58, Sep. 2014.
- [19] H. Holma, A. Toskala, and J. Reunanen, *LTE Small Cell Optimization: 3GPP Evolution to Release 13*. Hoboken, NJ, USA: Wiley, 2015.
- [20] Huawei Technologies Co., "document: eLTE2.2 DBS3900 LTE configuration principles," 2014 [Online]. Available: [www.e.huawei.com](http://www.e.huawei.com).
- [21] W. Stallings, *Data and Computer Communications*. Upper Saddle River, NJ, USA: Pearson/Prentice-Hall, 2007.
- [22] B. Bangerter, S. Talwar, R. Arefi, and K. Stewart, "Intel networks and devices for the 5G era," *IEEE Commun. Mag.*, vol. 52, no. 2, pp. 90–96, Feb. 2014.
- [23] J. G. Andrews, S. Buzzi, W. Choi, S. V. Hanly, A. Lozano, A. C. K. Soong, and J. C. Zhang, "What will 5G be?," *IEEE J. Sel. Areas Commun.*, vol. 32, no. 6, pp. 1065–1082, Jun. 2014.

- [24] F. Khan, Z. Pi, and S. Rajagopal, "Millimeter-wave mobile broadband with large scale spatial processing for 5G mobile communication," in *Proc. 50th Annu. Allerton Conf. Commun. Control Comput. (Allerton)*, pp. 1517–1523, 2012.
- [25] P. Adhikari, *Understanding millimeterwave wireless communication*. Loea Corp., White paper, 2008.
- [26] M. Agiwal, A. Roy, and N. Saxena, "Next generation 5G wireless networks: A comprehensive survey," *IEEE Commun. Surveys Tuts.*, vol. 18, no. 3, pp. 1617–1655, Third Quarter 2016.
- [27] GSMA Intelligence, *Understanding 5G: Perspectives on future technological advancements in mobile*. White paper, 2014.
- [28] S. Chen and J. Zhao, "The requirements, challenges, and technologies for 5G of terrestrial mobile telecommunication," *IEEE Commun. Mag.*, vol. 52, no. 5, pp. 36–43, May 2014.
- [29] 3GPP, *The Mobile Broadband Standard*. [Online]. Available: [www.3gpp.org](http://www.3gpp.org), 2015.
- [30] N. J. Gomes, P. Chanclou, P. Turnbull, A. Magee, and V. Jungnickel, "Fronthaul evolution: From CPRI to Ethernet," *Opt. Fiber Technol.*, vol. 26, pp. 50–58, Dec. 2015.
- [31] C. -L. I, Y. Yuan, J. Huang, S. Ma, C. Cui, and R. Duan, "Rethink fronthaul for soft RAN," *IEEE Commun. Mag.*, vol. 53, no. 9, pp. 82–88, Sep. 2015.
- [32] C. L. I, J. Huang, Y. Yuan, S. Ma, and R. Duan, "NGFI, the xHaul," In *Proc. IEEE Globecom Workshops (GC Wkshps)*, pp. 1–6, Dec. 2015.
- [33] 3GPP, *An Interview With Philippe Reininger—RAN3 Chairman*. [Online]. Available: [www.3gpp.org](http://www.3gpp.org), 2015.
- [34] T. Tashiro, S. Kuwano, J. Terada, T. Kawamura, N. Tanaka, S. Shigematsu, and N. Yoshimoto, "A novel DBA scheme for TDM-PON based mobile fronthaul," In *Proc. Opt. Fiber Commun. Conf. Exhibit. (OFC)*, pp. 1–3, Mar. 2014.
- [35] A. Maeder, M. Lalam, A. D. Domenico, E. Pateromichelakis, D. Wubben, J. Bartelt, R. Fritzsche, and P. Rost, "Towards a flexible functional split for cloud-RAN networks," In *Proc. Eur. Conf. Netw. Commun. (EuCNC)*, pp. 1–5, Jun. 2014.
- [36] J. Hoydis, S. Ten Brink, and M. Debbah, "Massive MIMO in the UL/DL of cellular networks: How many antennas do we need?," *IEEE J. Sel. Areas Commun.*, vol. 31, no. 2, pp. 160–71 Feb. 2013.
- [37] T. S. Rappaport, S. Sun, R. Mayzus, H. Zhao, Y. Azar, K. Wang, G. N. Wong, J. K. Schulz, M. Samimi, and F. Gutierrez, "Millimeter wave mobile communications for 5G cellular: It will work!," *IEEE Access.*, vol. 1, pp. 335–349, May 2013.

- 
- [38] C. -X. Wang, F. Haider, X. Gao, X. -H. You, Y. Yang, D. Yuan, H. M. Aggoune, H. Hass, S. Fletcher, and E. Hepsaydir, "Cellular architecture and key technologies for 5G wireless communication networks," *IEEE Commun. Mag.*, vol. 52, no. 2, pp. 122–130, Feb. 2014.
- [39] S. F. Yunas, M. Valkama and J. Niemela, "Spectral and energy efficiency of ultra-dense networks under different deployment strategies," *IEEE Commun. Mag.*, vol. 53, no. 1, pp. 90–100, Jan. 2015.
- [40] B. Soret, K. I. Pedersen, N. T. K. Jorgensen, and V. F. -Lopez, "Interference coordination for dense wireless networks," *IEEE Commun. Mag.*, vol. 53, no. 1, pp. 102–109, Jan. 2015.
- [41] A. Asadi, V. Sciancalepore and V. Mancuso, "On the efficient utilization of radio resource in extremely dense wireless networks," *IEEE Commun. Mag.*, vol. 53, no. 1, pp. 126–132, Jan. 2015.
- [42] N. Bhushan, J. Li, D. Malladi, R. Gilmore, D. Brenner, A. Damnjanovic, R. T. Sukhavasi, C. Patel, and S. Geirhofer, "Network densification: The dominant theme for wireless evolution in 5G," *IEEE Commun. Mag.*, vol. 52, no. 2, pp. 82–89, Feb. 2014.
- [43] M. Condoluci, M. Dohler, G. Araniti, A. Molinaro, and K. Zheng, "Toward 5G DenseNets: Architectural advances for effective machine-type communications over femtocell," *IEEE Commun. Mag.*, vol. 53, no. 1, pp. 134–141, Jan. 2015.
- [44] X. Ge, H. Cheng, M. Guizani, and T. Han, "5G wireless backhaul networks: Challenges and research advances," *IEEE Network*, vol. 28, no. 6, pp. 6–11, Nov. 2014.
- [45] J. He, K. Yang, K. Guild, and H. Chen, "Application of IEEE 802.16 mesh networks as the backhaul of multihop cellular networks," *IEEE Commun. Mag.*, vol. 45, no. 9, pp. 82–90, Sept. 2007.
- [46] S. Hur, T. Kim, D. J. Love, J. V. Krogmeier, T. A. Thomas, and A. Ghosh, "Millimeter wave beamforming for wireless backhaul and access in small cell networks," *IEEE Trans. Wireless Commun.*, vol. 61, no. 10, pp. 4391–4403, Oct. 2013.
- [47] C. Dehos, J. L. Gonzalez, A. D. Domenico, D. Ktenas, and L. Dussopt, "Millimeter-wave access and backhauling: The solution to the exponential data traffic increase in 5G mobile communications systems?," *IEEE Commun. Mag.*, vol. 52, no. 9, pp. 88–95, Sept. 2014.
- [48] X. Ge, S. Tu, G. Mao, C.-X. Wang, and T. Han, "5G ultra-dense cellular networks," *IEEE Wireless Commun.*, vol. 23, no. 1, pp. 72–79, Feb. 2016.
- [49] *Backhaul technologies for small cells: Use cases, requirements and solution.* Small Cell Forum, Dursley, U.K., Tech. Rep. 049.01.01, Feb. 2013.

- [50] M. -C. Jeong, J. -S. Lee, S. -Y. Kim, S. -W. Namgung, J. -H. Lee, M. -Y. Cho, S. -W. Huh, Y. -S. Ahn, J. -W. Cho, and J. -S. Lee, “8x10-Gb/s terrestrial optical free-space transmission over 3.4 km using an optical repeater,” *IEEE Photon. Technol. Lett.*, vol. 15, no. 1, pp. 171–173, Jan. 2003.
- [51] F. Barros, K. Ahl, and V. Chaillou, “Creating a Connected Continent,” *Press Conference Warsaw*. [Online]. Available: [www.ftthcouncil.eu](http://www.ftthcouncil.eu), 2015.
- [52] Z. Roth, M. Goldhamer, N. Chayat, A. Burr, M. Dohler, N. Bartzoudis, C. Walker, Y. Leibe, C. Oestges, M. Brzozowy, and I. Bucaille, “Vision and architecture supporting wireless Gbit/sec/km<sup>2</sup> capacity density deployments,” *In Proc. Future Netw. Mobile Summit*, pp. 1–7, Jun. 2010.
- [53] G. R. MacCartney, J. Zhang, S. Nie, and T. S. Rappaport, “Path loss models for 5G millimeter wave propagation channels in urban microcells,” *In Proc. IEEE Global Commun. Conference (GLOBECOM)*, pp. 3948–3953, Dec. 2013.
- [54] T. S. Rappaport, J. N. Murdock, and F. Gutierrez, Jr., “State of the art in 60-GHz integrated circuits and systems for wireless communications,” *Proc. IEEE*, vol. 99, no. 8, pp. 1390–1436, Aug. 2011.
- [55] T. S. Rappaport, “Millimeter Wave Wireless Communications: The Renaissance of Computing and Communications.,” *IEEE International Communications Conference (ICC)*, Sydney, Jun. 2014.
- [56] S. Nie, G. R. MacCartney, S. Sun, and T. S. Rappaport, “28 GHz and 73 GHz signal outage study for millimeter wave cellular and backhaul communications,” *in Proc. IEEE Int. Conf. Commun. (ICC)*, pp. 4856–4861, Sydney, Jun. 2014.
- [57] T. S. Rappaport, R. W. Heath, R. C. Daniels, and J. N. Murdock, *Millimeter Wave Wireless Communications*. 1st ed. Upper Saddle River, NJ, USA: Prentice-Hall, Sep. 2014.
- [58] R. Baldemair, T. Irnich, K. Balachandran, E. Dahlman, G. Mildh, Y. Selen, S. Parkvall, M. Meyer, and A. Osseiran, “Ultra-dense networks in millimeter-wave frequencies,” *IEEE Commun. Mag.*, vol. 53, no. 1, pp. 202–208, Jan. 2015.
- [59] J. A. Zhang, W. Ni, J. Matthews, C. -K. Sung, X. Huang, H. Suzuki, and I. Collings, “Low latency integrated point-to-multipoint and E-band point-to-point backhaul for mobile small cells,” *In Proc. IEEE Int. Conf. Commun. Workshops (ICC)*, pp. 592–597, Jun. 2014.
- [60] R. Taori and A. Sridharan, “In-band, point to multi-point, mm-wave backhaul for 5G networks” *In Proc. IEEE Int. Conf. Commun. Workshops (ICC)*, pp. 96–101, Jun. 2014.
- [61] T. K. Vu, M. Bennis, S. Samarakoon, M. Debbah, and M. Latva-Aho, “Joint in-band backhauling and interference mitigation in 5G heterogeneous networks” *In Proc. Eur. Wireless*, pp. 1–6, Oulu, Finland, May 2016.

- [62] K. Zheng, L. Zhao, J. Mei, M. Dohler, W. Xiang, and Y. Peng, “10 Gb/s Het-SNets with millimeter-wave communications: Access and networking – Challenges and protocols,” *IEEE Commun. Mag.*, vol. 53, no. 1, pp. 222–231, Jan. 2014.
- [63] R. J. Weiler, M. Peter, W. Keusgen, E. C. -Strinati, A. D. Domenico, I. Filipini, A. Capone, I. Siaud, A. -M. U. -Moll, A. Maltsev, T. Haustein, and K. Sakaguchi, “Enabling 5G backhaul and access with millimeter-waves” *In Proc. Eur. Conf. Netw. Commun. (EuCNC)*, pp. 1–5, Jun. 2014.
- [64] T. E. Bogale and L. B. Le, “Massive MIMO and mmWave for 5G wireless HetNet: Potential benefits and challenges,” *IEEE Veh. Technol. Mag.*, vol. 11, no. 1, pp. 64–75, Mar. 2016.
- [65] F. Demers, H. Yanikomeroglu, and M. St-Hilaire, “A survey of opportunities for free space optics in next generation cellular networks” *In Proc. IEEE 9th Annu. Commun. Netw. Services Res. Conf. (CNSR)*, pp. 210–216, Ottawa, ON, Canada, May 2011.
- [66] N. Letzepis and A. G. I. Fbregas, *Hybrid RF/FSO communications*. Advanced Optical Wireless Communication Systems. Cambridge, U.K.: Cambridge Univ. Press, 2012, pp. 273–302.
- [67] J. Rak and W. Molisz, “Reliable routing and resource allocation scheme for hybrid RF/FSO networks” *In Proc. 16th Int. Conf. Transparent Opt. Netw. (ICTON)*, Graz, Austria, pp. 1–4, Jul. 2014,
- [68] V. W. S. Chan, “Free-space optical communications,” *IEEE/OSA J. Lightw. Technol.*, vol. 24, no. 12, pp. 4750–4762, Dec. 2006.
- [69] M. Zotkiewicz, W. Ben-Ameur, and M. Pioro, “Finding failure-disjoint paths for path diversity protection in communication networks,” *IEEE Commun. Lett.*, vol. 14, no. 8, pp. 776–778, Aug. 2010.
- [70] Z. Ghassemlooy, W. Popoola, and S. Rajbhandari *Optical Wireless Communications: System and Channel Modeling With MATLAB*. Boca Raton, FL, USA: CRC Press, 2012.
- [71] M. A. Khalighi and M. Uysal, “Survey on free space optical communication: A communication theory perspective,” *IEEE Commun. Surveys Tuts.*, vol. 16, no. 4, pp. 2231–2258, Nov. 2014.
- [72] D. K. Borah, A. C. Boucouvalas, C. C. Davis, S. Hranilovic, and K. Yiannopoulos, “A review of communication-oriented optical wireless systems,” *EURASIP J. Wireless Commun. Netw.*, vol. 2012, no. 1, p. 91, Dec. 2012.
- [73] O. Awwad, A. Al-Fuqaha, B. Khan, and G. B. Brahim, “Topology control schema for better QoS in hybrid RF/FSO mesh networks,” *IEEE Trans. Commun.*, vol. 60, no. 5, pp. 1398–1406, May 2012.
- [74] J. Llorca, A. Desai, and S. Milner, “Obscuration minimization in dynamic free space optical networks through topology control,” *In Proc. Military Commun. Conf. (MILCOM)*, vol. 3. Monterey, CA, USA, Oct./Nov. 2004, pp. 1247–1253.



- [75] M. N. Smadi, S. C. Ghosh, A. A. Farid, T. D. Todd, and S. Hranilovic, "Free-space optical gateway placement in hybrid wireless mesh networks," *J. Lightw. Technol.*, vol. 27, no. 14, pp. 2688–2697, Jul. 15, 2009.
- [76] V. Rajakumar, M. N. Smadi, S. C. Ghosh, T. D. Todd, and S. Hranilovic, "Interference management in WLAN mesh networks using free-space optical links," *J. Lightw. Technol.*, vol. 26, no. 13, pp. 1735–1743, Jul. 1, 2008.
- [77] A. Kashyap and M. Shayman, "Routing and traffic engineering in hybrid RF/FSO networks," *In Proc. IEEE Int. Conf. Commun. (ICC)*, vol. 5, pp. 3427–3433, Seoul, South Korea, May 2005.
- [78] Y. Tang and M. Brandt-Pearce, "Link allocation, routing, and scheduling for hybrid FSO/RF wireless mesh networks," *IEEE/OSA J. Opt. Commun. Netw.*, vol. 6, no. 1, pp. 86–95, Jan. 2014.
- [79] D. Wang and A. A. Abouzeid, "Throughput capacity of hybrid radio-frequency and free-space-optical (RF/FSO) multi-hop networks," *In Proc. IEEE Inf. Theory Workshop (ITW)*, pp. 3–10, Bergen, Norway, Jan./Feb. 2007.
- [80] I. K. Son and S. Mao, "Design and optimization of a tiered wireless access network," *In Proc. IEEE Conf. Comput. Commun. (INFOCOM)*, pp. 1–9, San Diego, CA, USA, Mar. 2010.
- [81] X. Cao, "An integer linear programming approach for topology design in OWC networks," *In Proc. IEEE Global Telecommun. Workshops (GLOBECOM)*, pp. 1–5 New Orleans, LA, USA, Nov. 2008.
- [82] F. Ahdi and S. Subramaniam, "Optimal placement of FSO links in hybrid wireless optical networks," *In Proc. IEEE Global Telecommun. Conf. (GLOBECOM)*, pp. 1–6, Houston, TX, USA, Dec. 2011.
- [83] A. Douik, H. Dahrouj, T. Y. Al-Naffouri, and M.-S. Alouini, "Hybrid radio/free-space optical design for next generation backhaul systems," *IEEE Trans. Commun.*, vol. 64, no. 6, pp. 2563–2577, Jun. 2016.
- [84] Y. Li, M. Piro, and V. Angelakis, "Design of cellular backhaul topology using the FSO technology," *In Proc. 2nd Int. Workshop Opt. Wireless Commun. (IWOW)*, pp. 6–10, Newcastle Upon Tyne, U.K., Oct. 2013.
- [85] Y. Li, N. Pappas, V. Angelakis, M. Piro, and D. Yuan, "Optimization of free space optical wireless network for cellular backhauling," *IEEE J. Sel. Areas Commun.*, vol. 33, no. 9, pp. 1841–1854, Sep. 2015.
- [86] Y. Li, N. Pappas, V. Angelakis, M. Piro, and D. Yuan, "Resilient topology design for free space optical cellular backhaul networking," *In Proc. IEEE Global Telecommun. Conf. Workshops (GLOBECOM)*, pp. 487–492, Austin, TX, USA, Dec. 2014.
- [87] J. E. Mitchell, "Integrated wireless backhaul over optical access networks (Invited paper)," *IEEE/OSA J. Lightw. Technol.*, vol. 32, no. 20, pp. 3373–3382, Oct. 2014.

- 
- [88] C. Liu, J. Wang, L. Cheng, M. Zhu, and G. -K. Chang, “Key microwave-photonics technologies for next-generation cloud-based radio access networks (Invited paper),” *IEEE/OSA J. Lightw. Technol.*, vol. 32, no. 20, pp. 3452–3460, Oct. 2014.
- [89] P. T. Dat, A. Kanno, K. Inagaki, and T. Kawanishi, “High-capacity wireless backhaul network using seamless convergence of radio-over-fiber and 90-GHz millimeter-wave,” *IEEE/OSA J. Lightw. Technol.*, vol. 32, no. 20, pp. 3910–3923, Oct. 2014.
- [90] A. T. Pham, P. V. Trinh, V. V. Mai, N. T. Dang, and T. -C. Thang, “Hybrid free-space optics/millimeter-wave architecture for 5G mobile backhaul networks,” *In Proc. of the 20th Opto-Electronics and Communications Conference (OECC 2015)*, pp. 1–3, Jul. 2015.
- [91] O. Tipmongkolsilp, S. Zaghoul, and A. Jukan, “The evolution of cellular backhaul technologies: current issues and future trends,” *IEEE Commun. Surveys Tuts.*, vol. 13, no. 1, pp. 97–113, Feb. 2011.
- [92] S. Chia, M. Gasparroni, and P. Brick, “The next challenge for cellular networks: backhaul,” *IEEE Microw. Mag.*, vol. 10, no. 5, pp. 97–113, Feb. 2011.
- [93] F. Boccardi, R. W. Heath, A. Lozano, T. L. Marzetta, and P. Popovski, “Five disruptive technology directions for 5G,” *IEEE Commun. Mag.*, vol. 52, no. 2, pp. 74–80, Feb. 2014.
- [94] T. S. Rappaport, R. W. Heath Jr., R. C. Daniels, and J. N. Murdock, *Millimeter wave wireless communications*, Prentice Hall, 2014.
- [95] B. He and R. Schober, “Bit-interleaved coded modulation for hybrid RF/FSO systems,” *IEEE Trans. Commun.*, vol. 23, no. 21, pp. 1642–1644, Nov. 2011.
- [96] N. D. Chatzidiamantis, G. K. Karagiannidis, E. E. Kriezis, and M. Matthaiou, “Diversity combining in hybrid RF/FSO systems with PSK modulation,” *Proc. of the IEEE International Conference on Communications (ICC)*, pp. 1–6, Jun. 2011.
- [97] H. E. Nistazakis, A. N. Stassinakis, G. S. Tombras, S. S. Muhammad, and A. D. Tsigopoulos, “K modeled turbulence and nonlinear clipping for QAM OFDM with FSO and fiber serially linked,” *Proc. of the 20th International Conference on Microwaves, Radar, and Wireless Communication (MIKON)*, pp. 1–4, Jun. 2014.
- [98] P. V. Trinh, A. T. Pham, H. T. T. Pham, and N. T. Dang, “BER analysis of all-optical AF dual-hop FSO systems over Gamma-Gamma channels,” *Proc. of the 4th IEEE International Conference on Photonics (ICP)*, pp. 175–177, Oct. 2013.
- [99] M. A. Al-Habash, L. C. Andrews, and R. L. Philips, “Mathematical model for the irradiance probability density function of a laser beam propagating through turbulent media,” *Optical Engineering*, vol. 40, pp. 1554–1562, Aug. 2001.

- [100] T. McKenna, J. C. Juarez, J. A. Nanzer, and T. R. Clark, "Hybrid millimeter-wave/free-space optical system for high data rate communications," *In Proc. of the 2013 IEEE Photonics Conference (IPC)*, pp. 203–204, Sept. 2015.
- [101] B. Makki, T. Svensson, and M.-S. Alouini, "On the performance of millimeter wave-based RF-FSO links with HARQ feedback," *In Proc. of the 2016 IEEE 27th Annual International Symposium on Personal, Indoor, and Mobile Radio Communications (PIMRC)*, pp. 1–6, Sept. 2016.
- [102] H. Dahrouj, A. Douik, F. Rayal, T. Y. Al-Naffouri, and M.-S. Alouini, "Cost-effective hybrid RF/FSO backhaul solution for next generation wireless systems," *IEEE Wireless Commun.*, vol. 22, no. 5, pp. 98–104, Oct. 2015.
- [103] D. Schulz, V. Jungnickel, C. Alexakis, M. Schlosser, J. Hilt, A. Paraskevoudoulos, L. Grobe, P. Farkas, and R. Freund, "Robust optical wireless link for the backhaul and fronthaul of small radio cells," *IEEE/OSA J. Lightw. Technol.*, vol. 34, no. 6, pp. 1523–1532, Mar. 2016.
- [104] L. Yang, X. Gao, and M.-S. Alouini, "Performance analysis of relay-assisted all-optical FSO networks over strong atmospheric turbulence channels with pointing errors," *IEEE/OSA J. Lightw. Technol.*, vol. 32, no. 23, pp. 4613–4619, Dec. 2014.
- [105] S. S. Soliman, V. C. M. Leung, N. C. Beaulieu, and J. Cheng, "Analysis of general dual-hop AF systems over Rician fading links," *In Proc. IEEE Global Telecommun. Conf.*, pp. 1–6, Dec. 2015.
- [106] E. Zedini, I. S. Ansari, M. -S. Alouini, "Performance analysis of mixed Nakagami- $m$  and Gamma-Gamma dual-hop FSO transmission systems," *IEEE Photon. J.*, vol. 7, no. 1, Article no. 7900120, Feb. 2015.
- [107] L. Yang, M. O. Hasna, and X. Gao, "Performance of mixed RF/FSO with variable gain over generalized atmospheric turbulence channels," *IEEE J. Sel. Areas Commun.*, vol. 33, no. 9, pp. 1913–1924, Sept. 2015.
- [108] L. Kong, W. Xu, L. Hanzo, H. Zhang, and C. Zhao, "Performance of a free-space-optical relay-assisted hybrid RF/FSO system in generalized  $M$ -distributed channels," *IEEE Photon. J.*, vol. 7, no. 5, Article no. 7903319, Oct. 2015.
- [109] E. Zedini, H. Soury, M. -S. Alouini, "On the performance analysis of dual-hop mixed FSO/RF systems," *IEEE Trans. Wireless Commun.*, DOI 10.1109/TWC.2016.2524685, 2016.
- [110] M. K. Samimi and T. S. Rappaport, "28 GHz millimeter-wave ultrawideband small-scale fading models in wireless channels," *In Proc. of the 2016 IEEE 83rd Vehicular Technology Conference: VTC2016-Spring*, Nanjing, China, May 2016.
- [111] M. K. Simon and M. -S. Alouini, *Digital communications over fading channels*, Wiley Interscience, 2005.

- [112] A. Farid and S. Hranilovic, "Outage capacity optimization for free-space optical links with pointing errors," *IEEE/OSA J. Lightwave Technol.*, vol. 25, pp. 1702–1710, Jul. 2007.
- [113] X. Song, F. Yang, and J. Cheng, "Subcarrier intensity modulated optical wireless communications," *IEEE/OSA J. Lightw. Technol.*, vol. 32, no. 20, pp. 3373–3382, Jun. 2013.
- [114] E. Lee, J. Park, D. Han, and G. Yoon, "Performance analysis of the asymmetric dual-hop relay transmission with mixed RF/FSO links," *IEEE Photon. Technol. Lett.*, vol. 23, no. 21, pp. 1642–1644, Nov. 2011.
- [115] N. D. Chatzidiamantis, G. K. Karagiannidis, E. E. Kriezis, and M. Matthaiou, "Diversity combining in hybrid RF/FSO systems with PSK modulation," *In Proc. of the IEEE International Conference on Communications (ICC)*, pp. 1–6, Jun. 2011.
- [116] I. S. Gradshteyn and I. M. Ryzhik, *Table of Integrals, Series and Products*. New York: Academic Press, Seventh Edition, 2007.
- [117] P. V. Trinh and A. T. Pham, "Outage performance of dual-hop AF relaying systems with mixed MMW RF and FSO links," *In Proc. of the IEEE 82nd Vehicular Technology Conference: VTC2015-Fall*, pp. 1–5, Sept. 2015.
- [118] L. C. Andrews and R. N. Phillips, *Laser beam propagation through random media*, 2nd ed. Bellingham, WA, USA: SPIE, 2005.
- [119] A. J. Navas, J. M. G. Balsells, J. F. Paris, and A. P. Notario, "A unifying statistical model for atmospheric optical scintillation," *Numerical Simulations of Physical and Engineering Processes*, J. Awrejcewicz, Ed., Intech, 2011, ch.8.
- [120] A. J. Navas, J. M. G. Balsells, J. F. Paris, M. C. Vazquez, and A. P. Notario, "Impact of pointing errors on the performance of generalized atmospheric optical channels," *Opt. Exp.*, vol. 20, pp. 12550–12562, May 2012.
- [121] I. S. Ansari, F. Yilmaz, and M. -S. Alouini, "Performance analysis of free-space optical links over Málaga ( $\mathcal{M}$ ) turbulence channels with pointing errors," *IEEE Trans. Wireless Commun.*, vol. 15, no. 1, pp. 91–102, Jan. 2016.
- [122] V. S. Adamchik and O. I. Marichev, "The algorithm for calculating integrals of hypergeometric type functions and its realization in reduce system," *In Proc. of the Int. Con. Symbolic and Algebraic Computation*, pp. 212–224, Tokyo, Japan, 1990.
- [123] The Wolfram functions site. Internet. [Online]. Available: [www.functions.wolfram.com](http://www.functions.wolfram.com).
- [124] J. Lu, K. B. Letaief, J. C. -I. Chuang, and M. L. Liou, "M-PSK and M-QAM BER computation using signal space concepts," *IEEE Trans. Commun.*, vol. 47, no. 2, pp. 181–184, Feb. 1999.

- [125] Y. Zhao, P. Adve, and T. J. Lim, "Symbol error rate of selection amplify-and-forward relay systems," *IEEE Commun. Lett.*, vol. 10, no. 11, pp. 757–759, Nov. 2006.
- [126] M. I. Petkovic, A. M. Cvetkovic, G. T. Djordjevic, and G. K. Karagiannidis, "Partial relay selection with outdated channel state estimation in mixed RF/FSO systems," *IEEE/OSA J. Lightw. Technol.*, vol. 33, no. 13, pp. 2860–2867, Mar. 2015.
- [127] A. Belmonte and J. M. Kahn, "Capacity of coherent free-space optical links using atmospheric compensation techniques," *OSA Optics Express*, vol. 17, no. 4, pp. 2763–2773, Feb. 2009.
- [128] A. Mathai and R. Saxena, *The H-function with applications in statistics and other disciplines*. New York, NY, USA: Wiley, 1978.
- [129] B. L. Sharma, "Some formulae for generalized function of two variables," *Matematski Vesnik*, vol. 5, no. 20, pp. 43–52, 1968.
- [130] I. S. Ansari, S. A. Ahmadi, F. Yilmaz, M. -S. Alouini, and H. Yanikomeroğlu, "A new formula for the BER of binary modulations with dual-branch selection over generalized-K composite fading channels," *IEEE Trans. Commun.*, vol. 59, no. 10, pp. 2654–2658, Oct. 2011.
- [131] K. P. Peppas, "A new formula for the average bit error probability of dual-hop amplify-and-forward relaying systems over generalized shadowed fading channels," *IEEE Wireless Commun. Lett.*, vol. 1, no. 2, pp. 85–88, Jan. 2012.
- [132] H. Chergui, M. Benjillali, and S. Saoudi, "Performance analysis of project-and-forward relaying in mixed MIMO-pinhole and Rayleigh dual-hop channel," *IEEE Commun. Lett.*, vol. 20, no. 3, pp. 610–613, Mar. 2016.
- [133] X. Zhu and J. M. Kahn, "Free-space optical communication through atmospheric turbulence channels," *IEEE Trans. Commun.*, vol. 50, no. 8, pp. 1293–1300, Aug. 2002.
- [134] M. Safari and M. Uysal, "Relay-assisted free-space optical communication," *IEEE Trans. Wireless Comm.*, vol. 7, no. 12, Dec. 2008.
- [135] B. Rankov and A. Wittneben, "Spectral efficient protocols for half-duplex fading relay channels," *IEEE J. Sel. Areas Commun.*, vol. 25, no. 2, pp. 379–389, Feb. 2007.
- [136] Y. Tang, X. Zhou, Z. Zhang, and Q. Tian, "Performance analysis of a two-way network-coded free space optical relay scheme over strong turbulence channels," *Proc. of IEEE Vehicular Technology Conference (VTC)*, pp. 1-5, 2011.
- [137] P. Puri, P. Garg, and M. Aggarwal, "Analysis of spectrally efficient two-way relay assisted free-space optical systems in atmospheric turbulence with path loss," *Wiley Int. J. Commun. Syst.*, 2014, DOI: 10.1002/dac.3027.

- [138] P. Puri, P. Garg, and M. Aggarwal, "Outage and error rate analysis of network-coded coherent TWR-FSO systems," *IEEE Photon. Technol. Lett.*, vol. 26, no. 18, pp. 1797–1800, Sept. 2014.
- [139] P. K. Sharma and P. Garg, "Bi-directional decode-XOR-forward relaying over  $\mathcal{M}$ -distributed free space optical links," *IEEE Photon. Technol. Lett.*, vol. 26, no. 19, pp. 1916–1919, Oct. 2014.
- [140] P. Puri, P. Garg, and M. Aggarwal, "Bi-directional relay-assisted FSO communication systems over strong turbulence channels with pointing errors," *Wiley Int. J. Commun. Syst.*, 2015, DOI: 10.1002/dac.3027.
- [141] P. K. Sharma, A. Bansal, and P. Garg, "Relay assisted bi-directional communication in generalized turbulence fading," *IEEE/OSA J. Lightw. Technol.*, vol. 33, no. 1, pp. 133–139, Jan. 2015.
- [142] P. Puri, P. Garg, and M. Aggarwal, "Partial dual-relay selection protocols in two-way relayed FSO networks," *IEEE/OSA J. Lightw. Technol.*, 2015, DOI: 10.1109/JLT.2015.2475609.
- [143] P. Puri, P. Garg, and M. Aggarwal, "Asymptotic analysis of TWR assisted FSO links with partial dual-relay selection," *IEEE Commun. Lett.*, vol. 19, no. 5, pp. 879–882, May 2015.
- [144] P. Puri, N. D. Chatzidiamantis, P. Garg, M. Aggarwal, and G. K. Karagiannidis, "Two-way relay selection in multiple relayed FSO networks," *IEEE Wireless Commun. Lett.*, vol. 4, no. 5, pp. 485–488, Jun. 2015.
- [145] J. N. Laneman, D. N. Tse, and G. W. Wornell, "Cooperative diversity in wireless networks: efficient protocols and outage behavior," *IEEE Trans. Inform. Theory*, vol. 50, no. 12, pp. 3062–3080, Dec. 2004.
- [146] S. Kazemlou, S. Hranilovic, and S. Kumar, "All-optical multihop free-space optical communication systems," *IEEE/OSA J. Lightw. Technol.*, vol. 29, no. 18, pp. 2663–2669, Sept. 2011.
- [147] E. Bayaki, D. S. Michalopoulos, and R. Schober, "EDFA-based all-optical relaying in free-space optical systems," *IEEE Trans. Commun.*, vol. 60, no. 12, pp. 3797–3807, Dec. 2012.
- [148] L. Yang, X. Gao, and M.-S. Alouini, "Performance analysis of relay-assisted all-optical FSO networks over strong atmospheric turbulence channels with pointing errors," *IEEE/OSA J. Lightw. Technol.*, vol. 32, no. 23, pp. 4613–4620, Dec. 2014.
- [149] X. Song and J. Cheng, "Optical communication using subcarrier intensity modulation in strong atmospheric turbulence," *IEEE/OSA J. Lightw. Technol.*, vol. 30, no. 22, pp. 3484–3492, Nov. 2012.
- [150] J. Yang, P. Fan, T. Q. Duong, and X. Lei, "Exact performance of two-way AF relaying in Nakagami-m fading environment," *IEEE Trans. Wireless Commun.*, vol. 10, no. 3, pp. 980–987, Mar. 2011.

- [151] A. J.-Navas and A. P. -Notario, "Generation of correlated scintillations on atmospheric optical communications," *IEEE/OSA J. Opt. Commun. Netw.*, vol. 1, no. 5, pp. 452–462, Oct. 2009.
- [152] I. S. Ansari, F. Yilmaz, and M.-S. Alouini, "Performance analysis of free-space optical links over Málaga ( $\mathcal{M}$ ) turbulence channels with pointing errors," *IEEE Trans. Wireless Commun.*, vol. 15, no. 1, pp. 91–102, Jan. 2016.
- [153] M. D. Renzo, F. Graziosi, and F. Santucci, "A unified framework for performance analysis of CSI-assisted cooperative communications over fading channels," *IEEE Trans. Commun.*, vol. 57, no. 9, pp. 2551–2557, Sep. 2009.
- [154] M. Shah, "On generalization of some results and their applications," *Collectanea Math.*, vol. 24, no. 3, pp. 249–266, 1973.
- [155] M. K. Simon and M.S. Alouini, *Digital Communication over Fading Channels*, New York: John Wiley and Sons, 2000.
- [156] G. P. Efthymoglou, N. Y. Ermolova, and V. A. Aalo, "Channel capacity and average error rates in generalised-K fading channels," *IET Commun.*, vol. 4, no. 11, pp. 1364–1372, Jul. 2010.
- [157] Q. Liu, C. Qiao, G. Mitchell, and S. Stanton, "Optical wireless communication networks for first- and last-mile broadband access [Invited]," *J. Opt. Netw.*, vol. 4, no. 12, pp. 807–828, Dec. 2005.
- [158] E. Ciaramella, Y. Arimoto, G. Contestabile, M. Presi, A. D'Errico, V. Guarino, and M. Matsumoto, "1.28 Terabit/s (32 x 40Gbit/s) WDM transmission system for free space optical communications," *IEEE J. Sel. Areas Commun.*, vol. 27, no. 9, pp. 1639–1645, Dec. 2009.
- [159] L. G. Kazovsky, W. -T. Shaw, D. Gutierrez, N. Cheng, and S. -W. Wong, "Next-generation optical access networks," *IEEE/OSA J. Lightw. Technol.*, vol. 25, no. 11, pp. 3428–3442, Nov. 2007.
- [160] M. Forzati, A. Bianchi, J. Chen, K. Grobe, B. Lannoo, C. M. Machuca, J. -C. Point, B. Skubic, S. Verbrugge, E. Weis, L. Wosinska, and D. Breuer, "Next-generation optical access seamless evolution: concluding results of the European FP7 project OASE," *IEEE/OSA J. Opt. Commun. Netw.*, vol. 7, no. 2, pp. 109–123, Feb. 2015.
- [161] S. Hitam, S. N. Suhaimi, A. S. Noor, S. B. Anas, and R. K. Sahbudin, "Performance analysis on 16-channels wavelength division multiplexing in free space optical transmission under tropical regions environment," *Journal of Computer Science*, vol. 8, no. 1, pp. 145–148, 2012.
- [162] T. Kamalakis, I. Neokosmidis, A. Tsipouras, T. Sphicopoulos, S. Pantazis, and I. Andrikopoulos, "Hybrid free space optical/millimeter wave outdoor links for broadband wireless access networks," *Proc. of IEEE 18th Int. Symp. On Personal, Indoor and Mobile Radio Communications*, pp. 1–5, Athens, Greece, 2007.

- [163] A. O. Aladeloba, M. S. Woolfson, and A. J. Phillips, "WDM/FSO network with turbulence-accentuated interchannel crosstalk," *IEEE/OSA J. Opt. Commun. Netw.*, vol. 5, no. 6, pp. 641-651, June 2013.
- [164] V. V. Mai and A. T. Pham, "Adaptive rate-based MAC protocols design and analysis for integrated FSO/PON networks," *Proc. of the 2015 IEEE International Conference on Commun. (ICC'15)*, pp. 6629-6634, London, UK, Jun. 2015.
- [165] Y. Arimoto, "Compact free-space optical terminal for multi-gigabit signal transmission with a single mode fiber," *Proc. SPIE*, vol. 7199, no. 7, 2009.
- [166] C. K. Datsikas, K. P. Peppas, N. C. Sagiass, and G. S. Tombras, "Serial free-space optical relaying communications over gamma-gamma atmospheric turbulence channels," *IEEE/OSA J. Opt. Commun. Netw.*, vol. 2, no. 8, pp. 576-586, Aug. 2010.
- [167] T. V. Pham and A. T. Pham, "Performance analysis of amplify-decode-and-forward multihop binary phase-shift keying/free-space optical systems using avalanche photodiode receivers over atmospheric turbulence channels," *IET Commun.*, vol. 8, no. 9, pp. 1518-1526, Jun. 2014.
- [168] E. Bayaki, D. S. Michalopoulos, R. Schober, "EDFA-based all-optical relaying in free-space optical systems," *IEEE Trans. Commun.*, vol. 60, no. 12, pp. 3797-3807, Dec. 2012.
- [169] M. A. Kashani, M. M. Rad, M. Safari, and M. Uysal, "All-optical amplify-and-forward relaying system for atmospheric channels," *IEEE Commun. Letters*, vol. 16, no. 10, pp. 1684-1687, Oct. 2012.
- [170] P. V. Trinh, N. T. Dang, and A. T. Pham, "All-optical AF Relaying FSO Systems using EDFA combined with OHL over Gamma-Gamma Channels," *Proc. of the 2015 IEEE International Conference on Commun. (ICC'15)*, pp. 6720-6725, London, UK, Jun. 2015.
- [171] N. T. Dang and A. T. Pham, "Performance improvement of FSO/CDMA system over dispersive turbulence channel using multi-wavelength PPM signaling," *OSA Optics Express*, vol. 20, issue 24, pp. 26786-26797, Nov. 2012.
- [172] N. T. Dang, H. T. T. Pham, and A. T. Pham, "Average BER analysis of multihop FSO systems over strong turbulence and misalignment fading channels," *Proc. of the 2013 IEEE/CIC International Conference on Communications in China (ICCC)*, pp. 153-157, Xi'an, China, Aug. 2013.
- [173] K. Kiasaleh, "Performance of APD-Based, PPM Free-Space Optical Communication Systems in Atmospheric Turbulence," *IEEE Trans. Commun.*, vol. 53, no. 9, pp. 1455-1461, Sept. 2005.
- [174] S. G. Wilson, M. Brandt-Pearce, Q. Cao, and J. H. Leveque, "Free-Space Optical MIMO Transmission With Q-ary PPM," *IEEE Trans. Commun.*, vol. 53, no. 8, pp. 1402-1412, Aug. 2005.



- [175] W. Gappmair, S. Hranilovic, and E. Leitgeb, "Performance of PPM on terrestrial FSO links with turbulence and pointing errors," *IEEE Commun. Lett.*, vol. 14, no. 5, pp. 868–870, May 2010.
- [176] E. J. Lee and V. Chan, "Part 1: Optical communication over the clear turbulent atmospheric channel using diversity," *IEEE J. Sel. Areas Commun.*, vol. 22, no. 9, pp. 1896–1906, Nov. 2004.
- [177] S. B. Weinstein, Y. Luo, and T. Wang, "The ComSoc guide to passive optical networks: Enhancing the last mile access," *John Wiley & Sons, Inc.*, 2012.
- [178] D. Nasset, "NG-PON2 technology and standards," *IEEE/OSA J. Lightw. Technol.*, vol. 33, no. 5, pp. 1136–1143, Mar. 2015.
- [179] P. T. Dat, A. Bekkali, K. Kazaura, K. Wakamori, and M. Matsumoto, "A universal platform for ubiquitous wireless communications using radio over FSO system," *IEEE/OSA J. Lightw. Technol.*, vol. 28, no. 16, pp. 2258–2267, Aug. 2010.
- [180] R. Ramaswami and K. N. Sivarajan, *Optical Networks—A practical Perspective*, 2nd ed. London: Academic, 2002.
- [181] I. T. Monroy and E. Tangdionga, *Crosstalk in WDM Communication Networks*. Norwell, MA: Kluwer Academic, 2002.
- [182] G. P. Agrawal, *Fiber Optic Communication Systems*, John Wiley and Sons Inc., third ed., 2002.
- [183] C. Y. Young, L. C. Andrews, and A. Ishimaru, "Time-of-arrival fluctuations of a spacetime Gaussian pulse in weak optical turbulence: an analytic solution," *Appl. Opt.*, vol. 37, no. 33, pp. 7655–7660, Nov. 1998.
- [184] J. W. Goodman, *Statistical Optics*, Hoboken, NY: Wiley-Inter-science, 2000.
- [185] W. Zhang, S. Hranilovic, and C. Shi, "Soft-switching hybrid FSO/RF links using short-length raptor codes: design and implementation," *IEEE J. Sel. Areas Commun.*, vol. 27, no. 9, pp. 1698–1708, Dec. 2009.
- [186] I. B. Djordjevic, "Adaptive modulation and coding for free-space optical channels," *IEEE/OSA J. Opt. Commun. Netw.*, vol. 2, no. 5, pp. 221–229, May 2010.
- [187] M. Niu, J. Cheng, and J. F. Holzman, "Exact error rate analysis of equal gain and selection diversity for coherent free-space optical systems on strong turbulence channels," *OSA Opt. Express*, vol. 18, pp. 13915–13926, Jun. 2010.
- [188] M. Niu, J. Cheng, and J. F. Holzman, "A MIMO architecture for coherent optical wireless communication: system design and performance," *IEEE/OSA J. Opt. Commun. Netw.*, vol. 5, pp. 411–420, May 2013.
- [189] T. Eng, N. Kong, and L. B. Milstein, "Comparison of diversity combining techniques for Rayleigh-fading channels," *IEEE Trans. Commun.*, vol. 44, no. 9, pp. 1117–1129, Sep. 1996.

- 
- [190] M. K. Simon and M. -S. Alouini, "Performance analysis of generalized selection combining with threshold test per branch (T-GSC)," *IEEE Trans. Veh. Technol.*, vol. 51, no. 5, pp. 1018–1029, Sept. 2002.
- [191] A. Annamalai, G. Deora, and C. Tallembara, "Analysis of generalized selection diversity systems in wireless channels," *IEEE Trans. Veh. Technol.*, vol. 55, no. 6, pp. 1765–1775, Nov. 2006.
- [192] H. Moradi, H. H. Refai, and P. G. LoPresti, "Circular MIMO FSO nodes with transmit selection and receive generalized selection diversity," *IEEE Trans. Veh. Technol.*, vol. 61, no. 3, pp. 1174–1181, Mar. 2012.
- [193] F. J. Lopez-Martinez, J. M. Romero-Jerez, and J. F. Paris, "On the calculation of the incomplete MGF with applications to wireless communications," *IEEE Trans. Commun.*, vol. 65, no. 1, pp. 458–469, Jan. 2017.
- [194] A. T. Pham and D. A. Luong, "Optical wireless communications over fading channels: Spatial diversity or multihop relaying? (Invited Paper)," *In the Proc. of the 2014 Int. Conf. on Adv. Technol. Commun. (ATC 2014)*, pp. 760–765, Hanoi, Vietnam, Oct. 2014.
- [195] H. G. Sandalidis, N. D. Chatzidiamantis, and G. K. Karagiannidis, "A tractable model for turbulence- and misalignment-induced fading in optical wireless systems," *IEEE Commun. Lett.*, vol. 20, no. 9, pp. 1904–1907, Sept. 2016.
- [196] H. G. Sandalidis, N. D. Chatzidiamantis, G. D. Ntouni, and G. K. Karagiannidis, "Performance of free-space optical communications over a mixture composite irradiance channel," *Electronics Letters*, vol. 53, no. 4, pp. 260–262, Feb. 2017.
- [197] N. I. Miridakis and T. A. Tsiftsis, "EGC reception for FSO systems under mixture-Gamma fading channels and pointing errors," *IEEE Commun. Lett.*, vol. PP, no. 99, pp. 1–1, Feb. 2017. DOI: 10.1109/LCOMM.2017.2670565.
- [198] N. I. Miridakis, D. D. Vergados, and A. Michalas, "Performance of maximum-ratio combining-enabled heterodyne detection for free-space optical systems under mixture-Gamma fading channels and pointing errors," *Electronics Letters*, DOI:10.1049/el.2017.1006, Jun. 2017.
- [199] I. Djordjevic, W. Ryan, and B. Vasic, *Coding for optical channels*, Springer, 2010.
- [200] M. Abramowitz and I. A. Stegun, *Handbook of Mathematical Functions: With Formulas, Graphs, and Mathematical Tables*, 9th ed. New York, NY, USA: Dover 1972.
- [201] E. Karamad, R. S. Adve, Y. Lostanlen, F. Letourneux, and S. Guivarch, "Optimizing placements of backhaul hubs and orientations of antennas in small cell networks," *In Proc. of IEEE International Conference on Communications Workshop (ICC)*, pp. 68–73, London, England, Jul. 2015.

- [202] U. Siddique, H. Tabassum, E. Hossain, and D. I. Kim, "Wireless backhaul in future heterogeneous networks," *IEEE Wireless Commun.*, vol. 22, no. 5, pp. 22–31, Oct. 2015.
- [203] Mohamed Alzenad, Muhammad Z. Shakir, Halim Yanikomeroglu, and Mohamed-Slim Alouini, "FSO-based vertical backhaul/fronthaul framework for 5G+ wireless networks," *Under review in IEEE Commun. Mag.*, Available online: <https://arxiv.org/abs/1607.01472>.
- [204] M. Toyoshima, N. Yoshimura, B. Jeong, A. Akaishi, T. Takahashi, M. Akioka, Y. Fujino, S. Yamamoto, S. Taira, and N. Kadowaki, "Concept of satellite communication facility for disaster support located in the Tohoku district," *In Proc. of the 30th AIAA International Communications Satellite System Conference (ICSSC)*, pp. 1–8, Ottawa, Canada, Sept. 2012.
- [205] H. Kaushal and G. Kaddoum, "Optical communication in space: challenges and mitigation techniques," *IEEE Commun. Surveys Tut.*, vol. 19, no. 1, pp. 57–96, First Quarter 2017.
- [206] R. L. Graham, D. E. Knuth, and O. Patashnik, *Concrete Mathematics*. New York, NY, USA: Addison-Wesley, 1989.
- [207] A. Annamalai, C. Tallembara, and V. K. Bhargava, "Equal-gain diversity receiver performance in wireless channels," *IEEE Trans. Commun.*, vol. 48, no. 10, pp. 1732–1745, Oct. 2000.
- [208] Y. Deng, L. Wang, M. ElKashlan, K. J. Kim, and T. Q. Duong, "Generalized selection combining for cognitive relay networks over Nakagami- $m$  fading," *IEEE Trans. Signal Process.*, vol. 63, no. 8, pp. 1993–2006, Apr. 2015.
- [209] A. P. Prudnikov, Y. A. Brychkov, and O. I. Marichev, *Integrals and Series: Inverse Laplace Transform*. Gordon and Breach Science, 1992.

# Appendices

## A. A Proof of Theorem 1 in Chapter 7

From (7.9) and applying the multinomial theorem [206],  $[\phi_\gamma(s, \gamma)]^{M-1}$  can be rewritten as

$$[\phi_\gamma(s, \gamma)]^{M-1} = \sum_{k_1^\phi + \dots + k_N^\phi = M-1} \binom{M-1}{k_1^\phi, \dots, k_N^\phi} \times \prod_{i=1}^N a_i^{k_i^\phi} (s + \xi_i)^{-b_i k_i^\phi} [\Gamma(b_i, (s + \xi_i)\gamma)]^{k_i^\phi}, \quad (\text{A.1})$$

where  $\binom{M-1}{k_1^\phi, \dots, k_N^\phi} = \frac{(M-1)!}{k_1^\phi! \dots k_N^\phi!}$  is the multinomial coefficient, with  $k_1^\phi, \dots, k_N^\phi$  are nonnegative integer indices. With the help of [116, (8.354.5) and (8.972.1)], the upper incomplete Gamma function in (A.1) can be expanded in terms of an infinite series as

$$\Gamma(b_i, (s + \xi_i)\gamma) = e^{-(s + \xi_i)x} [(s + \xi_i)x]^{b_i} \sum_{n=0}^{\infty} \Lambda(n) \frac{\Phi(-n, b_i + 1; (s + \xi_i)x)}{n + 1}, \quad (\text{A.2})$$

where  $\Lambda(n) = \frac{\Gamma(n + b_i + 1)}{\Gamma(n + 1)\Gamma(b_i + 1)}$ ,  $\Phi(\cdot, \cdot; \cdot)$  is the Kummer confluent hypergeometric function [116, (9.210.1)]. (A.2) is valid for  $b_i$  taking on non-integer values typically for fading parameter  $\alpha$ , and converges rapidly with a truncation  $T_1$ . Plugging (A.2) into (A.1)

and applying the multinomial theorem, (A.1) can be rewritten as

$$[\phi_\gamma(s, \gamma)]^{M-1} = \widetilde{\sum_{\mathbb{S}_k^\phi}^N} \prod_{i=1}^N \prod_{n=0}^{T_1} A_{i,n}^{k_i^\phi} \gamma^{b_i k_i^\phi} e^{-(s+\xi_i)k_i^\phi \gamma} \times [\Phi(-n, b_i+1; (s+\xi_i)\gamma)]^{k_i^\phi}, \quad (\text{A.3})$$

where  $\widetilde{\sum_{\mathbb{S}_k^\phi}^N} \triangleq \sum_{S_1^\phi} \cdots \sum_{S_h^\phi} \cdots \sum_{S_k^\phi}$ ,  $|\mathbb{S}_k^\phi|$  is the cardinality of the set  $S_k^\phi$ , which denotes a set of  $(M-1)$ -tuples satisfying the condition  $S_k^\phi = \{(k_1^\phi, \dots, k_N^\phi) | \sum_{i=1}^N k_i^\phi = M-1\}$ , thereby  $|\mathbb{S}_k^\phi| = \binom{M+N-2}{N-1}$ .  $S_h^\phi = \{(h_0^\phi, \dots, h_{T_1}^\phi) | \sum_{n=0}^{T_1} h_n^\phi = k_i^\phi\}$ , with  $\{k_i^\phi\}, \{h_n^\phi\} \in \mathbb{Z}$ .  $A_{i,n} = \frac{a_i}{n+1} \Lambda(n)$ .

Similarly, from (7.3) and applying the multinomial theorem,  $[F_\gamma(\gamma)]^{L-M}$  can be expressed as

$$[F_\gamma(\gamma)]^{L-M} = \sum_{k_1^F + \dots + k_N^F = L-M} \binom{L-M}{k_1^F, \dots, k_N^F} \times \prod_{i=1}^N a_i^{k_i^F} \xi_i^{-b_i k_i^F} [\gamma(b_i, \xi_i \gamma)]^{k_i^F}. \quad (\text{A.4})$$

With the help of [116, (8.354.1)], the lower incomplete Gamma function in (A.4) can be expanded in terms of an infinite series as  $\gamma(b_i, \xi_i \gamma) = \sum_{l=0}^{\infty} \frac{(-1)^l (\xi_i \gamma)^{b_i+l}}{l!(b_i+l)}$ , which is also valid for  $b_i$  taking on non-integer values typically for fading parameter  $\alpha$ , and converges rapidly with a truncation  $T_2$  due to the factorial term  $l!$  in the denominator. Substituting the series expansion of  $\gamma(b_i, \xi_i \gamma)$  into (A.4) and applying the multinomial theorem, (A.4) can be rewritten as

$$[F_\gamma(\gamma)]^{L-M} = \widetilde{\sum_{\mathbb{S}_k^F}^N} \prod_{i=1}^N \prod_{l=0}^{T_2} A_{i,l}^{h_i^F} \xi_i^{(b_i+l)h_i^F - b_i k_i^F} \gamma^{(b_i+l)h_i^F}, \quad (\text{A.5})$$

where  $\widetilde{\sum_{\mathbb{S}_k^F}^N} \triangleq \sum_{S_1^F} \cdots \sum_{S_h^F} \cdots \sum_{S_k^F}$ ,  $|\mathbb{S}_k^F|$  is the cardinality of the set  $S_k^F$ , which denotes a set of  $(L-M)$ -tuples satisfying the condition  $S_k^F = \{(k_1^F, \dots, k_N^F) | \sum_{i=1}^N k_i^F = L-M\}$ , thereby  $|\mathbb{S}_k^F| = \binom{L-M+N-1}{N-1}$ .  $S_h^F = \{(h_0^F, \dots, h_{T_2}^F) | \sum_{n=0}^{T_2} h_n^F = k_i^F\}$ , with  $\{k_i^F\}, \{h_n^F\} \in \mathbb{Z}$ .

$$\mathbb{Z}. A_{i,l} = \left( \frac{(-1)^l a_i}{l(b_i+l)} \right)^{h_i^F}.$$

Substituting (7.2), (A.3) and (A.5) into (7.8), we arrive at the following expression

$$\Phi_{\gamma_{GSC}}(s) = M \binom{L}{M} \widetilde{\sum}_{\mathbb{S}^\Phi} \widetilde{\prod}_{i,n,l} A_{i,n,l}^\Phi \int_0^\infty \gamma^{\nu-1} e^{-\varepsilon\gamma} \prod_{k=1}^{k_i^\phi} \Phi(\sigma_k, \rho_k; \tau_k \gamma) d\gamma, \quad (\text{A.6})$$

where  $\widetilde{\sum}_{\mathbb{S}^\Phi} \triangleq \sum_{i=1}^N \widetilde{\sum}_{\mathbb{S}_{|S_k^\phi|}^\phi} \widetilde{\sum}_{\mathbb{S}_{|S_k^F|}^F}$ ,  $\widetilde{\prod}_{i,n,l} \triangleq \prod_{i=1}^N \prod_{n=0}^{T_1} \prod_{l=0}^{T_2}$ ,  $A_{i,n,l}^\Phi = a_i A_{i,n} A_{i,l}$ ,  $\nu = b_i(k_i^\phi + h_n^F + 1) + nh_n^F$ ,  $\varepsilon = (s + \xi_i)(k_i^\phi + 1)$ ,  $\{\sigma_1 = \dots = \sigma_k = \dots = \sigma_{k_i^\phi} = -n\}$ ,  $\{\rho_1 = \dots = \rho_k = \dots = \rho_{k_i^\phi} = (b_i + 1)\}$ , and  $\{\tau_1 = \dots = \tau_k = \dots = \tau_{k_i^\phi} = (s + \xi_i)\}$ . Applying the result from [207, (C.1)], a closed-form solution for (A.6) can be derived as in *Theorem 1*.

## B. A Proof of Lemma 1 in Chapter 7

The Laplace transform of  $\mathbb{F}_{\gamma_{GSC}}(\gamma)$  is given as  $\mathcal{L}[\mathbb{F}_{\gamma_{GSC}}(\gamma)] = \frac{\Phi_{\gamma_{GSC}}(s)}{s}$  [208].

From (7.10),  $\mathcal{L}[\mathbb{F}_{\gamma_{GSC}}(\gamma)]$  can be expressed as

$$\Phi_{\gamma_{GSC}}(s) = M \binom{L}{M} \widetilde{\sum}_{\mathbb{S}^\Phi} \widetilde{\prod}_{i,n,l} A_{i,n,l}^\Phi B_{i,n}^\Phi \frac{\Gamma(\nu)}{s(s + \xi_i)^\nu}, \quad (\text{B.1})$$

where  $B_{i,n}^\Phi = (k_i^\phi + 1)^{-\nu} F_A \left( \nu; \sigma_1, \dots, \sigma_{k_i^\phi}; \rho_1, \dots, \rho_{k_i^\phi}; \frac{\tau_1}{\varepsilon}, \dots, \frac{\tau_{k_i^\phi}}{\varepsilon} \right)$ . Then, taking the inverse Laplace transform of  $\mathcal{L}[\mathbb{F}_{\gamma_{GSC}}(\gamma)]$  with the help of [209, (2.1.2.1)], we arrive at *Lemma 1*.